DEVELOPMENT OF CATALYSTS FOR THE HYDROGASIFICATION OF CARBONACEOUS MATERIALS AND BIOMASS

Emilia Saraceno

UNIVERSITY OF SALERNO



DEPARTMENT OF INDUSTRIAL ENGINEERING

Ph.D. Course in Innovative Technologies for Industrial Sustainability (IETIS)
Curriculum in Chemical Engineering - XXXVIII Cycle

DEVELOPMENT OF CATALYSTS FOR THE HYDROGASIFICATION OF CARBONACEOUS MATERIALS AND BIOMASS

Supervisor
Prof. Vincenzo Palma

Ph.D. student
Emilia Saraceno

Scientific Referees
Prof. Vincenzo Palma
Ing. Eugenio Meloni, PhD
Ing. Alberto Giaconia, PhD

Ph.D. Course Coordinator
Prof. Diego Barletta

“Chance favors the prepared mind.”
Louis Pasteur

Acknowledgement

List of publications

Journal Articles:

1. Meloni, E.; **Saraceno, E.**; Martino, M.; Corrado, A.; Iervolino, G.; Palma, V.; *SiC-based structured catalysts for a high-efficiency electrified dry reforming of methane*. Renewable Energy 2023; 211:336–46. https://doi.org/10.1016/j. renene.2023.04.082.
2. **Saraceno, E.**; Ruocco, C.; Palma, V. *A Review of Coal and Biomass Hydrogasification: Process Layouts, Hydrogasifiers, and Catalysts*. Catalysts 2023, 13, 417. https://doi.org/10.3390/ catal13020417.
3. **Saraceno, E.**; Meloni, E.; Giaconia, A.; Palma, V. *Catalytic OBSiC Open Cell Foams for Methane-Rich Gas Production Through Hydrogasification of Plastic Waste*, Catalysts (2025), 15(2):152. https://doi.org/10.3390/catal15020152

Others:

1. **Saraceno, E.**; Renda, S.; Menéndez, M.; Palma, V. *Study on the Fluidization of Mixture of Plastic Waste and Alumina*, presented to Jornadas de jóvenes investigadores del I3A, 25 Giugno 2025, Saragozza, Spain.

Table of Contents

Chapter I. Introduction: Approaches for the conversion of carbonaceous materials 1

I.1 Carbonaceous materials and plastics as emerging energy feedstocks 1

I.2 Technologies for the conversion of carbonaceous materials and biomass 3

I.2.1 Pyrolysis 3

I.2.2 Gasification 6

I.3 An alternative process: the hydrogasification 9

Chapter II. State of the art 13

II.1 Overview of the coal and biomass hydrogasification process. 13

II.2 Catalytic hydrogasification 15

II.2.1 Literature on the catalytic coal hydrogasification 15

II.3 Catalytic mechanism of iron group metal-based catalysts for the coal hydrogasification 23

II.4 Catalytic conversion of plastic waste 26

II.5 Type of reactor configuration for plastic waste pyrolysis 34

II.6 Fluidization of plastic particles 35

II.6.1 Phenomenology of fluidization of binary mixtures 38

II.6.2 Minimum fluidization velocity estimation 40

II.6.3 Estimation of minimum fluidization velocity for binary mixture ... 43

Chapter III. Aim of the thesis 49

Chapter IV. Materials and methods 51

IV.1 Plastic waste matrix 51

IV.1.1 Pretreatment of the plastic waste matrix 51

IV.1.2 Thermogravimetric analysis (TGA) 52

IV.1.3 Kinetic evaluation of thermal degradation of plastic waste 52

IV.2 Carrier for the structured catalyst 54

IV.3 Preparation of the structured catalyst 55

IV.4 Preparation of powder catalysts 56

IV.5 Characterization technique 57

IV.6 Experimental plant 58

IV.7 Experimental evaluation and prediction of the minimum fluidization velocity 61

IV.8 Experimental evaluation 63
IV.8.1 Preliminary tests evaluation 63
IV.8.2 Test performed in the new reactor configuration 63
IV.8.3 Fluidization test performances evaluation 64

IV.9 COMSOL Multiphysics Simulations 65

Chapter V. Characterization results 67

V.1 Plastic waste matrix characterization 67

V.2 Catalyst Characterization 73
V.2.1 Structured catalyst characterization 73
V.2.2 Powder catalyst characterization 80

Chapter VI. Results and Discussion 81

VI.1 Results of the preliminary experimental tests 81

VI.2 Scale-up of the reactor and optimization of the reactor configuration 85
VI.2.1 Preliminary heating test in the new reactor configuration 86
VI.2.2 Results of structured catalyst activity test 89
VI.2.3 Solid products characterization and catalyst regeneration 92
VI.2.4 Results on the regenerated catalyst 96

VI.3 Mechanistic interpretation of the Ni–Ca/CeO_2/γ-Al_2O_3/OBSiC structured catalyst in Hydrogasification of plastic waste 97

VI.4 Results of fluidization experiments 100

VI.5 Implications of catalytic performance and fluidization behavior for hydrogasification scale-up 109

Chapter VII. Conclusions and future perspectives 113

Index of Figures

Figure I.1 *Pyrolysis process (reproduced from (Basu Prabir, 2013)*..... 4
Figure I.2 *Simplified layout of a pyrolysis plant* 5
Figure I.3 *Reaction sequence and potential paths for gasification* 7
Figure II.1 *Scheme of the hydrogasification process* 14
Figure II.2 *Schematic diagram of H_2 atoms spillover in the supported hydrogenation Ni catalysts and iron group metal loaded char system* 19
Figure II.3 *Schematic diagram of the reaction mechanism of SH on MC-hydrogasification catalyzed by an iron-group metal*..... 25
Figure II.4 *Pyrolysis mechanism and gas generation of PE (Reaction-1: the initial bond breaking reaction, Reaction-2: the terminal dissociation to monomer reaction, Reaction-3: the monomer dehydrogenation reaction) (Xuan et al., 2023)* 27
Figure II.5 *Steps that lead to segregation and fluidization when plastic feedstock is pyrolyzed in a fluidized bed reactor (Mastellone & Arena, 2004)* 37
Figure II.6 *Binary fluidization pattern: top fluidization.(Formisani et al., 2008)*..... 38
Figure II.7 *Binary fluidization pattern: bottom fluidization (Formisani et al., 2013)*..... 39
Figure II.8 *Three layers structures of mixtures of dissimilar solids (Formisani et al., 2013)*..... 40
Figure II.9 *A typical pressure-drop-velocity curve of a binary mixture. (Fu et al., 2019)* 45
Figure IV.1 *Plastic waste matrix supplied by ENEA Centro Ricerche Casaccia* 51
Figure IV.2 Grinder used for shredding the plastic waste..... 52
Figure IV.3 *Preparation of the catalytic foam* 56
Figure IV.4 *Experimental plant set-up*..... 59
Figure IV.5 *Sketch of the experimental plant with details on the reaction section*..... 59
Figure IV.6 *(a) New optimized reactor configuration; (b) Photo of the reactor* 60
Figure IV.7 *Cordierite monolith used to thermally insulate the reactor zones* 61
Figure IV.8 *Experimental set-up for the evaluation of the minimum fluidization velocity* 61
Figure V.1 *Plastic waste sample before (a) and after (b) mechanical grinding* 68
Figure V.2 *TG-MS results on the plastic waste sample: a) TG (weight loss and derivative weight loss) curves; b) MS curves from the plastic sample pyrolysis* 69

Figure V.3 *TGA and DTGA curves for plastic waste pyrolysis at different heating ramp* 70
Figure V.4 *Estimation of activation energy for plastic waste thermal degradation using the Kissinger method*..... 72
Figure V.5 *Results of the ultrasound adherence test on structured catalyst* 73
Figure V.6 *Pore distribution of the samples* 74
Figure V.7 *N_2 at 77K adsorption-desorption isotherms for a) the bare OBSiC foam and b) the catalytic foam*..... 75
Figure V.8 *SEM-EDX images of the fresh sample 40 wt.% Ni/ 30 wt.% CeO_2/ 30 wt.% Al_2O_3/ OBSiC*..... 76
Figure V.9 *H_2 consumption from TPR analysis on 5 catalytic OBSiC foam (40 wt.% Ni/ 8 wt.% Ca/ 30 wt.% CeO_2/ 30 wt.% Al_2O_3)*..... 77
Figure V.10 *CO_2-TPD curves for the fresh and spent 20 wt.% Ni/ 10 wt.% CeO_2/ 30 wt.% Al_2O_3/ OBSiC catalysts and fresh and spent 20 wt.% Ni- 8 wt.% Ca/ 10 wt.% CeO_2/ 30 wt.% Al_2O_3/ OBSiC catalyst*..... 78
Figure V.11 *Isotherms and porous distribution of powder catalyst*..... 80
Figure VI.1 *Results of experimental test under (a) pyrolysis, (b) catalytic pyrolysis, (c) hydrogasification, and (d) catalytic hydrogasification conditions* 83
Figure VI.2 *Gas selectivity in the experimental test* 84
Figure VI.3 *Heating of the reactor with the cordierite monolith used for thermally insulate the two zones of the reactor*..... 86
Figure VI.4 *COMSOL simulation of temperature profiles within cordierite monolith*..... 87
Figure VI.5 *COMSOL simulation of temperature profiles within the reactor* 88
Figure VI.6 *Results of experimental test with a) 50 g and b) 105 g of plastic waste*..... 90
Figure VI.7 *Details of the results of the test with 105 g of plastic waste*.... 91
Figure VI.8 *Coke layer deposited over the catalytic foams* 93
Figure VI.9 *Raman analysis results on coke deposited on the catalytic foams* 94
Figure VI.10 *TPR and CO_2-TPD on regenerated catalyst*..... 95
Figure VI.11 *Methane production in $NmL \cdot min^{-1}$ for the fresh and spent catalyst* 96
Figure VI.12 *a) Weight loss of 90-180 μm alumina particle sample after prolonged fluidization; b) Pressure drops curves for different granulometries of alumina powder*..... 101
Figure VI.13 *Model for the prediction of minimum fluidization velocity of alumina powder and fitting of experimental data with literature models* .. 102
Figure VI.14 *Pressure drops curves of mixtures of alumina (90-180 μm) and plastic waste (180-355 μm)* 104

Figure VI.15 *Prediction of minimum fluidization velocity of mixtures for different volume ratios of alumina (90-180 μm) and plastic waste (180-355) μm* 105
Figure VI.16 *Effect of the dimension of plastic waste particles on minimum fluidization velocity in mixtures of a) 90-180 μm alumina and b) 180-355 μm and at different ratio*..... 107
Figure VI.17 *Experimental minimum fluidization velocity of mixtures of alumina, plastic waste and coke*..... 109

Index of Tables

Table I.1 *Typical gasification reactions* 8
Table II.1 Comparison of the coal-to-SNG technologies (S. Yan et al., 2024) 16
Table II.2 *Summary of the rate-determining steps and the promotional effect of hydrogen spillover (SH) on Fe-, Ni-, and Co-based catalysts during hydrogasification* 26
Table II.3 *Literature studies on Catalytic Hydrogasification* 31
Table II.4 *Literature studies on the catalytic hydrogasification of plastics* 33
Table II.5. *Reactor comparison for plastic thermolysis. Modified from (Qureshi et al., 2020a)* 35
Table II.6 *Values of the two parameters in the correlation for the estimation of* U_{mf} 42
Table II.7 *List of correlations for binary systems* 46
Table II.8 *Literature summary of minimum fluidization velocity of binary mixtures. Rearranged by (Fu et al., 2019)* 47
Table V.1 *Elemental Analysis of the plastic waste sample* 67
Table V.2 *Onset, peak, and final temperatures for the tests on plastic waste at different heating rates* 71
Table V.3 *Peaks temperatures and quantitative results in the* CO_2*-TPD tests* 79
Table V.4 *SSA and porosity properties of powder catalyst* 80
Table VI.1 *Amount of the liquid and solid residues compared to the gaseous fraction* 85
Table VI.2 *Parameters for the assessment of process efficiency* 91
Table VI.3 *Experimental minimum fluidization velocity and dimensionless parameters for different volume ratios of alumina (90-180 μm) and plastic waste (180-355 μm)* 104

Abstract

This PhD project has been focused on the catalytic chemical conversion of plastic waste, an emerging strategy for waste valorization and sustainable energy supply.

The rapid economic development and rising living standards have accelerated the depletion of conventional fossil fuel resources. To mitigate the resulting environmental pollution and meet increasing energy demands, it is crucial to explore alternative and sustainable energy sources. Carbon-based materials and biomass represent viable options in this context. In particular, the catalytic conversion of plastic waste offers a promising pathway to repurpose a resource that would otherwise accumulate in landfills.

Among the available methods for converting carbon-based materials, hydrogasification stands out due to several advantages: it is an exothermic process that requires no additional oxygen, directly produces methane (thus eliminating the need for a separate methanation step), and achieves thermal efficiencies up to 80%. The process generates a methane-rich gas stream that can be readily blended with natural gas in existing distribution pipelines.

Accordingly, this PhD project aims to convert carbon-based materials into methane via catalytic hydrogasification. The main objective of the three-year research activities was the identification of a catalytic system selective for methane production. According to the current state of the art, iron-group metals represent the most effective catalysts for hydrogasification, especially when coupled with basic promoters (e.g., calcium) that mitigate sintering and inhibit the deactivation of the active phase.

The research was structured around several strategic objectives. The first milestone was the identification of an optimal catalytic formulation with high activity and selectivity. The most effective system was found to be a Ni-based structured catalyst, supported on Oxygen Bonded Silicon carbide (OBSiC) foam, and promoted by calcium. The thermally conductive open-cell architecture ensures superior mass- and heat-transfer characteristics, while the dispersed Ni phase provides the active sites responsible for the desired reaction pathway. The Ca acts as a catalytic promoter, contributing to stabilizing the metallic phase and modulating surface acidity. Furthermore, the catalyst enhances the conversion of condensable pyrolysis by-products, promoting their gasification and preventing secondary deposition phenomena.

With a view toward applications at TRL higher than the lab-scale, a reactor scale-up was performed to evaluate process feasibility under higher plastic loadings and to assess catalyst robustness under intensified heat and material transport conditions. Experimental tests feeding up to 105 g of plastic waste yielded methane concentrations up to 59 vol. % in the product gas, with a stable plateau around 50 vol. %. Hydrogen consumption was quantified as 16 kg per ton of plastic waste, while the process delivered a gas yield of

approximately 450 Nm^3 per ton of feedstock, with methane representing about 89% of the product in gas phase. Under these conditions, coke formation was observed, leading to partial degradation of the OBSiC foam structure. Nevertheless, the catalytic system maintained stable methane production, indicating that the active Ni phase remained accessible and that the reaction was not significantly limited by progressive pore blockage or structural damage.

These results confirm the achievement of the methane-rich gas production, demonstrated under catalytic hydrogasification conditions.

The final part of the work was devoted to the systematic investigation of the fluidizability of a binary mixture composed of plastic waste and alumina powder, with the specific objective of supporting the potential transition of the hydrogasification process toward a fluidized-bed configuration. While fluidization is widely studied for inert or mineral systems, limited information is available in the literature on the hydrodynamics of mixtures containing low-density, deformable, and thermally reactive plastic particles.

Fluidization ensures intense solid-solid and solid-gas mixing, promotes uniform temperatures profiles, and enhances mass- and heat-transfer rates. These features make fluidized-bed reactors particularly attractive for catalytic processes, combustion, and gasification, especially when heterogeneous feedstocks as plastic waste.

However, the marked differences in density, particle morphology, and mechanical resistance between plastic particles and conventional bed materials may induce segregation, channeling, and unstable operating regimes.

In this work, a dedicated experimental campaign was carried out to quantify the operating window enabling stable and homogeneous fluidization of plastic–alumina mixtures. The results demonstrated that stable fluidization can be achieved when a suitable alumina-to-plastic volume ratio is adopted and when the two solids exhibit comparable particle size distributions. Under these conditions, segregation phenomena are significantly mitigated, and the system maintains uniform hydrodynamic behavior. Building on the experimental findings, predictive correlations for the minimum fluidization velocity of the binary system were developed and validated against measured data. Unlike conventional correlations derived for spherical or inert particles, the proposed approach accounts for the specific characteristics of plastic-containing mixtures. The resulting model provides a physically grounded tool for reactor design and represents a necessary step toward scaling up the hydrogasification of plastic waste in fluidized bed reactors.

Chapter I.
Introduction: Approaches for the conversion of carbonaceous materials

I.1 Carbonaceous materials and plastics as emerging energy feedstocks

The rapid development of the economy and improved standards of living have led to the deterioration of the availability of traditional fossil fuel resources, whose intensive use has increased the related environmental pollution problems (Weldekidan et al., 2018). The fast population growth, which is expected to lead the world population up to 9.3 billion by 2050 (Morales et al., 2014), has influenced the energy demand, which is expected to increase by about 40% of the current use by 2040 (Cronshaw, 2015).

Therefore, it is essential to explore new sustainable energy sources to mitigate greenhouse gas emissions and support energy demand. Indeed, although a large part of our economy is still based on fossil fuels — specifically coal, oil, and natural gas — the use of solar, wind, geothermal, biomass, hydroelectric, and sea energy has received significant attention over the last decade to diversify the energy market. In most cases, the use of these renewable energy sources is still not economically competitive, and their global spread can be ensured only if allowed by the energy market and national transition policies.

Carbonaceous materials and biomass (such as organic waste streams from agriculture and industry, woody residues from forest harvesting, municipal solid wastes, and plastic wastes) can be a solid alternative for energy supply. In the Net-Zero Emission (NZE) Scenario, these advanced bioenergy feedstocks that do not require land will provide 60% (compared to 20% today)

of the 100 EJ of global bioenergy supply in 2050. Of these sustainable waste streams, forestry residues from wood processing and forest harvesting provide 20 EJ, while various sustainable waste streams outside of the forestry sector provide the remaining 40 EJ (Energy Agency, 2021).

Biomass consists of natural organic materials, either from plant or animal sources, that represent a possible way to produce chemicals and energy fuels (K. Lee et al., 2022). One of the most abundant biomass resources on earth is represented by lignocellulosic biomass (mainly constituted of cellulose, hemicellulose and lignin, with a small amount of ash and extracts), with more than 100 billion metric tons of agricultural and forestry residues produced annually (Abbasi & Abbasi, 2010). This resource is considered carbon-neutral because it takes carbon from the atmosphere and returns it after conversion to multifunctional products.

When considering other carbonaceous materials, plastic stands out for its numerous applications, thanks to its low cost, light weight, durability, chemical resistance, and ease of processing. Among thermoplastics, polyethylene (PE) is the most widely produced, with a global production of 125 million tons per year, followed by polypropylene (PP) at 69 million tons per year (K. Lee et al., 2022). One more common plastic is polyvinyl chloride (PVC), which has a global production of 39 million tons per year and requires a dichlorination step before depolymerization due to its halogen content.

In 2020, global plastic production reached 367 million tons, with China accounting for 32%, NAFTA (North American Free Trade Agreement) countries for 18%, the rest of Asia for 17%, Europe for 15%, the Middle East and Africa for 7%, Latin America for 4%, Japan for 4%, and the CIS (Commonwealth of Independent States) countries for 3% (Plastics-the Facts 2019 An Analysis of European Plastics Production, Demand and Waste Data, n.d.). Projections suggest that plastic production will rise to 1.1 billion tons by 2050, leading to an increase in plastic waste, with an estimated 12 billion tons expected to be disposed of in landfills by that time (Geyer et al., 2017).

Currently, of the 8,600 million tons of plastic ever produced, 59% has been discarded, ending up in landfills or accumulating in the natural environment, including oceans. Only 17% has been recycled or incinerated for energy recovery. In response to this issue, European governments have focused on improving waste collection and conversion technologies. In 2021, the European Union and associated countries collected 29.5 million tons of post-consumer plastic waste, achieving a 117.7% increase in recycling rates, a 77.1% rise in energy recovery, and a 46.6% reduction in landfill disposal compared to 2006. Future targets aim for “zero landfilling” to facilitate a circular economy for plastics.

The potential of plastics as an alternative energy resource is demonstrated by their higher carbon (78-85 wt%) and hydrogen (8-15 wt%) contents as compared to biomass, such as rice straw and cotton stalk (C:43-45 wt%; H: ~6 wt%) (Nam & Capareda, 2015). Moreover, the high heating value (HHV)

of plastic waste is as high as 40-46 $MJ \cdot kg^{-1}$, which is similar to that of kerosene (46.5 $MJ \cdot kg^{-1}$) and diesel (45.7 $MJ \cdot kg^{-1}$) (S. Wang et al., 2021).

The conversion of these feedstocks into energy and chemicals is attracting growing attention from both the scientific community and industry. In particular, the conversion of plastic waste represents a promising route for valorizing a resource that would otherwise be landfilled, contributing to the broader goal of a carbon-neutral and waste-free society (K. Lee et al., 2022).

The core of this three-year project has been the proposal and investigation of some innovative solutions to valorize carbonaceous materials. The results achieved will be discussed in this dissertation.

I.2 Technologies for the conversion of carbonaceous materials and biomass

A viable strategy for valorizing landfill-bound waste is its conversion into energy, fuels, or chemical products. Thermochemical routes such as pyrolysis and gasification can be employed for this purpose, as they build upon technologies originally developed for biomass conversion, owing to the comparable organic nature and similar reaction pathways of plastics and lignocellulosic feedstocks (K. Lee et al., 2022).

Several conversion methods are available for efficiently transforming carbonaceous materials into energy carriers and chemical products. Raw biomass, in particular, can be processed through several routes—including combustion, pyrolysis, gasification, torrefaction, liquefaction, esterification, and fermentation (Weldekidan et al., 2018).

These technologies are generally classified into three main categories: i) thermochemical processes, which use heat to break down feedstocks; ii) biological processes, which exploit microorganisms or enzymes to convert organic matter into fuels or platform chemicals (e.g., anaerobic digestion, fermentation); and iii) physical conversion methods, which involve mechanical treatments such as size reduction, densification, squeezing, or extraction. Both biomass and plastics have historically been treated using these approaches and continue to be processed through them today.

The following section focuses on pyrolysis and gasification, the two most widely employed thermochemical conversion pathways.

I.2.1 Pyrolysis

In pyrolysis, heavier hydrocarbon molecules are broken down into smaller hydrocarbon molecules, condensable gases, and solid carbon as char (eq. ((1)), through a thermochemical decomposition (**Figure I.1**). The condensable gas may break down further into non-condensable gases, such as CO, CO_2, H_2, and CH_4.

$$C_nH_mO_p + heat \rightarrow \sum_{liquid} C_aH_bO_c + \sum_{gas} C_xH_yO_z + \sum_{solid} C \quad (1)$$

The pyrolysis method stands out as particularly promising because it operates without the need for oxygen, enabling the conversion of organic waste into various fuels or chemicals, including gaseous and liquid fuels, and solid carbon, at temperatures ranging from 400 to 700 °C. The key distinction between pyrolysis and other thermochemical conversion routes is its ability to convert waste predominantly into liquid oils and waxes, which can be readily stored, transported, and flexibly used as energy carriers or chemical intermediates (Qureshi et al., 2020a).

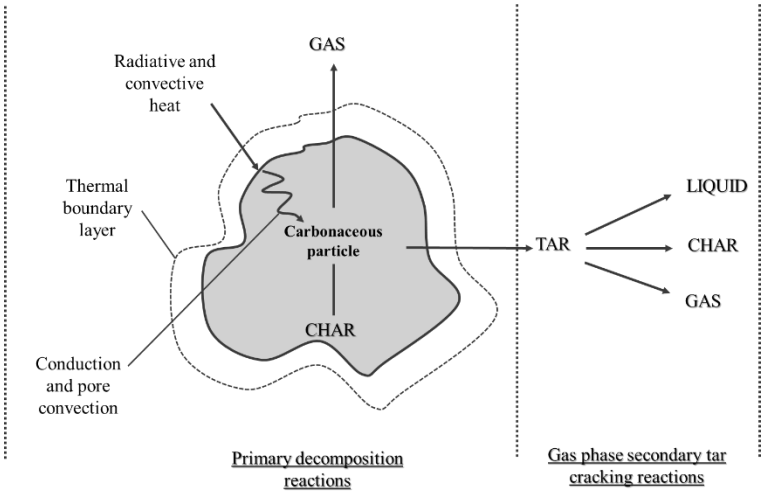


Figure I.1 *Pyrolysis process (reproduced from (Basu Prabir, 2013)*

Although pyrolysis oil is the target product in most cases, the process conditions can be adjusted to obtain either liquid or gaseous products as the outcome (Qureshi et al., 2020b). The distribution of products is influenced by reaction temperatures (thermodynamics) and heating/cooling rates (kinetics). Presently, the primary objective is to maximize the bio-oil fraction, which is achieved through flash or fast pyrolysis, characterized by a heating rate exceeding 1000 °C·s^{-1} and a residence time of less than 1 second (K. Lee et al., 2022). Opposite reaction conditions (residence time of hours or days) are used in the slow pyrolysis which target product is the solid carbon or bio-char) (K. Lee et al., 2022).

Figure I.2 shows a simplified layout of a biomass pyrolysis plant equipped with a fluidized bed reactor. The biomass is fed into the heated reactor, and the thermal decomposition releases condensable and non-condensable vapors, which leave the chamber. The solid char produced remains partly in the chamber and partly in the gas from which is separated and cooled downstream of the reactor. The condensable vapor condenses as bio-oil or pyrolysis oil.

The non-condensable gases leave the chamber as product gas, which is the product of interest. Regarding the solid char, it can be collected as a commercial product or burned in a separate chamber to produce heat for pyrolysis or used as fluidizing agent, since it is free from oxygen.

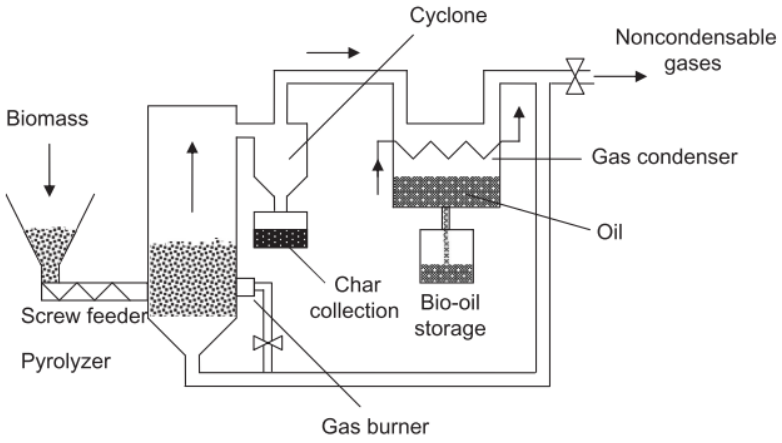


Figure I.2 *Simplified layout of a pyrolysis plant*

This technology has some drawbacks, such as the high temperatures required for molecular cracking and the low quality of the produced liquid oils. To address these issues and enhance the quality and consistency of pyrolysis products, one strategy involves the co-pyrolysis of biomass and waste plastics. Waste plastics have a high hydrogen-to-carbon (H/C) ratio and a relatively low oxygen-to-carbon (O/C) ratio, while the opposite is for biomass. Combining their effects, biomass can be deoxidized by the hydrogen-rich plastics, resulting in an improved quality of bio-oils and other products. This synergy reduces oxygen content and increases the energy density of the final liquid fuels, making them more comparable to conventional fossil fuels.

Additionally, plastics help to stabilize the pyrolysis process, reducing issues like tar formation commonly associated with biomass pyrolysis. This results in a higher yield of valuable products, such as syngas and biochar, and minimizes the formation of undesired byproducts. Co-pyrolysis also contributes to waste management by utilizing both biomass (renewable organic waste) and plastic waste, which is often challenging to recycle through other means. This combined approach enhances the economic viability of the process and supports circular economy goals (Mo et al., 2023; Yek et al., 2024)

Moreover, advancements in catalytic co-pyrolysis further improve the process by selectively producing higher-quality chemicals and fuels, optimizing both the environmental and economic outcomes of waste

management and energy recovery (Guo et al., 2023). In particular, during the co-pyrolysis, the waste plastics provide hydrogen donors and produce hydrocarbons which react with biomass-derived radicals to form more hydrocarbons and oxides such as alcohols and ketones (Al-Maari et al., 2021; Terry et al., 2023). In recent years, several studies (R. Chen et al., 2020; Guo et al., 2023; Y. Wang et al., 2021) have been focused on different aspects of co-pyrolysis, such as kinetics, thermal behaviour, product yields (oil yield is favoured) and synergic effects, concluding that activation energy required for co-pyrolysis of the mixture was lower than that of waste plastic but higher than solid biomass.

I.2.2 Gasification

Gasification involves the conversion of solid or liquid feedstock into gaseous fuel or chemical products that can be burned to release energy or employed to produce value-added chemicals (Basu Prabir, 2013). In particular, the process uses high temperatures, typically above 700°C, along with a controlled amount of oxygen (air) or steam to break down feedstocks into syngas, primarily composed of carbon monoxide (CO), carbon dioxide (CO_2), and hydrogen (H_2). The main goal in this process is to maximize the production of useful gases like hydrogen, which can improve the overall efficiency of the system, especially in energy generation or chemical production. Minimizing tar formation is also crucial, as tars can cause operational issues such as clogging and reduce the efficiency of gasification systems. Therefore, reducing tar is a key focus during the process design, often achieved through different techniques, including the optimization of the operating conditions or the use of catalysts (K. Lee et al., 2022).

Figure I.3 shows a typical biomass gasification process, which includes the following steps: i) drying; ii) thermal decomposition or pyrolysis; iii) partial combustion of some gases, vapors, and char; iv) gasification of decomposed products. In a typical gasification process, the biomass is first heated and dried, after which it undergoes thermal degradation (pyrolysis). The resulting pyrolysis products—gases, vapors/liquids, and char—then react both among themselves and with the gasifying agent to generate the final syngas. In most commercial gasifiers, the heat required for drying, pyrolysis, and the subsequent endothermic reactions is supplied by a controlled fraction of exothermic combustion occurring within the reactor.

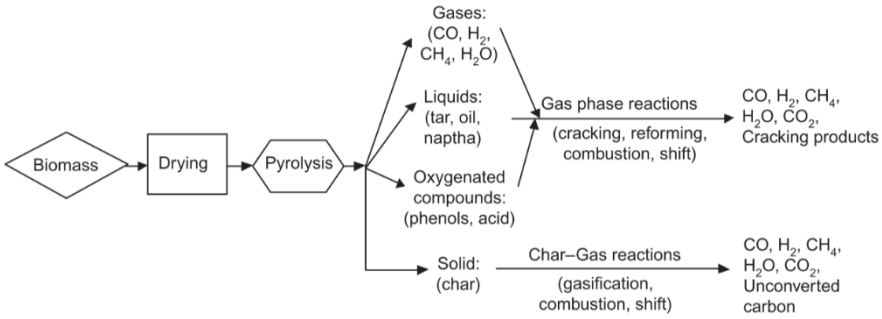


Figure I.3 *Reaction sequence and potential paths for gasification*

When gasification is preceded by pyrolysis, the process can become more efficient. Pyrolysis, which is endothermic, produces intermediate products like gas, tar, and char. In the subsequent gasification phase (which is exothermic), partial oxidation of the more complex hydrocarbons in the tar and char further enhances these outputs. This additional oxidation breaks down the heavier hydrocarbons, improving the overall yield of syngas.

Table I.1 *Typical gasification reactions*

Reaction Type	Reaction
Carbon Reactions	
R1 (Boudouard)	$C + CO_2 \rightleftharpoons 2CO + 172\ kJ \cdot mol^{-1}$
R2 (water-gas or steam)	$C + H_2O \rightleftharpoons CO + H_2 + 131\ kJ \cdot mol^{-1}$
R3 (hydrogasification)	$C + 2H_2 \rightleftharpoons CH_4 - 74.8\ kJ \cdot mol^{-1}$
R4	$C + 0.5O_2 \rightleftharpoons CO - 111\ kJ \cdot mol^{-1}$
Oxidation Reactions	
R5	$C + O_2 \rightarrow CO_2 - 394\ kJ \cdot mol^{-1}$
R6	$CO + 0.5O_2 \rightarrow CO_2 - 284\ kJ \cdot mol^{-1}$
R7	$CH_4 + 2O_2 \rightarrow CO_2 + 2H_2O - 803\ kJ \cdot mol^{-1}$
R8	$H_2 + 0.5O_2 \rightarrow 2H_2O - 242\ kJ \cdot mol^{-1}$
Shift Reaction	
R9	$CO + H_2O \rightleftharpoons CO_2 + H_2 - 41.2\ kJ \cdot mol^{-1}$
Methanation Reaction	
R10	$2CO + 2H_2 \rightleftharpoons CH_4 + CO_2 - 247\ kJ \cdot mol^{-1}$
R11	$CO + 3H_2 \rightleftharpoons CH_4 + H_2O - 206\ kJ \cdot mol^{-1}$
R14	$CO_2 + 4H_2 \rightleftharpoons CH_4 + 2H_2O - 165\ kJ \cdot mol^{-1}$
Steam-Reforming Reactions	
R12	$CH_4 + H_2O \rightleftharpoons CO + 3H_2 + 206\ kJ \cdot mol^{-1}$
R13	$CH_4 + 0.5O_2 \rightleftharpoons CO + 2H_2 - 36\ kJ \cdot mol^{-1}$

Table I.1 lists some of the important chemical reactions taking place in a gasifier.

In general, the outputs of the gasification process are:

1. Solid (30-50% of input weight): composed mainly of non-volatile metals and other inorganic materials, which form ash.

2. Liquid (10-20% of input weight): this consists of small amounts of oils and tar.
3. Gas: Similar to pyrolysis gas but with a higher concentration of CO_2, as more complete oxidation occurs compared to pyrolysis alone.

This multi-stage approach improves conversion efficiency and ensures better quality of the final products, particularly the gaseous components. Depending on the weight of the supply, the gas yield can range from 30 to 60% (Shah et al., 2023).

The heating value of the gas produced during gasification varies significantly based on the gasification agent used, for example in the case of oxygen the typical heating value is between 3 and 12 $MJ \cdot Nm^{-3}$. When air or oxygen-enriched air is employed, inert nitrogen enters the gasifier and dilutes the product gas, reducing its calorific value and making it less suitable for many applications. Another established approach is to use pure oxygen as the oxidant. This produces a product gas essentially free of nitrogen, although it still contains some carbon dioxide. The main drawback of this method is the need for an air-separation unit to supply the required oxygen, which increases both capital and operating costs. The choice of gasification agent (oxygen, air, or steam) plays a crucial role in determining the composition of the produced syngas, affecting the relative concentrations of gases like hydrogen (H_2), carbon monoxide (CO), and carbon dioxide (CO_2).

Regarding reactor types, gasifiers are generally categorized into two main designs:

- Fixed-bed reactors: These are the most commonly used, particularly in their updraft and downdraft configurations, due to their simplicity, ease of operation, and low investment cost. However, they come with limitations such as difficulties in scaling up, suboptimal gas–solid contact, challenges with continuous operation, and low heat transfer rates.
- Fluidized-bed reactors: Though more complex, these reactors offer better gas–solid mixing, higher heat transfer rates, and improved process efficiency. However, they are more expensive to design and operate (Tezer et al., 2022).

I.3 An alternative process: the hydrogasification

Although well-established, the technologies described above present several drawbacks, mainly associated with the composition of the resulting product gas and the operating temperatures required.

Hydrogasification is a particular form of gasification that operates in a hydrogen-rich environment to process carbon-based fuels, like coal. This method has historical significance, with its first major use dating back to the 1930s. Germany, the United States, and Great Britain explored this technology to address fuel shortages, particularly for gas and liquid fuels. In subsequent

years, hydrogasification became part of broader gasification processes such as steam reforming and partial oxidation. A notable application was Germany's use of the Fischer-Tropsch process during World War II to convert coal into high-octane gasoline, a crucial resource when traditional petroleum supplies were limited. Similarly, during the international embargo against South Africa due to Apartheid, the country employed this technology to produce fuel from coal, ensuring a domestic supply of energy resources despite global restrictions (Tosti et al., 2016).

The hydrogasification process remains relevant today because of its ability to convert carbon-rich feedstock into methane-rich gases, offering a pathway toward cleaner and more flexible energy production (Tosti et al., 2016).

Coal hydrogasification is a well-established technology, and recent studies have highlighted its potential in energy storage applications (Tosti et al., 2016). This process has been explored as a method to produce substitute natural gas (SNG), a methane-rich gas, from various low-value materials like wood biomass, agricultural waste, and plastics. Such approaches not only enhance the energy value of these materials but also provide a sustainable strategy for converting waste into valuable fuel, contributing to circular economy practices.

Additionally, hydrogasification can be employed as a form of energy storage, where the produced SNG can act as a versatile fuel source for periods of high demand.

The energy content of methane can be highlighted by comparing its combustion with that of carbon, as reported in eq (2)(2) and eq (3):

$$CH_4 + 2O_2 \rightarrow CO_2 + 2H_2O(g) \qquad \Delta H^0_{298K} = 802\ kJ \cdot mol^{-1} \qquad (2)$$

$$C + O_2 \rightarrow CO_2 \qquad \Delta H^0_{298K} = 393\ kJ \cdot mol^{-1} \qquad (3)$$

To summarize the key advantages of coal hydrogasification:

- Exothermic process: coal hydrogasification is exothermic, meaning it generates heat, eliminating the need for external oxygen or additional heating sources.
- Direct production of methane: the process directly produces methane (synthetic natural gas, SNG) without requiring a separate methanation step, simplifying the overall operation and reducing costs.
- High thermal efficiency: the process can achieve a thermal efficiency up to 80%, making it highly efficient in terms of energy conversion.

These factors contribute to its attractiveness as an energy production method, particularly for converting low-value materials into high-value fuels like substitute natural gas (L. Yan et al., 2014).

The primary challenge to the industrial adoption of hydrogasification is the cost of hydrogen. However, interest in this technology could rise with the availability of low-cost hydrogen.

Currently, hydrogen is produced through thermochemical processes like reforming and partial oxidation, which are efficient and cost-effective but

have a high global warming potential, with steam reforming emitting around 8 kg CO_2eq per kg of hydrogen (Bhandari et al., 2014). Other methods, such as alkaline water electrolysis, are well-known but remain expensive due to their high electricity consumption, resulting in more than 30 kg CO_2eq per kg of hydrogen. An alternative is water electrolysis powered by wind energy during off-peak hours, which significantly lowers the carbon footprint to less than 2 kg CO_2eq per kg of hydrogen. This method also produces high-purity oxygen (>99%), which has numerous applications in industries such as welding, metal production, pharmaceuticals, biotechnology, water treatment, and refining, as well as in medical and healthcare sectors. Electrolysis produces high-purity oxygen (>99%) which could be used in industries (welding and metal production, pharmaceutical and biotechnology, water treatment, refining) as well as in medicine and healthcare.

This PhD project is focused on the study of the conversion of carbonaceous materials, in particular plastic waste, into a methane-rich gaseous product by means of the catalytic hydrogasification process.

Chapter I

Chapter II.
State of the art

II.1 Overview of the coal and biomass hydrogasification process

The hydrogasification process includes several reactions depending on the assumptions (thermodynamics and kinetics) and on the characteristics of the feedstocks chosen. The reaction of carbon hydrogasification is reported in eq. (4).

$$C + 2H_2 \rightleftharpoons CH_4 \qquad \Delta H^0_{298K} = -75\ kJ \cdot mol^{-1} \tag{4}$$

Considering the composition of coal/carbonaceous materials ($C_aH_bO_cN_dS_e$) which includes carbon and other elements (hydrogen, oxygen, nitrogen, sulfur, etc.), a realistic reaction scheme of the coal hydrogasification process consists of three steps (Xuan et al., 2023; L. Yan et al., 2014) (Barbuzza et al., 2019):

i) the drying process of the original feedstock;
ii) the pyrolysis of the dried feedstock, which generates volatiles (mainly CO, CO_2, CH_4, C_6H_6, N_2, H_2S, SO_2, H_2, H_2O), separating them from the char (solid carbon);
iii) a series of gasification reactions of both char and volatile.

The temperature reached by the hydrogasification reactor ranges from 800°C to 1000°C.

Along with the reaction of hydrogasification, the other main reactions that involve the char gasification are the steam reforming (eq. (5)) and the Boudouard equilibrium (eq. (6)):

$$C + 2H_2O \rightleftharpoons CO + H_2 \qquad \Delta H^0_{298K} = 131\ kJ \cdot mol^{-1} \tag{5}$$

$$C + CO_2 \rightleftharpoons 2CO \qquad \Delta H^0_{298K} = 172\ kJ \cdot mol^{-1} \tag{6}$$

The volatiles can react in the following reactions (eqs. (7-(11)):

$$CO + H_2O(g) \rightleftharpoons CO_2 + H_2 \qquad \Delta H^0_{298K} = -41\ kJ \cdot mol^{-1} \tag{7}$$

$$CO_2 + 4H_2 \rightleftharpoons CH_4 + 2H_2O \qquad \Delta H^0_{298K} = -165\ kJ \cdot mol^{-1} \qquad (8)$$

$$C_6H_6 + 6H_2O \rightleftharpoons 6CO + 9H_2 \qquad \Delta H^0_{298K} = 739\ kJ \cdot mol^{-1} \qquad (9)$$

$$C_6H_6 + 8H_2 \rightleftharpoons 4CH_4 + C_2H_6 \qquad \Delta H^0_{298K} = -433\ kJ \cdot mol^{-1} \qquad (10)$$

$$C_2H_6 + 2H_2O \rightleftharpoons 2CO + 5H_2 \qquad \Delta H^0_{298K} = 347\ kJ \cdot mol^{-1} \qquad (11)$$

The reducing environment allows to increase the formation of methane at the expense of CO and CO_2.

The water gas-shift reaction controls the presence of carbon monoxide, which is a by-product of the hydrogasification process. Indeed, when the temperature is above 300 °C the equilibrium is shifted towards CO and water production. Therefore, a successive step of CO methanation is necessary to further lower the CO concentration (eq. (12)) in the product stream, even if the excess of hydrogen avoids the formation of heavier hydrocarbons and reduces the CO formation.

$$CO + 3H_2 \rightleftharpoons CH_4 + H_2O(g) \qquad \Delta H^0_{298K} = -206\ kJ \cdot mol^{-1} \qquad (12)$$

A schematic representation of the basic hydrogasification process is reported in Figure II.1 and the general reaction of the process is reported in eq (13).

$$C_xH_yO_z + \alpha H_2 \rightarrow a\ CH_4 + b\ CO + c\ CO_2 + d\ H_2 + eH_2O + other\ products \qquad (13)$$

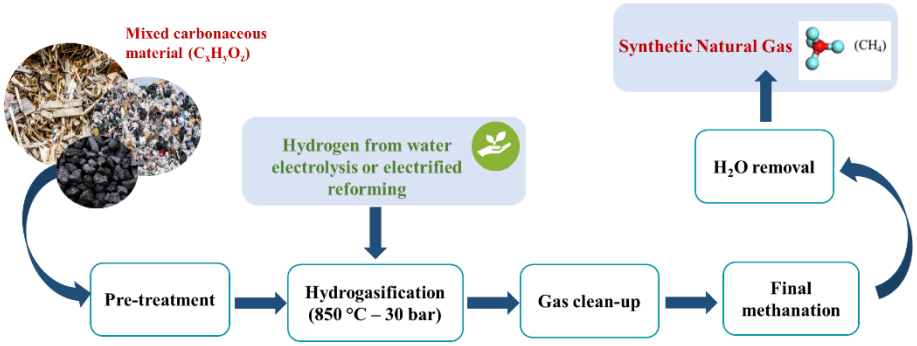


Figure II.1 *Scheme of the hydrogasification process*

At the end of the process, the final product is SNG, consisting of methane with hydrogen plus minor impurities. The presence of hydrogen in methane up to 28 vol.% is safe to be used with properly serviced existing domestic appliances (Melaina et al., 2013), while its blending with methane in the range 20-30 vol% is the most suitable for internal combustion engines. In order to meet the regulatory requirements for SNG into the grid, CO_2 separation step is needed, using absorption in chemical solvents such as aqueous solution of amines (mono-, di- and tri-amine, di-isopropanol amine, etc.), pressure swing

adsorption in packed columns filled with molecular sieves or activated carbons, use of selective membranes, cryogenic processes, or calcium looping CO_2 capture (Tosti et al., 2016). The water, mainly produced by the reaction of hydrogen with oxygen contained in the biomass, can be removed by condensation, while the ammonia can be removed in an upgrading section to make the SNG able to meet the specifications required by the regulations of the methane grid (Barbuzza et al., 2019).

Since the equilibrium reaction in eq. (4) is exothermic, methane formation is favored at lower temperatures. Conversely, higher temperatures promote the equilibrium toward CO production, according to the Boudouard equilibrium and the steam reforming reactions (which also favour the hydrogen production at the expense of methane yield). Moreover, because methanation reactions involve a decrease in the total number of moles, Le Chatelier-Braun's principle indicates that increasing the pressure further promotes methane yield. Therefore, typical operation conditions consist of low temperatures (~300°C, although the initial pyrolysis step must still reach temperatures sufficient to release volatiles) and high pressure (30 bar, which promotes higher carbon-conversion efficiencies, particularly when the reaction temperature is increased).

II.2 Catalytic hydrogasification

The main drawback of the non-catalytic thermochemical technologies developed to transform biomass or plastic waste into chemicals, heat and materials is the low selectivity towards high-quality products. A catalyst can improve the process economics by shifting the reaction conditions to milder temperatures and lower pressures and selectively enhance the formation of methane or other desired products (K. Lee et al., 2022).

Several studies have investigated the use of a catalyst for the hydrogasification of coal; very few research studies have focused on the catalytic conversion of plastics by means of the hydrogasification process.

In this paragraph, the literature review will discuss the studies on coal conversion and the performances of different catalysts for the hydrogasification.

II.2.1 Literature on the catalytic coal hydrogasification

Compared with existing coal-to-SNG technologies (Table II.1)—such as two-stage gasification (Lurgi gasifier), catalytic coal gasification, and conventional coal hydrogasification—catalytic hydrogasification offers clear advantages, including higher CH_4 yields and improved thermal efficiency (S. Yan et al., 2017). In addition, the catalytic hydrogasification process generates larger quantities of high-value hydrocarbon liquids (HCL), such as BTX (benzene, toluene, xylenes), PCX (phenol, cresols, xylenols), and naphthalene, further enhancing the competitiveness of the technology (Yuan

et al., 2017). As a result, catalytic coal hydrogasification (CCHG) has attracted considerable attention over the past decades, and significant efforts have been devoted to developing efficient and economically viable catalysts.

Table II.1 Comparison of the coal-to-SNG technologies (S. Yan et al., 2024)

Process	**Lurgi (Z. Chen et al., 2017)**	**CCG (Yuan et al., 2017)**	**GHG**	**CCHG (S. Yan et al., 2017)**
Reactor	Fixed bed	Fluidized bed	Entrained-flow bed	Fluidized bed
Catalyst	No	K_2CO_3	No	Co and Ca nitrate
Particle	Lump coal	Powder coal	Powder coal	Powder coal
Gasifing agent	H_2O	H_2O	H_2	H_2
Temperature (°C)	900-1000	700	900-1100	850
Pressure (MPa)	2.0-4.0	3.5	5.0-7.0	3.0
Residence time	1-3 h	2 h	15-20 s	0.5 h
Carbon conversion	~99%	~95%	~50%	90%
CH_4 yield	~20.3%	~33.3%	~35.0%	77.3%
CH_4 production (Nm^3/kg coal)	0.32	0.52	0.55	1.11
CO_2 emission (g/mol CH_4)	72.64	44.84	36	38.25
Catalyst recovery	-	~87.6%	-	>99%
Thermal efficiency	61.9%	72.7%	79.6%	81.8%

Table II.3 shows a summary of the principal studies on catalytic hydrogasification.

Iron group metals-based catalysts

Iron group metals have been widely investigated since they provide active hydrogen and decrease the binding energy of C-C bond for coal hydrogasification (Matsumoto, 1991; S. Yan et al., 2018), with activity typically following the order Co > Ni > Fe (F. Zhang et al., 2019). However, these metals are prone to deactivation at high temperatures due to coke deposition, sulfur poisoning, and sintering (Murakami et al., 2000). For this reason, an alkaline-earth promoter, such as calcium, is commonly introduced to mitigate sintering of iron group metals and reduce susceptibility to poisoning. The alkaline promoters are able to modify the catalytic behaviour of iron group metals, enabling performances comparable to those of more expensive noble metals such as Rh or Pt (Haga & Nishiyama, 1987). In particular, calcium compounds enhance metal dispersion on coal and strengthen metal-carbon interactions (S. Yan et al., 2021).

Therefore, the combination of an iron-group metal with an alkaline-earth promoter provides an effective compromise between catalytic activity and economic viability. In this paragraph, a review of the literature studies on Ni, Co and Fe-based catalysts is presented.

Matsumoto et al. (Matsumoto, 1991) reported a marked enhancement in hydrogasification rates when a supported nickel hydrogenation catalyst was blended with metal-loaded char. Their study employed 0.5 g of char derived from Australian Yallourn brown coal, characterized by low ash and sulfur content, crushed to 32/60 mesh and subsequently demineralized using HCl at 80 °C. Iron, nickel, and cobalt were introduced onto the demineralized coal via wet impregnation with aqueous metal nitrate solutions, followed by heat treatment under argon at 850 °C for 30 minutes. The catalyzed char was then mixed with 0.5 g of a commercial Ni/diatomite catalyst (45 wt% Ni, ground to 150 mesh). Experiments were carried out at atmospheric pressure in a micro-flow quartz reactor using a hydrogen flow of 100 mL $\cdot min^{-1}$.

Tests performed with 0.8 wt. % metal-loaded char confirmed the activity trend Co > Ni > Fe at 820 °C. The initially low reactivity was attributed to sulfur traces in the coal, which chemisorbed on the catalyst surface and temporarily inhibited activity. When the metal loading was varied, catalytic effects became noticeable at levels as low as 0.1 wt. % for all metals. Above 0.2 wt. %, however, further increases in loading produced only modest improvements. For iron, the gasification rate reached a plateau already below 0.1 wt. %, whereas cobalt showed its highest activity only beyond 0.5 wt. % loading. Fe_3C is often found in the catalyzed coal chars, whereas no Co or Ni carbide was formed; instead, they existed in the metallic state. (F. Zhang et

al., 2019) reported that Fe_3C constitutes the active phase during catalytic hydrogasification; however, the overall activity of iron remains limited because carbon binds to Fe through a predominantly ionic interaction, forming a bond that is too strong to be rapidly hydrogenated. In contrast, on Co and Ni catalysts carbon accumulates on the surface in a more weakly bound, dissolution-like state, which can be readily hydrogenated by activated hydrogen species. As a result, cobalt and nickel exhibit markedly higher hydrogasification activity than iron (Haga et al., 1992). Overall, cobalt consistently delivered the best performance, followed by nickel and iron.

Eqs. (14-16) presents the principle of Fe/Co/Ni-catalyzed hydrogasification of model carbon (MC):

$$H_2 \rightarrow H\cdot + H\cdot \tag{14}$$

$$C=C \xrightarrow{bonds\ breaking} C[bulk] + Fe \rightarrow Fe_3C + H\cdot \rightarrow Fe + CH_4 \tag{15}$$

$$C=C \xrightarrow{bonds\ breaking} C[bulk] \rightarrow C[Co/Ni\,, dissolved] \rightarrow C[ad] + H\cdot \rightarrow CH_x[ad] + H\cdot \rightarrow CH_4 \tag{16}$$

Introducing Ni/diatomite alongside the metal-loaded char not only accelerated the hydrogasification rate but also shortened the initial low-reactivity period, indicating that the commercial catalyst helped remove chemisorbed sulfur from the active sites. At elevated temperatures, catalyst deactivation was observed, and the rate enhancement diminished. Comparison with tests conducted without Ni/diatomite showed that the presence of the commercial catalyst allowed the reaction temperature to be reduced by approximately 200 °C for cobalt-loaded char (hydrogasification occurring at 570 °C), and by about 150 °C and 100 °C for iron- and nickel-loaded char, respectively. Importantly, the dependence of reaction rate on metal loading remained essentially unchanged, suggesting that Ni/diatomite boosts the intrinsic activity of iron-group metals without altering the reaction mechanism or catalyst dispersion.

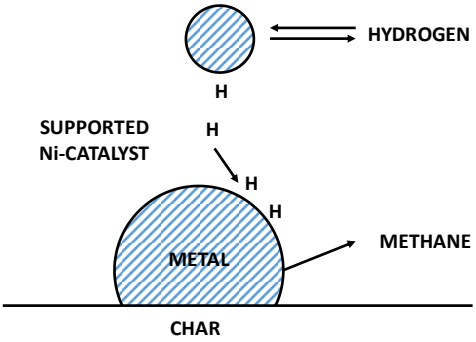


Figure II.2 *Schematic diagram of H_2 atoms spillover in the supported hydrogenation Ni catalysts and iron group metal loaded char system*

To clarify the synergistic effect between Ni/diatomite and iron-group metal catalysts, the authors highlighted that the Ni/diatomite itself is catalytically active: it improves the overall performance—even when nickel is already present—and helps remove sulfur species from the catalyst surface. This occurs because Ni/diatomite particles are in intimate contact with the iron-group metal particles dispersed on the char. As a result, hydrogen atoms dissociated on the supported nickel catalyst can migrate ('spill over') to the adjacent catalytic sites (Figure II.2). A similar spillover mechanism may also allow hydrogen atoms to reach the carbon matrix directly, facilitating C–C bond cleavage.

Several studies have extensively investigated the use of calcium as a promoter.

Haga et al., 1992 and Yan et al., 2022d showed that the bimetallic catalyst 5wt%Co-5wt%Ca exhibited higher activity than Ni-Ca and Fe-Ca in the hydrogasification of bituminous coal, due to its superior ability to break C-C bonds. The Co–Ca catalyst was found to enhance coal devolatilization, suppress the graphitization of the coal matrix, and generate additional active sites on the char surface during hydropyrolysis. Several studies have also identified an optimal calcium loading of around 1.0 wt.% (J. Feng et al., 2023; Qu et al., 2019; S. Yan et al., 2017; Yuan et al., 2017).

Yan et al. (S. Yan et al., 2018) investigated coal hydrogasification in a pressurized fluidized-bed reactor using a cobalt–calcium bimetallic catalyst (Co–Ca) prepared via co-impregnation. The catalyst contained 5 wt.% Co and 1 wt.% Ca, and the reactor was operated with 50 g of char and a hydrogen flow of 11.7 $L \cdot min^{-1}$. Their results showed that the Co–Ca catalyst significantly enhanced coal depolymerization and hydrogenation during hydropyrolysis. Carbon conversion increased markedly—from 43.4 wt.% for raw coal under H_2 to 91.3 wt.% when Co–Ca was present—and similar improvements were observed in methane and tar production. These findings indicate that only the

combined action of Co–Ca and hydrogen is capable of cleaving the C–C bonds in the condensed aromatic structures of coal, whereas neither component alone produces a comparable effect. The maximum methane formation rate reached 66.8 mL·(min·g_{coal})$^{-1}$ with Co–Ca in H_2, substantially higher than the 39.2 mL·(min·g_{coal})$^{-1}$ obtained under pyrolysis conditions. In addition, the Co–Ca/H_2 system achieved a CH_4 yield of 77.3 wt.% within 30 min. Based on these observations, the authors concluded that at temperatures above 800 °C and pressures around 3 MPa, the dominant step in Co–Ca-catalyzed hydrogasification is the cleavage of C–C bonds, facilitated by the catalyst, which both lowers the activation energy of this step and provides the hydrogen required for the reaction. They also noted that hydrogen spillover was not the rate-limiting step. According to their proposed mechanism, the initial stage involves hydrogenation of small, reactive aromatic units, while the more stable condensed rings undergo catalytic cracking promoted by the synergistic action of Co–Ca and hydrogen**.**

In a subsequent study (Qu et al., 2019), the authors evaluated how different Co–Ca loadings affected product distribution. With 5 wt.% Co–1 wt. % Ca at 850 °C and 3 MPa, they achieved 90 wt.% carbon conversion and 77.3 wt.% CH_4 in 30 min. Increasing Co content reduced light-tar yields, whereas higher Ca loadings increased them. Heavy-tar production was highest with 5 wt. % Co–2 wt. % Ca, attributed to enhanced C–C bond cleavage and partial secondary hydrocracking of heavy volatiles. Calcium loadings of 1–2 wt. % also enabled methane formation rates above 70 mL· (min· g_{coal})$^{-1}$.

These findings reinforce the potential of Co–Ca-catalyzed hydrogasification for SNG production, although the high cost of cobalt remains a significant economic limitation. To address this issue, Feng et al. (J. Feng et al., 2023) proposed an HNO_3-based leaching process capable of recovering Co and Ca with efficiencies exceeding 99%. Nonetheless, the regenerated catalyst gradually lost activity with repeated cycles due to the buildup of impurities—especially aluminium.

Feng et al. (J. Feng et al., 2022) examined Co–Ca-catalyzed coal hydrogasification using H_2 and H_2/CO_2 mixtures. A 3 wt. % Co – 2 wt. % Ca catalyst, prepared by impregnating coal with cobalt and calcium acetates, was tested in a fluidized-bed reactor at 850 °C and 3.5 MPa. Adding 10 vol. % CO_2 increased total gas and water yields but reduced CH_4 by 22.6%, while CO and CO_2 formation rose. Despite the high temperature, the Co–Ca catalyst still promoted CO_2 methanation. The maximum CH_4 formation rate with H_2/CO_2 was 34.6 mL·(min·g_{coal})$^{-1}$ lower than in pure H_2, but unlike the H_2 case — where the rate dropped to zero after 40 min —it stabilised around 23 mL·(min·g_{coal})$^{-1}$ due to the additional methane formed from CO_2.

Yuan et al. (Yuan et al., 2015) investigated Ni–Ca-catalyzed hydrogasification of a Chinese sub-bituminous coal in a fixed-bed reactor operated at 750 °C and 1 MPa, with an H_2 flow of 4.4 L·min^{-1}. They observed that product yields strongly depended on the amount of co-loaded calcium:

the 5 wt.% Ni–1 wt.% Ca catalyst produced the highest amounts of light aromatic hydrocarbons (2.15 wt.%, including 0.85 wt.% BTX and 0.7 wt.% naphthalene) and gaseous products (51.51 wt.% of CH_4, CO, CO_2 and C_2–C_3). Calcium addition inhibited nickel sintering, improved metal dispersion on the char, and limited catalyst poisoning by reacting with sulfur present in the coal.

Cobalt and nickel are widely recognized as highly effective catalysts for coal hydrogasification, but their high cost limits the practical feasibility of the process. This has motivated interest in more economical yet active alternatives, such as iron-based catalysts. Zhang et al. (F. Zhang et al., 2019) reported that a 5 wt.% Fe–1 wt.% Ca formulation delivered the best performance, achieving a CH_4 yield of 53.4%, compared with 7.76%, 11.58% and 12.20% for raw coal, 5 wt.% Fe, and 1 wt.% Ca, respectively. Although the methane formation rate followed the typical pattern observed for non-catalyzed char—rapid rise to a peak at 30 min followed by a gradual decline—it was substantially higher for the Fe–Ca system, showing a marked increase after 100 min and a second peak between 300 and 400 min, reaching 3.14 $mL\cdot(min\cdot g_{char})^{-1}$. These results indicate that co-loading Fe and Ca enhances char reactivity by improving metal dispersion, facilitating sulfur removal, and promoting both iron reduction and carburization.

Similar conclusions were reached by Yuan et al. (Yuan et al., 2017), who examined the promoter effect of calcium in Fe-catalyzed hydrogasification of sub-bituminous coal at 650–750 °C and 0.1–3.0 MPa in a fixed-bed reactor. At 750 °C and 1.0 MPa, the optimal Fe/Ca ratio (that is 5) maximized the production of light aromatic hydrocarbons (3.38 wt.%, including 2.47 wt.% BTX and 0.34 wt.% naphthalene) and increased gas yields from 33.15% to 46.71%. Calcium addition facilitated the reduction of iron oxide to metallic iron, enhanced metal dispersion, and ultimately improved the hydrogasification rate.

Copper and composite-based catalysts

Using composite catalysts is an effective way to improve catalytic efficiency while reducing costs. Copper-based materials are attractive for industrial use, but Cu alone is unsuitable for hydrogasification due to its poor ability to adsorb and dissociate hydrogen, its weak interaction with carbon, and its tendency to sinter at high temperatures (Bridier & Pérez-Ramírez, 2010; Sun et al., 2019). Cu–Ni alloys show good hydrogenation activity (Freitas et al., 2018; Gandarias et al., 2012; H. Liu et al., 2018), benefiting from improved metal dispersion (Han et al., 2019; Li et al., 2017; Z. Pan et al., 2018) and hydrogen spillover between Cu and Ni (Hu et al., 2018).

Sun et al. (Sun et al., 2019) evaluated Cu–Ni–Ca catalysts for hydrogasification of Yili sub-bituminous coal at 750 °C and 2 MPa. Catalysts prepared by incipient wetness impregnation showed CaS formation (indicating sulfur capture) and reduced sintering. Raman analysis confirmed

suppressed graphitization and more active sites due to strong metal–char interactions. The 2.5 wt.% Cu–2.5 wt.% Ni–1 wt.% Ca catalyst performed best, reaching 88.3% CH_4 yield and a methane formation rate of 11.56 mL· (min· g_{char})$^{-1}$ at 800 °C and 2 MPa. In a follow-up study, Sun et al. (Sun et al., 2021) showed that increasing Cu loading in Cu–Ca catalysts (1–5 wt.% Cu with 1 wt.% Ca) significantly enhanced methane yield and produced two distinct peaks in methane formation rate, while also shortening the induction period required for CaO to activate less reactive carbon.

Jiang et al. (Jiang et al., 2016) evaluated the performance of an inexpensive Cu-based catalyst in a pressurized fixed-bed reactor and demonstrated that copper can be efficiently recovered through selective oxidizing ammonia leaching, improving both its economic and environmental viability. The catalyst, prepared by incipient wetness impregnation of demineralized Yili coal char with Cu and Ca nitrates, was tested at 800 °C and 2 MPa under a hydrogen flow of 50 mL·min^{-1}. Under these conditions, the 5 wt.% Cu–1 wt.% Ca catalyst achieved a methane yield of 60.6%, markedly higher than at 700 °C or 750 °C, due to stronger Cu–C interactions and enhanced hydrogen-radical formation at high temperature. Increasing Cu loading from 1 wt.% to 5 wt.% raised methane yield from 36.8% to 60.6% and produced two peaks in methane formation rate, with a maximum of 6.65 mL· (min· g_{char})$^{-1}$ at 800 °C.

Alkaline and earth alkaline-based catalysts

Alkali catalysts such as K- and Na-based compounds, typically used at 5–10 wt.%, have been widely investigated for coal and char hydrogasification due to their high activity and strong selectivity toward CH_4—often exceeding that of transition metals (Karcz & Porada, 1996; Kokorotsikos et al., n.d.; Sheth et al., 2004; Zoheidi & Miller, n.d.). Their main limitation is the formation of water-insoluble species (e.g., $KAlSiO_4$) through reactions with mineral matter, which hinders catalyst recovery and increases operating costs (J. Zhang et al., 2015).

Hong et al. (B. Hong et al., 2013) examined KOH-based catalysts during hydrogasification of raw coal at 800 °C and 4 MPa. Using 10 wt.% catalyst added by wet-mixing, they observed CH_4 production rates up to 348 L·kg^{-1} in 60 min. Compared with pyrolysis, the presence of H_2 suppressed radical polycondensation and promoted rapid hydrogenation, leading to higher CH_4 release. Gas-productivity tests at 700–800 °C showed that, under H_2, productivity increased from 0.25 to 0.40 mol $_{C,produced}$· mol $_{C,feed}^{-1}$, while remaining nearly unchanged under pyrolysis. CH_4 yield rose from 13% to 30% between 700 and 800 °C, reflecting enhanced hydrogenation and hydrocracking at higher temperatures.

Liu et al. (X. Liu et al., 2017) investigated coal-char hydrogasification in a high-pressure fixed-bed reactor using CaO, $CaCO_3$, Na_2CO_3 and K_2CO_3 as

catalysts. Demineralized char (2 g) mixed with 10 wt.% catalyst was tested at 850 °C and 5 MPa H_2. As also reported in previous studies, $CaCO_3$ decomposed to CaO and CO_2 during hydrogasification, influencing reaction rate and carbon conversion. The resulting CaO inhibits the aromatic-ring condensation, although this effect is mainly exerted on the char surface on the char surface. At the same time, CaO also interacts with the volatile fraction: several authors have shown that it promotes the cleavage of methyl substituents on aromatic rings and accelerates the opening of structures such as BTX, PCX, indole, and benzofuran during coal-tar cracking under N_2 flow (Yongbin et al., 2004) Despite partial vaporization at high temperature, Na_2CO_3- and K_2CO_3-catalyzed chars showed much higher reactivity due to their uniform dispersion. Na_2CO_3 increased char reactivity to 53.13×10^{-5} s^{-1} (over ten times the uncatalyzed value), while K_2CO_3 achieved the highest reactivity, 70.42×10^{-5} s^{-1}. The catalytic activity followed the order K_2CO_3 >Na_2CO_3 > CaO > $CaCO_3$ > uncatalyzed char. The superior performance of Na and K catalysts was attributed to their ability to act both on the char surface and within its internal structure.

The authors concluded that the different catalytic activities of alkali and alkaline-earth catalysts arise from their mobility at high temperature. CaO remains essentially immobile, limiting its action to the char surface, whereas alkali metals can diffuse into the char matrix and interact uniformly with its internal structure. However, their high mobility also leads to partial vaporization at elevated temperatures, causing catalyst loss during hydrogasification.

II.3 Catalytic mechanism of iron group metal-based catalysts for the coal hydrogasification

In this paragraph, a detailed review of the reaction mechanism involved in the coal hydrogasification, when an iron group metal-based catalyst is employed, is presented.

The hydrogasification pathway over transition metals consists of hydrogen dissociation on the metallic surface, spillover of activated hydrogen atoms to carbonaceous sites, and the subsequent formation of C–H bonds through hydrogen–carbon interaction (S. Liu et al., 2024).

According to the majority of studies, transition metals act both as sites for C–C bond scission and as active centres for hydrogen adsorption and dissociation in CCHG (F. Zhang et al., 2019).

Hydrogen spillover is a well-known phenomenon in heterogeneous catalysis, in which atomic hydrogen migrates from one surface or particle to another (Conner & Falconer, 1995)(Xiong et al., 2021). Kenneth (Sancier, 1971) reported that Al_2O_3 enhances the catalytic performance of Pd/Al_2O_3 in benzene hydrogenation, suggesting that hydrogen atoms spill over from Pd to

the alumina surface, where they subsequently react with benzene. Similarly, Ohgoshi et al. (Ohgoshi et al., 1993) observed that neither Pt/KA nor NaY alone shows significant activity in isobutylene hydrogenation; however, combining the two catalysts markedly improves performance, indicating that hydrogen atoms are transferred from Pt/KA to NaY, enabling isobutylene reduction.

The recently proposed mechanism for CCHG indicates that both the catalyst–carbon interaction and the catalyst–hydrogen interaction play essential roles. However, Fe-group catalysts display markedly different activities, and their performance is strongly influenced by the hydrogen partial pressure. Moreover, different metals exert distinct effects on the cleavage of carbon–carbon (C–C) bonds. Liu et al. (S. Liu et al., 2024) investigated the reasons for the differences in catalytic hydrogasification activity of iron group metals. Experimental evidence shows that Fe–Ca exhibits the lowest hydrogasification activity among Fe-group catalysts. However, in the presence of spillover hydrogen, the catalytic performance of Fe increases markedly and even surpasses that of Ni. Furthermore, the CH_4 yield obtained with the Fe–Ca catalyst increases significantly when the H_2 partial pressure is raised from 2.0 to 3.0 MPa. This suggests that, for iron, the rate of hydrogen dissociation is slower than the rate of C–C bond cleavage, indicating that hydrogen activation is the rate-determining step in iron-catalyzed hydrogasification.

For the Co–Ca catalyst, only a modest promoting effect is observed. This behaviour may stem from the fact that cobalt exhibits a relatively balanced ability to dissociate hydrogen and cleave C–C bonds; therefore, simply enhancing its hydrogenation capacity results in only limited improvements in activity. A weaker promoting effect is also evident for Ni–Ca compared with Fe–Ca. Although nickel is generally an effective hydrogenation catalyst and can contribute to hydrogasification through hydrogen spillover, the overall Ni-catalyzed hydrogasification pathway is more complex.

(S. Liu et al., 2024) used the Mayer bond order of carbon-carbon and carbon-metal was used to assess the ability of metal to promote C-C bond cleavage. When H_2 molecules approach the metal sites, they first adsorb molecularly without breaking the H–H bond. The subsequent dissociation step requires overcoming an energy barrier of 54.81 kJ· mol^{-1} on Fe, 25.57 kJ· mol^{-1} on Ni, and 6.44 kJ· mol^{-1} on Co. These values indicate that hydrogen dissociation occurs more readily on Ni than on Fe, and even more easily on Co, which exhibits the lowest barrier. Overall, the hydrogen activation ability of iron-group metals follows the order Co > Ni > Fe. In the presence of spillover hydrogen, the hydrogen atoms markedly enhance the catalytic activity of iron. In contrast, the reactivity of nickel is limited by the slow rate of C–C bond cleavage, owing to its relatively weak ability to activate carbon. Cobalt, which combines the highest hydrogen-dissociation capacity with

strong carbon-activation ability, consequently exhibits superior hydrogasification performance.

Fe-group metals act as catalysts by promoting both hydrogen dissociation (eq. (17)) and carbon activation (eq.(18)), thereby facilitating the overall reaction.

$$H_2\ dissociation \xrightarrow{Co,Ni,Fe} 2H \quad (17)$$

$$C\ activation \xrightarrow{Co,Ni,Fe} C^{+}[metal\ carbide], C^{*}, C^{V}, C^{0} \quad (18)$$

where C^{v}, C^{*}, C^{0} represent carbon in volatiles (from catalytic depolymerization), activated carbon, and inert carbon, respectively.

Subsequently, carbon species *(C^{+}, C^{v} and C^{*})* react with activated hydrogen to form CH_4 (eq. (19)). In the presence of spillover hydrogen, hydrogen atoms can spill over onto the surface of carbon or metal carbides, thereby participating directly in the hydrogasification process (eq. (20-21)). Whether a catalyst is present or not, SH promotes hydrogasification because atomic hydrogen exhibits a stronger tendency to react with carbon. A possible reaction pathway in the presence of SH is illustrated in Figure II.3.

$$C^{*}, C^{V}, C^{0} \xrightarrow{H^{\cdot}} CH_x \xrightarrow{H^{\cdot}} CH_4 \quad (19)$$

$$H_2 \xrightarrow{Co/Al_2O_3} 2H^{SH}(spillover\ hydrogen) \quad (20)$$

$$C^{+}, C^{*}, C^{V} \xrightarrow{H^{SH}} CH_4 \quad (21)$$

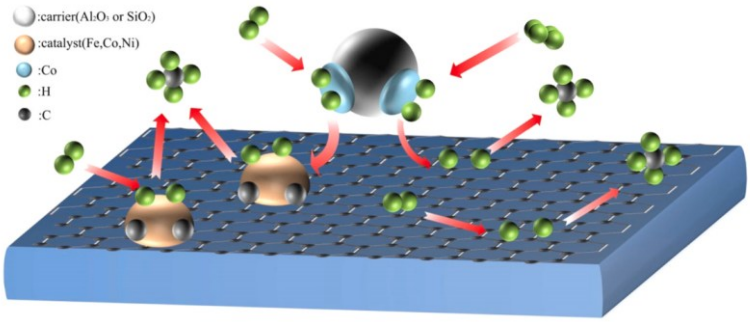


Figure II.3 *Schematic diagram of the reaction mechanism of SH on MC-hydrogasification catalyzed by an iron-group metal*

In the absence of SH, Fe is limited by slow hydrogen dissociation, Ni by sluggish C–C bond cleavage, and Co shows a balanced kinetic profile without a clear rate-limiting step. The introduction of SH profoundly enhances Fe activity by eliminating its slowest step, while Ni benefits moderately through increased availability of reactive hydrogen. For Co, already highly active, the promotional effect of SH is comparatively small. Overall, SH promotes catalytic hydrogasification across all Fe-group metals, though the magnitude

of the effect depends strongly on the intrinsic kinetic limitations of each catalyst (Table II.2).

Table II.2 *Summary of the rate-determining steps and the promotional effect of hydrogen spillover (SH) on Fe-, Ni-, and Co-based catalysts during hydrogasification*

Catalyst	Rate-determining step (without SH)[1]	Role of SH	Overall effect on hydrogasification activity
Fe (Fe-Ca)	H_2 dissociation is slower than C–C bond cleavage	Provides activated H atoms via spillover, effectively bypassing the slow step	Strong promotion; Fe activity increases dramatically in the presence of SH
Ni (Ni-Ca)	C–C bond cleavage (H_2 dissociation is relatively fast)	Supplies additional H_2, which reacts with C_V or C to form CH_4	Moderate promotion; SH enhances activity but does not remove the intrinsic rate limitation
Co (Co-Ca)	No dominant limitation: balanced H_2 dissociation and C–C activation	Adds extra H^*, but the catalyst is already efficient and carbon conversion is high	Weak promotion; SH has limited impact due to already optimal kinetics

Regarding the promotion effect of calcium additives, a detailed mechanistic analysis has shown that calcium nitrates and acetates, when impregnated onto carbonaceous substrates, react with carbon during heating under H_2 to form intermediate CaO(COO) species (Haga' And & Nishiyama, 1983). Above approximately 650 °C, these CaO(COO) intermediates decompose into CaO and CO_2, generating the two key species responsible for promoting the activity of Fe-, Co-, and Ni-based catalysts prepared from the corresponding nitrates or acetates. (Haga et al., 1992) further demonstrated that the CO_2 released in situ can be captured by adjacent Ni–C structures, forming Ni–(O)–C species that enhance Ni dispersion and increase the reactivity of carbon toward hydrogenation.

Overall, the use of Ca compounds in combination with Fe/Co/Ni nitrates or acetates effectively overcomes the intrinsic limitations of iron-group metals in the hydrogasification of carbonaceous materials. Calcium species provide three synergistic benefits: (1) they enhance the dispersion of Fe/Co/Ni on the carbon surface; (2) they mitigate catalyst poisoning and sintering; and (3) they modulate the metal–carbon interfacial chemistry, thereby enabling more efficient hydrogenation of low-reactivity carbon domains (graphitic or amorphous) (Yuan et al., 2017)(S. Yan et al., 2021).

II.4 Catalytic conversion of plastic waste

The literature reviewed above on catalytic hydrogasification primarily concerns coal and char conversion, as only a limited number of studies address plastic-waste hydrogasification.

Since the first step of the process is the pyrolysis of the plastic feedstock, it is relevant to understand the pyrolysis mechanism of the macromolecules which composing the plastic.

As reported by Xuan, W. et al. (Xuan et al., 2023) during the pyrolysis process the polymer dissociation happens up to the polymer monomer and then, the monomer converts to gas molecule. According to Hong, D. et al. (D. Hong et al., 2021) the PE dissociation begins with C-C bond breaking in a random position. The different C-C bond breaking results in some shorter chains. Then, after the initial C-C bond fracture of the polymer, a large number of monomers appears by the terminal dissociation. Finally, intramolecular and intermolecular dehydrogenation of the monomer occur, and gas molecules are generated, as showed in Figure II.4. The last step (monomer dehydrogenation) has the highest energy barrier.

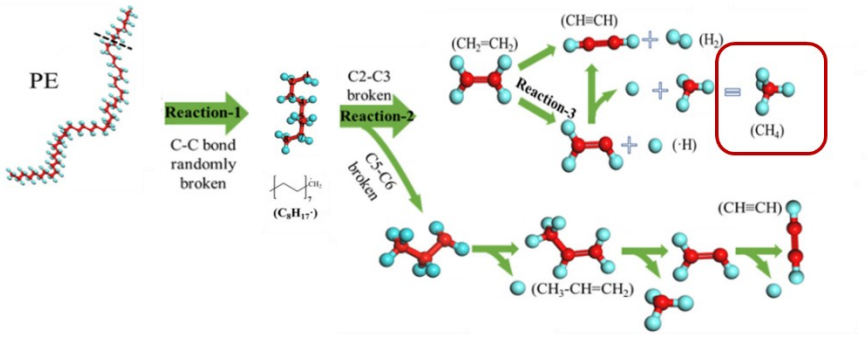


Figure II.4 *Pyrolysis mechanism and gas generation of PE (Reaction-1: the initial bond breaking reaction, Reaction-2: the terminal dissociation to monomer reaction, Reaction-3: the monomer dehydrogenation reaction) (Xuan et al., 2023)*

In general, C–C bonds in non-substituted aliphatic chains (C_{aliph}–C_{aliph}) have a high dissociation energy (~370 kJ mol^{-1}) and are rather inert, whereas in substituted aliphatic carbon chains such as in the case of glucose and PP, the bond dissociation energy can be lower than 300 kJ·mol^{-1}.

The cleavage of (C_{aliph}–C_{aliph}) bonds can be obtained using catalytic cracking over solid acid catalyst (for example zeolite), hydrogenolysis over a metal catalyst and hydrocracking over a metal-acid bifunctional catalyst. These strategies are well established in oil-refineries sector, where heavy petroleum feedstocks are converted into valuable shorter chain products (K. Lee et al., 2022). As for the conversion of biomass and plastic waste, there are different commercial-level processes such as Anellotech's Bio-TCat (woody biomass and waste plastics to benzene, toluene, xylenes and/or fuels), Shell's integrated hydropyrolysis and hydroconversion (IH2; non- food biomass and municipal wastes into hydrocarbons), Neste's NExBTL technology (vegetable oils to renewable diesel and aviation fuel), and Honeywell UOP's ecofining process (triglycerides to liquid fuels).

The use of a suitable catalyst can help to achieve the desired product distribution. For example, gasoline-range hydrocarbons and light olefins (C_2-

C_4) can be obtained by using a Brønsted acid catalyst (such as zeolite) at high temperatures. The reaction conditions and crystalline structure of the zeolite determine the product distribution: at high temperature the protolytic cracking is the dominant scission and produces light hydrocarbons (methane, ethane and ethylene); ultra stable Y zeolite (USY) is used in fluidized catalytic cracking for its superior liquid oil production activity and steam tolerance, while zeolite Socony Mobil-5 (ZSM-5) is able to produce light olefins and aromatics owing to its 10-membered ring micropore structure (K. Lee et al., 2022).

One different way to cleavage (Caliph–Caliph) bonds is the hydrogenolysis using metal catalysts to produce shorter linear hydrocarbons by terminal and consecutive scission of the polymer substrate. This approach for waste plastic has reached commercial plant operation scales (Tukker & Picard, 1999). Rorrer, J. E. et al. (Rorrer et al., 2021) have demonstrated the hydrogenolysis of polyethylene into liquid alkanes under mild conditions using ruthenium nanoparticles supported on carbon (Ru/C); this catalyst is highly active and selective for the hydrogenolysis of $C(sp^3)$–$C(sp^3)$ bonds at temperatures ranging from 200 to 250 °C producing ~40 wt.% of C_8–C_{45} and 50 wt.% of C_1–C_7 hydrocarbons, with CH_4 being the most abundant product. The cost of H_2 is the main issue, so the target of the conversion could be the production of more valuable longer-chain products, such as lubricant and wax products with uniform C-number distribution, which Celik, G. et al. (Celik et al., 2019) have produced with a 2 nm Pt-dispersed $SrTiO_3$ catalyst. Coupling hydrogenolysis (exothermic) with aromatization (endothermic), Zhang, F. et al. (F. Zhang et al., n.d.)were able to produce highly valuable long-alkyl-chain-functionalized aromatics using a common Pt/γ- Al2O3 catalyst at 280°C and no-external H_2 since the one produced via aromatization is sufficient to sustain the first hydrogenolysis step.

The hydrocracking approach consists in cracking the carbon chain using metal-acid bifunctional catalysts: the acid sites promote C–C cleavage, whereas the metal sites facilitate the paraffin–olefin transition in the initiation and termination steps. The scission involved is the β-scission since the temperatures are lower than that for catalytic cracking (200-300 °C), so the products are $\geq C_3$-hydrocarbons, in particular branched paraffins, because isomerization occurs before the β-scission. The metal component is usually Ni, NiMo-sulfide and CoMo-sulfide (which have high hydrogenation activity), or noble metals. Industrial processes Ecofinin and Honeywell UOP use hydrocracking to convert triglycerides into green diesel and jet fuel (K. Lee et al., 2022). For the plastic feedstocks, selective hydrocracking has been achieved using suitable catalysts: for example, Liu S. et al (S. Liu et al., 2021). converted PE using $Pt/WO_3/ZrO_2$-mixed USY catalysts system, where WO_3/ZrO_2 is the acidic support for Pt and breaks the polymer into C_{13+} hydrocarbons, which subsequently react on USY to produce gasoline-range hydrocarbons (C_5–C_{12}). Starting from PP, the same catalyst and reaction

conditions produce fewer products with shorter carbon chains and result in a higher isomer ratio than PE, showing that PP is a promising feedstock to be converted into transportation fuels (especially jet fuel and diesel).

Research on the hydrogasification of plastic waste into methane remains remarkably scarce, highlighting a clear gap in the current literature. Table II.4 reports the studies available in the literature for the specific process of plastic hydrogasification.Current state-of-the-art approaches rely on two-step tandem catalysis: plastics are first decomposed by pyrolysis at about 520 °C to produce short-chain fragments, which are then converted to methane in a separate vapor-phase step (Z. Zhang et al., 2023) (Zhao et al., 2024).

(Z. Zhang et al., 2023) performed the conversion of mixed plastic into methane with a selectivity >99% with a single-atom Ru catalyst in a two-reactor plant: in the primary reactor, the plastic (mixture of PE, PP and PET) is decomposed at 520°C into a short-chain polymer, which is then fed into the secondary reactor where the catalyst allows the conversion in methane in the presence of hydrogen at 1.5 bar and 300°C.

(Zhao et al., 2024) designed a high-efficiency catalyst codoping Mn heteroatoms into both RuO_2 and CeO_2, which allows them to gain an impressive PE conversion rate exceeding >99% with nearly 99% toward CH_4 at a moderate temperature of 250 °C within 8 h.

Searching for industrially relevant solutions, Lee et al. (W. T. Lee et al., 2021) investigated the performances of Ru-modified zeolite for the conversion of PE, PP and PS into grid-compatible methane at 300-350°C and 50 bar H_2. The experimental tests proved that methane with purity >97% can be achieved using hydrocracking treatment. Being a reductive process, it tends to result in fewer undesirable products.

Although remarkable results in terms of methane selectivity have been achieved in these studies, several research limitations still need to be addressed:

- The experimental scale remains confined to the conversion of small plastic samples (typically between 2.5 and 800 mg) using limited catalyst amounts (30–80 mg). Such a laboratory scale is far from the requirements of industrial applications, where tons of plastic waste must be processed.
- Most experiments have been conducted on mixtures of virgin polymers (PET, PP, PE, HIPS), which makes it difficult to extrapolate the results to real post-consumer plastic waste.
- Due to the small reactor volume, batch configurations have been predominantly employed.

Although effective, such multistage processes are complex and difficult to scale. This makes the development of a single-step, mild-condition route to CH_4 particularly appealing — and still largely unexplored.

In this context, the present doctoral project aims to overcome these limitations by developing a one-step hydrogasification process capable of converting larger quantities of real plastic waste into methane under mild conditions, while providing insights into catalyst behavior, reaction mechanisms, and scalability.

Table II.3 *Literature studies on Catalytic Hydrogasification*

Ref.	Catalyst	Reactor type	Reaction conditions	CH_4 yield and char conversion	CH_4 formation	Tar yield
(S. Yan et al., 2022)	Co-Ca/Co-K/ Co-Mg	Pressurized fluidized bed	12 L·min^{-1} of H_2 600-850 °C, 3.0 MPa U/U_{mf}: 1.9-15 Gas residence time: 1-8 s	X_{Char}: from 27 to 91.3 wt% Y_{CH4}: from 9.6 to 78.8 wt% in 30 min	72 mL·(min·g_{coal})$^{-1}$ after 10 min	Tar: 4.3 wt% HCL: 1.5 wt%
(Qu et al., 2022)	2wt%Fe/ Co/ Ni/K/Ca/Mg with 1 wt% Ca	Pressurized thermo-gravimetric analyser	200 mL·min^{-1}of H_2 850°C 3 MPa	X_{char}: 98% in 90 min		
(F. Zhang et al., 2019)	5wt%Fe - 1wt%Ca	Pressurized Fixed-bed reactor	50 L·min^{-1} of H_2 750°C, 2 MPa Reaction time: 450 min	Y_{CH4}: 53.40% (7.76 % without catalyst)	3.14 mL·(min·g_{char})$^{-1}$	
(Qu et al., 2019)	5wt%Co-1wt%Ca	Pressurized fluidized bed reactor	12.0 L·min^{-1} of H_2 850 °C, 3 MPa Reaction time: 100 min	Within 30 min: X_{char}: 90.0 wt% Y_{CH4}: 77.3 wt%	70.0 mL·(min·g_{coal})$^{-1}$ at 10 min	4.4 wt%
(S. Yan et al., 2018)	5wt%Co-1wt%Ca	Pressurized fluidized bed reactor	11.7 L (STP) ·min^{-1} of H_2 800 °C, 1 MPa Residence time: 30 min Reaction time: 100 min	X_{char} : 91.3 wt% Y_{CH4} : 77.3 wt% In 30 min	66.8 mL· (min·g_{coal})$^{-1}$	~8 wt%
(S. Yan et al., 2017)	5wt%Co-1wt%Ca	Pressurize fluidized bed	11.7 L(STP) ·min^{-1} 850 °C, 3 MPa U/U_{mf} 2	X_{Char}:91.3 wt%, Y_{CH4}:78.8 wt% Within 30 min	69.0 mL· (min·g_{coal})$^{-1}$ in 7.5 min 1.2 Nm^3_{CH4} · g_{coal}^{-1}	4.28 wt%
(Sun et al., 2021)	5wt%Cu-1wt%Ca catalyst	Pressurized fixed-bed reactor	50 L·min^{-1} of H_2 800°C, 2 MPa Reaction time: 450 min	Y_{CH4}: 61%	6.65 mL·(min·g_{char})$^{-1}$ after 100 min	

(Sun et al., 2019)	2.5%Cu-2.5%Ni-1.0%Ca	Pressurized fixed-bed reactor	50 mL·min^{-1} of H_2 800°C 2 MPa	Y_{CH4}: 88.3% in 450 min	11.56 mL·(min·g_{char})$^{-1}$ in 450 min	
(X. Liu et al., 2017)	10 wt% CaO/10 wt% $CaCO_3$/ 10 wt% Na_2CO_3/ 10 wt% K_2CO_3	High-pressure fixed-bed tube reactor	1.5 NL ·min^{-1} 850°C, 5 MPa Reaction time: 40 min	-No catalyst: X_{char}: 18.13 % -10 wt%CaO: X_{char}: 32.25% -10 wt%Na_2CO_3: X_{char}: 71.49% -10 wt%K_2CO_3: X_{char}~80%		
(Jiang et al., 2017)	CaO-0.258FeS_2	Pressurized fixed-bed reactor	50 mL·min^{-1} 800°C, 3.0 MPa	Y_{CH4}: 77.9 wt% in 7.5 h.	Max of 1.75 mL·(min·g_{char})$^{-1}$ after 200 min	
(Skodras et al., 2016)	20 wt% K_2CO_3	Tubular fixed bed reactor	850°C, 1 MPa, Residence times up to 100 min	X_{char}: 40%	2 mL· (g· min)$^{-1}$	
(B. Hong et al., 2013)	10wt% K_2CO_3/ 10wt% $Ca(OH)_2$/ 10wt% Ni $(NO_3)_2$	Pressurized fixed-bed reactor	1 L·min^{-1} of H_2 800°C, 4.0 MPa	Y_{CH4} within 60 min: -Raw caol/ $Ca(OH)_2$/ $Ni(NO_3)_2$/Na_2CO_3/KOH/: 29.3 %, 29%, 33.0%, 67.1%, 78%	With KOH catalyst: 0.348 L·g_{coal} in 60 min	With KOH catalyst: 7%

Table II.4 *Literature studies on the catalytic hydrogasification of plastics*

. Ref.	Catalyst	Reactor type	Reaction conditions	CH_4 selectivity and plastic conversion	Comments
(Z. Zhang et al., 2023)	Single atom Ru on Co/Al oxide	Two fixed-bed reactors (pyrolysis+methanation)	520°C for pyrolysis step 300°C for methanation step 1.5 bar, 30 mg of catalyst, 2.5 mg of plastic GHSV: 22.8 s^{-1}	CH_4 selectivity: 99% Plastic conversion: 90%	Single atoms is the key to efficient conversion to produce single product methane and reduce carbon formation
(Zhao et al., 2024)	$RuMn/CeO_2$	Batch reactor	250°C 10 bar of H_2 0.8 g of LDPE and 0.08 g of catalyst	CH_4 selectivity: 99 Plastic conversion: 99%	Ru^0-$Ru^{\delta+}$ interface enhances the adsorption of alkane intermediates
(W. T. Lee et al., 2021)	RuZ (2.5 wt% Ru)	Autoclave reactor	300°C, 50 bar H_2, 500 rpm 1.7 g of PE or PP and 0.103 mg of RuZ 0.780 g of PS and 0.052 g of RuZ	Methane selectivity>97%	

II.5 Type of reactor configuration for plastic waste pyrolysis

The choice of reactor plays a crucial role in tuning the product distribution in the pyrolysis of plastic waste (Qureshi et al., 2020a). Current investigations into plastic conversion reactor design are predominantly carried out at laboratory and pilot stages, considering the heat and mass transfer, continuous operation, reduced residence time, high process flexibility, catalytic capability, and scalability (Qureshi et al., 2020b).

Studies on the comparison of pyrolysis liquid from fixed-bed and batch reactor using different plastics (polystyrene (PS), polyethylene (PE), polypropylene (PP), and polyethylene terephthalate (PET)) were conducted by Miandad et al. (Miandad et al., 2017). An attempt to examine the energy conversion efficiency of pyrolysis of rice straw at 500°C was performed by Nam et al. (Nam et al., 2015) in three different reactors: bench-scale auger reactor, batch reactor, and fluidized bed reactor. The majority of the energy (50–64%) was in the bio-char products from the auger and batch reactors, while the bio-oil from the fluidized bed reactor contained the highest energy (47%). Choi et al. (Choi et al., 2024) pyrolyzed three different plastics (PP, LDPE and ABS) in a fluidized bed reactor. Comparison with fixed-bed reactor configuration highlighted the possibility to achieve higher C_1-C_2 gas yield (CH_4 and C_2H_4) and lower C_{3+} gas in the fluidized-bed reactor.

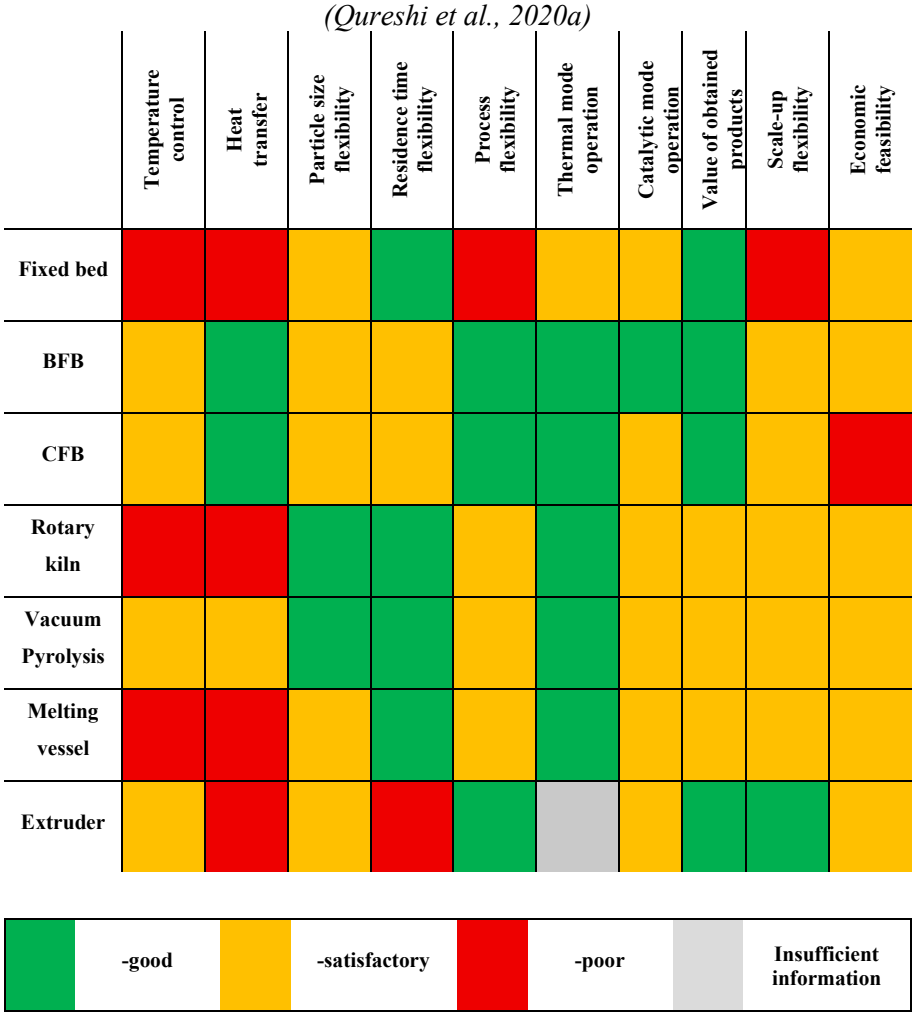
Heat transfer efficiency was found to be the key factor in the pyrolysis of plastic waste. The reactor comparison for plastic thermolysis process is shown in Table II.5, based on different operational and economical flexibility parameters.

The majority of industrial-scale reactors for plastic waste pyrolysis are rotary kilns (Zhang et al., 2022, 2020). Since rotary kilns have a low heat transfer, it is necessary to load more heat carriers to improve heat efficiency, weighing on cost and energy consumption.

In fluidized bed reactors (BFB and CFB), operating parameters—particularly temperature—can be controlled with considerable flexibility, thereby allowing precise tuning of product distribution (Scheirs & Kaminsky, 2006). Their superiority derives from their excellent heat and mass transfer achieved by a heated fluidizing medium in the reactor; moreover, they can also be used with catalysts to yields selective product distribution at lower temperatures. Although their scalability is generally achievable, the investment costs remain high, particularly at small scale (Qureshi et al., 2020a). Vacuum pyrolysis safeguards the monomers produced from repolymerization. However, such reactors are generally heated externally, resulting in poor heat transfer, and their operation can be expensive owing to the stringent pressure conditions. Same drawback related to the heat transfer can be pointed out for melting vessels or stirred-tank reactors.

Considering these aspects, the investigation of a fluidized bed reactor setup warrants attention.

Table II.5. *Reactor comparison for plastic thermolysis. Modified from (Qureshi et al., 2020a)*



II.6 Fluidization of plastic particles

Fluidization is a well-established engineering technique that transforms a bed of solid particles into a liquid-like state by introducing a gas, liquid, or a mixture of both through a distributor. This enhanced mixing significantly improves heat and mass transfer, as well as chemical reaction rates between the particles and the fluid. Consequently, fluidization is widely used in industrial processes, including the catalytic cracking of petroleum feedstock (Paudel & Feng, 2013). Fluidized-bed reactors offer several key advantages for the thermal treatment of waste (Scheirs & Kaminsky, 2006):

- Excellent mixing and isothermal conditions: The rapid and thorough mixing of solids ensures nearly uniform temperatures throughout the bed, simplifying and enhancing process control.
- Thermal stability: The well-mixed solid inventory acts as a large thermal flywheel, effectively resisting rapid temperature fluctuations and preventing the formation of hot or cold spots.
- Lower operating temperatures: These reactors generally operate at lower temperatures compared to other gas-solid reactor types.
- Enhanced heat and mass transfer: Fluidized beds provide superior gas-particle heat and mass transfer rates and excellent contact between gaseous and solid reactants.
- Continuous and manageable operation: The fluid-like behavior of particles allows for continuous, controlled processes with ease of material handling. Solids circulation between multiple fluidized beds facilitates efficient heat management and the replacement of problematic bed material.
- High process flexibility: Fluidized beds can accommodate various fluidizing agents, operating temperatures, gas residence times, and can be used with or without a catalyst.
- Reduced maintenance: The absence of moving parts in high-temperature zones and lower operating temperatures contribute to lower maintenance times and costs, making them a viable option for both large and small-scale applications.

However, disadvantages could be pointed out, concerning the entrainment of solid particles by the gas with the necessity of making up for fresh material, and the segregation due to agglomeration of sticky particles, which could require modification in operating conditions and the variation in process performances (Scheirs & Kaminsky, 2006). The steps that can lead to segregation and defluidization phenomena are reported in Figure II.5 (Mastellone & Arena, 2004), in the case of a plastic feedstock with inert sand particles used to promote fluidization. The nature of the polymer, and more precisely the presence or not of a sticky carbon residue, determines the crumbling of the aggregates (as in the case of PE), or the adhesion of several layers of inert material on plastic particles (as in the case of PET) (Arena & Mastellone, 2000). Besides the nature of the polymer, the other two parameters influencing the defluidization time (defined as the time when the whole particle bed leaves the fluidization regime and assumes fixed bed properties) were identified in: i) the ratio $W_{bed}/ Q_{polymer}$ between the bed hold-up and the polymer feed rate; ii) the bed temperature. The general criterion for preserving fluidization quality is the continuous feeding of fresh inert material (for example, sand) with the simultaneous drawing of bed material, regardless of the nature of the plastic (Arena & Mastellone, 2000).

Geldart (Geldart, 1973) noted that the behavior of a fluidized bed is influenced by factors such as particle density, the properties of the fluidizing agent, and the size of the solid particles. Biomass and plastic waste are difficult to fluidize due to their irregular shape, large size and low density. To improve the fluidization, a second fluidization medium is added to the bed, typically an inert material (silica sand, aluminium oxide, CFB cinder) or also the catalyst. These actions prevent the formation of preferential channels and multiple stagnation points, both of which hinder the fluidization process (Balestieri et al., 2023). The ratio between the inert material and bed material is a parameter to optimize for each particular case. Balestieri et al. (Balestieri et al., 2023) reported that an increase in the ratio of rice husks negatively affected fluidization, especially considering values above 5 and the generation of several preferential paths and bed stoppages.

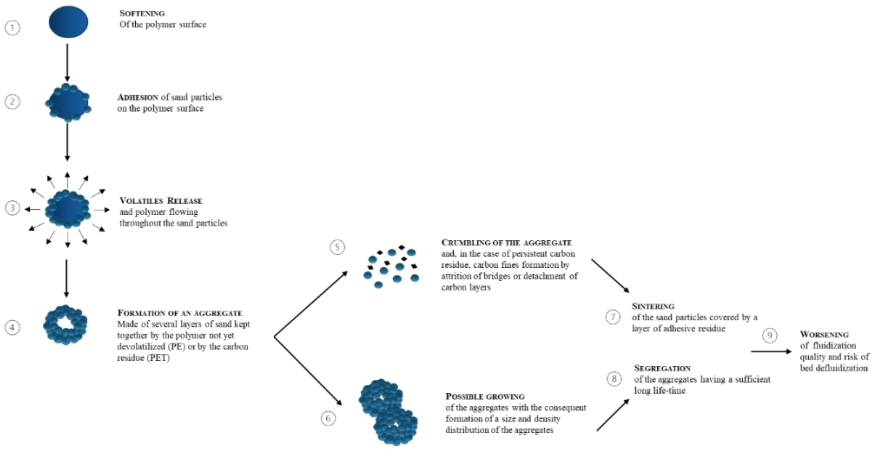


Figure II.5 *Steps that lead to segregation and fluidization when plastic feedstock is pyrolyzed in a fluidized bed reactor (Mastellone & Arena, 2004)*

Therefore, understanding the hydrodynamic characteristics of mixtures of biomass and inert particles is crucial for the optimal design and operation of fluidized bed reactors or devices (Paudel & Feng, 2013).

The minimum fluidization velocity U_{mf} is a key parameter in this context. It defines the lower limit of the flow rate required for the suspension of a solid in the gaseous phase and is essential for modelling fluidized bed processes.

Numerous studies have been carried out to determine the minimum fluidization velocities for biomass particles. Experiments on sawdust, coal bottom ash, coconut shell, rice husk, and palm fiber of different sizes and density were conducted by Abdullah et al. (Abdullah et al., 2003) who concluded that only Geldart type B biomass satisfactorily fluidized, having voidage and bulk density as parameters influencing the fluidization. Mixtures of biomass and sand were the focus of the investigation of Si and Guo (Si &

Guo, 2008) who studied the effect of mass percentage of biomass (20%, 30%, 40% and 50%) on the minimum fluidization velocity, which increases with the biomass content. They also found that a drop in the minimum fluidization velocity could be reached with increasing sound pressure level and had a minimum value over the sound frequency range of 100-200 Hz. Indeed, increasing vibration frequency results in a rise in the pressure drop and reduction of minimum fluidization velocities, since homogenous fluidization can be reached.

II.6.1 Phenomenology of fluidization of binary mixtures

Considering a mixture of solids that differ both in density and size, a dynamic equilibrium between mixing and segregation conditions determines different patterns of fluidization (Formisani et al., 2013).

When the less dense component is also the smaller, "top fluidization" happens throughout the mechanism sketched in Figure II.6. The fluidization front, generated at the initial velocity U_{if} at the upper surface of the bed (Figure II.6a), travels downward as the gas velocity is increased. Rowe et al. (Rowe et al., 1964) have defined as "flotsam" component the lighter and smaller particles, which convene on the top of the bed forming a bubbling layer; while the "jetsam" is the denser component and stays in a fixed stratum. Above the initial velocity, the height of the initial homogeneous mixture, resting at the bottom of the column—still in a non-fluidized state—gradually decreases (Figure II.6b).

When the velocity reaches the final fluidization velocity U_{ff}, the entire bed becomes suspended, and the final pressure drop plateau is attained. At this stage, the two solids exhibit a mixing degree greater than that observed at lower velocities (Figure II.6c), although this depends on the specific mixture and its composition. Nonetheless, a distinct top layer composed almost entirely of flotsam is consistently observed across all cases.

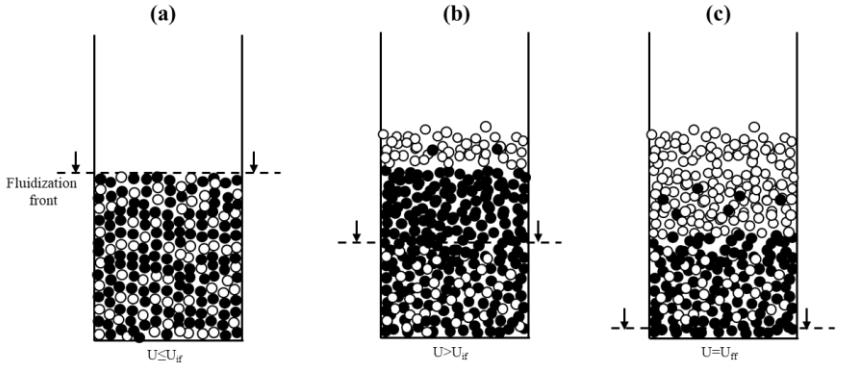


Figure II.6 *Binary fluidization pattern: top fluidization.(Formisani et al., 2008)*

In contrast, binary systems in which the denser component is also the smaller one can exhibit multiple fluidization patterns. When the denser solid fluidizes first—typically occurring when its particle size is significantly smaller than that of the other component—the fluidization front originates at the bottom of the bed, effectively inverting the conventional behavior. This phenomenon is commonly referred to as "bottom fluidization." As the superficial gas velocity reaches the initial velocity U_{if} of the mixture, the entire bed is momentarily lifted, creating a narrow horizontal gap between the bed and the gas distributor. The particles with the lower minimum fluidization velocity (i.e., the "fluidized" component) then descend, forming a bubbling layer at the base of the column (Figure II.7b), while the other component accumulates as a fixed layer above the original mixture, which remains sandwiched between the two segregated phases.

Further increases in gas velocity promote the expansion of these segregated layers at the expense of the mixed region, until at the final fluidization velocity U_{ff} and beyond, the entire bed becomes suspended and the two solids re-mix to a certain extent (Figure II.7c). Figure II.8 schematizes the three layers distinguishable when U varies from U_{if} and U_{ff}, in the two types of fluidization.

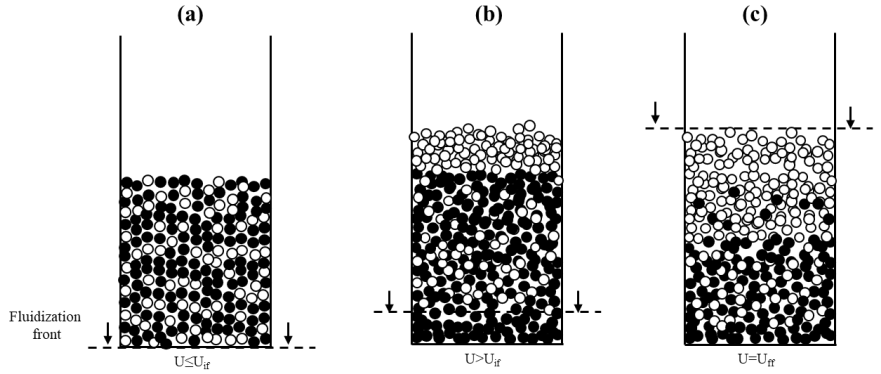


Figure II.7 *Binary fluidization pattern: bottom fluidization (Formisani et al., 2013)*

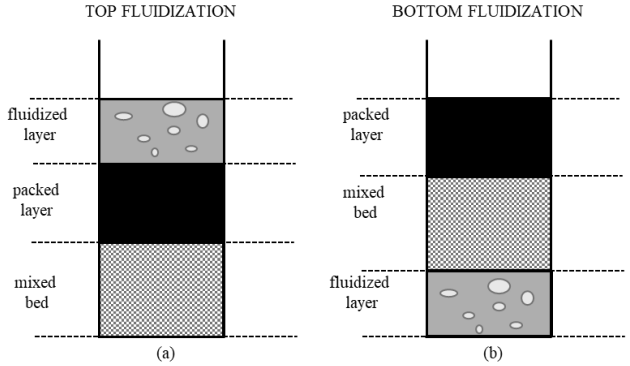


Figure II.8 *Three layers structures of mixtures of dissimilar solids (Formisani et al., 2013)*

II.6.2 Minimum fluidization velocity estimation

The minimum fluidization velocity (U_{mf}) is defined as the gas velocity at which a solid passes from a fixed to a fluidized state. The U_{mf} is generally measured by the bed pressure drop against the superficial gas velocity curve method (Chiba et al., 1979). Its estimation is crucial to correctly design the reactor. Correlations for different kinds of particles are reported in Table II.6.

Theoretical analysis

For a fixed bed, pressure drop is defined as eq. (22):

$$\Delta P_l = W/A_c = const \tag{22}$$

Where W is the weight of bed material and A_c is the cross-sectional area of the reactor.

The pressure drop of a fixed bed with height H with porosity ε, for non-spherical particles (ϕ) with an average diameter d_p, is given by Ergun as eq. (23):

$$\frac{\Delta P_l}{H} = \frac{150(1-\varepsilon)^2}{\varepsilon^3} \cdot \frac{\mu_f U}{(\phi d_p)^2} + \frac{1.75(1-\varepsilon)}{\varepsilon^3} \cdot \frac{\rho_f U^2}{\phi d_p} \tag{23}$$

where ρ_f and μ_f are the density and viscosity of the fluid.

On the right-hand side, the first term represents the pressure loss through viscous effects, which is dominant in the laminar flow region (Re<20); while the second term represents the pressure loss due to inertial forces and is dominant at high Reynolds numbers (Re>1000) (R. Feng et al., 2017).

At the minimum fluidization conditions, the pressure drop is equal to the pressure drop expressed as the difference between the flotation and the net weight of the solid per unit of surface (eq. (24)) (Renda et al., 2025):

$$\Delta P_l = H_{mf}(1-\varepsilon_{mf})(\rho_p - \rho_f)g \tag{24}$$

where the "*mf*" subscript indicates the parameter in the minimum fluidization condition. Combining the last two equations (where eq. (23) is considered at the *mf* conditions) and rearranging them, a new correlation can be obtained (eq. (25)), expressed in terms of dimensionless quantities, known as Archimedes number (*Ar*) (eq. (26) and Reynolds number (Re_{mf}) (eq. (27)):

$$Ar = \frac{150(1-\varepsilon_{mf})}{\phi^2 \varepsilon_{mf}^3} \cdot Re_{mf} + \frac{1.75}{\phi \varepsilon_{mf}^3} \cdot Re_{mf}^2 \tag{25}$$

Where:

$$Ar = \frac{d_p^3 \rho_f (\rho_p - \rho_f) g}{\mu_f^2} \tag{26}$$

$$Re = \frac{d_p U_{mf} \rho_f}{\mu_f} \tag{27}$$

Rearranging eq. (25), it is possible to obtain the correlation eq. (28):

$$Re_{mf} = \left[\left(42.857 \frac{k_2}{k_1} \right)^2 + \frac{Ar}{1.75 k_1} \right]^{0.5} - 42.857 \frac{k_2}{k_1} \tag{28}$$

Where $k_1 = \frac{1}{\phi \varepsilon_{mf}^3}$ and $k_2 = \frac{(1-\varepsilon_{mf})}{\phi^2 \varepsilon_{mf}^3}$

This equation implies the knowledge of sphericity and porosity of minimum fluidization parameters, which are difficult to determine experimentally.

A simplified form for this equation was proposed by Wen et Yu (Wen & Yu, 1953), introducing two constant K_1 and K_2, as follows (eq. (29)):

$$Re_{mf} = \left[{K_1}^2 + K_2 Ar \right]^{0.5} - K_1 \tag{29}$$

Their values stay nearly constant for different kinds of particles over a wide range of Reynolds numbers (*Re* from 0.001 to 4000) at minimum fluidization conditions.

Table II.6 *Values of the two parameters in the correlation for the estimation of U_{mf}*

Reference	K_1	K_2	Materials	PSD	Pressure	Other conditions
(Wen & Yu, 1953)	33.7	0.00408	Fine particles, at atmospheric pressure	Narrow	Ambient	$10^{-3}<Re_{mf}<4\times10^{3}$
(Babu et al., 1978)	25.3	0.0651	Fuel particles for the coal conversion systems			
(Grace, 1982)	27.2	0.0408				
(Chitester et al., 1984)	28.7	0.0494	Coal, char, and ballotini	Narrow	Elevated pressure	$10^{2}<Ar<10^{6}$
(Richardson)	25.7	0.0365				
(Saxena and Vogel)	25.3	0.0571	Dolomite	Narrow	Elevated pressure	$6<Re_{mf}<10^{2}$
(Nakamura et al., 1985)	33.9	0.0465	Glass beads	Narrow	Ambient	
(Zhu et al.)	22.1	0.0354	Sand bead	Narrow	Elevated pressure	$40<Re_{mf}<10^{3}$
(Paudel & Feng, 2013)	30.28	0.046	Sand, glass, bead and alumina			
(Paudel & Feng, 2013)	30.28	0.108	Corn cobs and walnut shells			
(R. Feng et al., 2017)	27.9	0.0554	Polystyrene particles, of different diameters (0.55 mm, 0.70 mm, 0.90 mm, 1.13 mm, and 1.34 mm	Narrow		
(Reina et al., 2000)	48	0.045	Different type of woods			
(Kozanoglu et al., 2002)	$\Phi>0.8$ 36.8 $0.5<\Phi\leq0.8$ 33.6 Both types 30.3	$\Phi>0.8$ 0.065 $0.5<\Phi\leq0.8$ 0.0598 Both types 0.0546	Black pepper, millet, munition paste, corn, turf seeds, and others			
(Pérez et al., 2018)	$U_{mf}=\frac{0.0822Ar^{0.4304}\mu_f}{d_p\rho_f}$ $U_{mf}=\frac{0.1045Ar^{0.4998}\mu_f}{d_p\rho_f}$		Sugarcane bagasse			$0.21<Re_{mf}<2$ $8.37<Ar<1502$ $0.32<Re_{mf}<4.44$ $8.37<Ar<1502$

II.6.3 Estimation of minimum fluidization velocity for binary mixture

The correlation between the minimum fluidization velocity and the Reynolds and Archimedes numbers means that the parameters that influence the fluidization of inert particles are essentially the size and density. The shape effect is negligible since the inert particles usually have round shapes. This is not true when biomass fluidization is performed: its complex geometry and physical properties (lower sphericity - between 0.1 and 0.5) could determine significant differences with respect to the inert particles. Paudel and Feng (Paudel & Feng, 2013) proposed a correlation using different experimental data on corn cobs and walnut shells, resulting in an efficient fitting for binary mixtures of biomass and sand particles.

Two approaches are generally used for the estimation of the minimum fluidization velocity of binary systems:

1) A first method assumes the binary mixture as a mono-component system, imposing an equivalent particle diameter and density (Paudel & Feng, 2013) to be used into the generalized Ergun-type equations. This approach can lack in the representation of reality since some fluidization could only partially happen at the incipient fluidization state and particle size ratio and size distribution of the solids composing the mixture can influence the bed voidage of the binary system.
2) A second approach uses empirical correlations developed directly from experimental data in particular conditions, gaining more accuracy and simplicity in utilization. Table II.7 reports some of the formulas proposed in the literature, with the range of application.

Among the correlations, the one proposed by Goosens et al (1971) ignores the variation of bed voidage in binary systems, which can become significant for large particle size ratio. Otero and Corella, Cheung et al., Chiba et al., and Obata et al. developed empirical equations based on the knowledge of the minimum fluidization velocity of each particle component in the binary system; their general validity beyond the particular application has to be verified.

The minimum fluidization velocity (U_{mf}) of various binary mixtures is effectively predicted by the correlation proposed by Cheung et al. Their model suggests that, for systems containing a low fraction of light/small (or heavy/large) particles, the U_{mf} of the mixture closely approximates that of the heavy/large (or light/small) component. However, the applicability of this correlation is limited: it assumes a particle size ratio not exceeding 3, and the exponent value of 2 was derived from a narrow experimental dataset, potentially restricting its generalizability. Modifications to the correlation could involve the bed voidage effect, using the general exponent *n*, mainly

affected by the ratio of particle and increasing with particle size ratio (Fu et al., 2019).

The method applied to binary particle systems is shown in Figure II.9. For binary mixtures, and in particular with wide particle size distribution (PSD), other two velocities can be defined besides the minimum fluidization velocity, which are the incipient and total fluidization velocities (U_{if} and U_{tf}). The incipient fluidization corresponds to the breakpoint in the ΔP versus U_f curve when the first particles begin to fluidize, while the total fluidization happens when all particles are fluidized (R. Feng et al., 2017). The PSD influences the fluidization quality of the mixture. Gauthier et al.(Gauthier et al., 1999) and Lin et al. (Lin et al., 2002) indicated that the particles of flat and binary distributions tend to move segregation, but the particles of Gaussian-type PSD which is similar to the narrow PSD tend to be good mixing.

The parameters necessary to estimate the minimum fluidization velocity of binary mixture of solids particles are the surface/volume average particle diameter (eq. (31)) and density (eq. (30)), defined as (Asif, 2011; Formisani et al., 2013):

$$\frac{1}{\bar{\rho}} = \frac{x_B}{\rho_B} + \frac{x_S}{\rho_S} \tag{30}$$

$$\bar{d} = d_B d_S \left[\frac{x_B \rho_S + x_S \rho_B}{x_B \rho_S d_S + x_S \rho_B d_B}\right] \tag{31}$$

where x_i is the weight fraction of each component of solid particles, the subscripts, S and B, are used to distinguish the particle components with lower and higher minimum fluidization velocities, respectively. From the weight fraction is also possible to calculate the volume fraction of each component of the solid mixture (Formisani et al., 2013), which affect the U_{mf}.

Starting from the definitions of effective particle diameter and density, Archimedes number (eq. (32)) and Reynolds number (eq. (33)) of a binary mixture are given by:

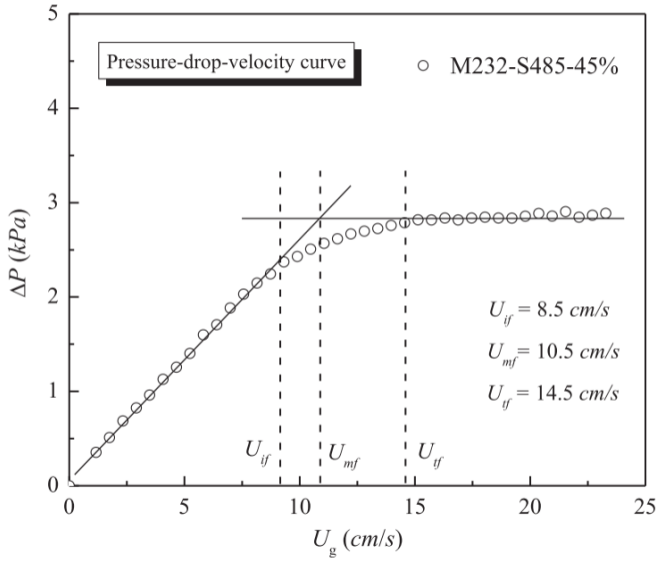


Figure II.9 *A typical pressure-drop-velocity curve of a binary mixture. (Fu et al., 2019)*

$$\overline{Ar} = \rho_f(\overline{\rho_p} - \rho_f)g\overline{d_p^3}/\mu^2 \quad (32)$$

$$\overline{Re}_{mf} = \rho_f U_{mf}\bar{d}/\mu \quad (33)$$

Starting from this point (Paudel & Feng, 2013) proposed a correlation which takes into account the biomass weight percentage (reported in Table II.7), which becomes the relative equation for inert particles when $x_B=0$, while for $x_B=1$ is the correlation for biomass particles. This effectively predicted the corn cob data in Paudel and Feng. Several investigations have been carried out on the study of fluidization of binary mixtures. Table II.8 reports a summary of the details of experiments, which involved systems of particles differing in size and density, with minimum fluidization velocity varying in the range 0.1-145 cm·s^{-1}.

Table II.7 *List of correlations for binary systems*

Reference	Correlation	Notes
Goossens et al. (1971)	$U_{mf} = 0.00061\overline{Ar} \times \mu/(\rho_f \bar{d})$	
Otero and Corella (1971)	$U_{mf} = [x_B U_B + (1 - x_B)U_S]$	x_B is the volumetric fraction of larger component arithmetic average of U_{mf} of single component solids differing only in size (0.3≤ds/db<3)
(Cheung L; Nienow A.W, Rowe P.N., 1973)	$\frac{U_{mf}}{U_S} = \left(\frac{U_B}{U_S}\right)^{x_B^2}$	The exponent 2 by fitting limited experimental data U_B: is the min fluidization velocity of larger particles U_S: the min fluidization velocity of smaller particles
(Fu et al., 2019)	$\frac{U_{mf}}{U_S} = \left(\frac{U_B}{U_S}\right)^{x_B^n}$	$n = 1.26 \times (d_B/d_S)^{0.5}$
(Chiba et al., 1979)	$\frac{U_{mf}}{U_S} = \left(\frac{\bar{\rho}}{\rho_S}\right)\left(\frac{\bar{d}}{d_S}\right)^2$	Binary mixture (skillful and complex derivation) Without the knowledge of U_B
(EIJI OBATA, HARU OWATANABE AND NAOTO SHIENDO, 1982)	Simple graphical method	Binary mixture harmonic averaging of the minimum fluidization velocity of wide PSD
(Rincon et al., 1994)	$\frac{1}{U_M} = \frac{1}{U_{12\ldots n}} = \sum_{i=n}^{n} \frac{x_i}{U_i}$	Perfectly mixed and completely segregated multicomponent mixture
(Asif, 2011)	$1.75\bar{\varepsilon}_{mf}^3 \overline{Re}_{mf}^2 + 150\bar{\varepsilon}_{mf}^3(1 - \varepsilon_{mf})\overline{Re}_{mf} - Ar =$	Binary mixture
Rowe and Nienow	$U_{mf,mix} = U_{mf,1} f(\varepsilon)\left[x_1 + \left(\frac{U_{mf,1}}{U_{mf,2}}\right)^{n/(3-n)} \cdot x_2 + \cdots\right]^{(1-3/n)}$	semi-theoretical equation by extending Hatch's pressure-drop relationship particles with various sizes should have same shape and density n can be taken to be 1.053 f (ε) is function of the bed voidage
(Paudel & Feng, 2013)	$Re_{mf} = \left\{30.28^2 + \left[0.046(1 - x_B) + 0.108x_B^{1/2}\right]Ar\right\}^{1/2} - 30.28$	Weight fraction of biomass 10-90%
(R. Rao & Ram. Bheemarasetti, 2001)	$U_{mf,mix} = \frac{d_{p\,eff}^2(\rho_{eff} - \rho_f)g}{1650\mu}$ $d_{p\,eff}^2 = (20d_{p1} + 0.36)\left\{d_{p1}\left[\left(\frac{\rho_1}{\rho_2}\right)\left(\frac{d_{p2}}{d_{p1}}\right)\right]^{x_2/x_1}\right\}^2$	Biomass and sand up to 10% weight of biomass particles in mixtures

Table II.8 *Literature summary of minimum fluidization velocity of binary mixtures. Rearranged by (Fu et al., 2019)*

Ref.	Bed cross-section (cm)	Material	ρ_f (kg/m^3)	d_p (µm)	U_{mf} (cm/s)	Range of Ar	Range of Re_{mf}
(Lockett & Gunnarsson, 1973)	3.5	FCC	1150	45-95	0.23-0.27	4.4-25.4	0.007-0.019
Cheung L. ; Nienow A.W. ; Rowe P.N. (1973)	14	Glass powder Bronze ballotini	2520 8540 2520	195-461 388-550 271-642	2.5-15 39-51 8-36.5	737-9736 19678-56052 1978-26296	0.35-4.98 10.9-20.2 1.56-16.89
Rowe and Nienow (1975)	-	catalyst	1150	29-81	0.1-0.5	1.1-24.3	0.002-0.029
Chen and Keairns (1975)	10	Dolomite Char	2800 702	338-1125 718	11.5-78 38	4283-157436 10,233	2.8-63.3 7.76
(Chiba et al., 1979)	5	Copper shot Glass bead Hollow char Silica ballons	8900 2520 1080 190	153-254 115-385 775 359	9.2-18.2 1.6-14.4 22.5 0.79	1520-5754 151-5671 19,811 344.5	1.08-3.33 0.13-3.99 12.57 0.21
Noda et al. 1986	16	Glass bead Sand Rubber Soya bean	2520 2600 1450 1220	45.4-84.3 45.4-139 283 785	13.9-45 16.9-76 114 145	9.3-59.5 9.6-275.4 1296 23,261	0.45-2.73 0.55-7.61 23.25 82.03
(Formisani, 1991)	10.1	Glass bead	2530	153-483	2.4-21.2	357-11242	0.24-6.8
Marzocchella et al. 2000	12	Silica sand Glass bead	2600 2540	125 500	1.7 22	200 12,521	0.15 7.92
(Olivieri et al., 2004)	12	Silica sand Silica gel Polypropylene Glass bead	2600 600 900 2540	125-500 375 500 500	2.2-19 3.2 11 23	200-12817 1246 4432 12,521	0.2 0.87 3.96 8.29
(Formisani et al., 2008)	10	Glass bead Molecular sieves Steel shots Ceramic spheres	2480 1460 7600 3760	154-612 624-800 243-439 701	2.5-32.5 21.5-35.5 17.5-46 44	357-22418 13984-29468 25,366 51,086	0.28-14.33 9.67-20.57 14.55 22.23
(Asif, 2011)	6	Sand Plastic particles	2664 1761	550 2550	3.6 26.5	17,479 1,151, 254	1.43 48.7

(Formisani et al., 2011)	10	Glass bead Ceramic spheres Steel shots	2480 3760 7600	172-593 605 243	2.8-30.8 43.3 17.3	357-34571 32, 841 4302-25366	0.24-14.78 18.88 3.03-15.09
(Paudel & Feng, 2013)	14.5	Sand Walnut sheel	2630 1200	241 856	7.4 55.3	1448 29,655	1.28 34.11
Kumoro et al., 2014	10	River sand Corn cob	2630 1080	241 1040	9 62	1452-4142 47,876	1.56-4.54 46.47

Despite the extensive body of literature on catalytic hydrogasification and fluidized-bed technologies, very limited attention has been devoted to the hydrodynamic behaviour of mixtures containing plastic waste and conventional bed materials under conditions relevant for methane-oriented hydrogasification. In this perspective, the present work addresses this gap by experimentally investigating the fluidization behaviour of plastic–alumina systems, whose results and modelling development are discussed in detail in Chapter VI.

Chapter III.
Aim of the thesis

As discussed in the previous chapters, the conversion of carbonaceous materials—particularly plastic waste—represents a major challenge in the modern era, with significant implications for energy sector development and environmental pollution mitigation.

This Ph.D. project was co-funded by ENEA (*Agenzia nazionale per le nuove tecnologie, l'energia e lo sviluppo economico sostenibile*) to develop a novel catalyst system for the hydrogasification of carbonaceous materials. The main objective is to recover the value of waste by converting it into a gaseous stream, primarily composed of methane, which can be utilized as synthetic natural gas.

At present, various solutions are applied to process biomass/ carbonaceous materials, but none of them allows for reaching a competitive conversion efficiency. Moreover, plastic waste is predominantly converted via pyrolysis, and research on its hydrogasification as a route to methane production remains limited.

Therefore, this project has been designed to pursue a sustainable and innovative approach to waste valorization through methane-rich gas production.

The research was structured around the definition and development of multiple strategic objectives:

- first, identifying the optimal catalytic formulation capable of providing high selectivity and activity;
- second, performing experimental tests to assess the feasibility of the process within a structured catalyst-based reaction system;
- finally, evaluating the fluidizability of the binary system composed of plastic waste and powdered catalysts.

It should be emphasized that the preliminary study of the process was performed at the ENEA-Casaccia research laboratories, while the study of the fluidization of the support–plastic system was undertaken during the abroad research period at the University of Zaragoza (Spain). In particular, the research study on fluidization focused on the identification of operating

conditions allowing stable fluidization of plastic–alumina mixtures, as a preliminary step toward potential implementation in fluidized-bed reactor configurations.

Chapter IV.
Materials and methods

IV.1 Plastic waste matrix

The plastic waste matrix (Figure IV.1) has been provided by ENEA Centro Ricerche Casaccia. The sample consists of a heterogeneous fraction of mixed plastic waste that cannot be effectively recycled through conventional mechanical processes. It is primarily composed of PE (polyethylene) and PP (polypropylene) but also contains non-plastic impurities such as paper residues. In Italy, this type of material is commonly referred to as “plasmix”.



Figure IV.1 *Plastic waste matrix supplied by ENEA Centro Ricerche Casaccia*

IV.1.1 Pretreatment of the plastic waste matrix

The plastic waste used in the experimental test was pretreated using the grinder shown in Figure IV.2, in order to uniformize the shape and the size of

the particles. The grinder apparatus has a rated power of 2500 W and a rotational speed up to 36000 rpm.



Figure IV.2 Grinder used for shredding the plastic waste

Shredding of the samples was also necessary and crucial for the fluidization experiments, for which the grinded plastic waste was sieved in the following granulometry: 180-355 µm, 355-500 µm, 500-1000 µm, 1000-1250 µm, 1250-1650 µm, 1650-2500 µm.

IV.1.2 Thermogravimetric analysis (TGA)

A thermogravimetric analysis coupled with a mass spectrometry analysis has been performed to evaluate the weight loss and species obtained from the depolymerization of the plastics. The analysis was performed using a TA Instruments Q600 thermogravimetric balance, coupled with a mass spectrometer (TG-MS) to analyze the gases released during heating. This setup enables the determination of both the temperatures at which mass loss occurs and the molecular structures involved. The analysis was carried out in a nitrogen atmosphere (100 mL/min), with heating ramp of 10, 20 and 30 °C/min up to 1000 °C.

IV.1.3 Kinetic evaluation of thermal degradation of plastic waste

The kinetic analysis of thermal degradation of plastic waste was performed using the Kissinger method. This method is one of the most popular approaches for determining kinetic parameters, since it is rapid and easy to use, and requires a series of experiments at different heating ramps (generally

three or four). The temperatures of the maximum decomposition peaks, obtained from TGA, were implemented in the model to obtain the activation energy of the depolymerization step.

Generally, the conversion of plastics pyrolysis can be written as follow (eq. (34)):

$$\alpha = (m_0 - m_t)/(m_0 - m_f) \tag{34}$$

where α is the reaction conversion, m_0, m_t and m_f refer to the mass of the sample at the beginning and final time t, respectively. The rate of conversion can be expressed by the following basic rate equation (eq. (35)):

$$d\alpha/dt = k(T)f(\alpha) \tag{35}$$

where $f(\alpha)$ is a mathematical model that simulates the reaction, and the parameter k is the temperature T dependence of the rate of weight loss, which can be obtained from the Arrhenius equation (eq. (36)):

$$k = Aexp\left(-\frac{E}{RT}\right) \tag{36}$$

where A is pre-exponential factor, E is the activation energy, R is the gas constant.

By combining the last two equations, the reaction rate can be given as (eq. (37)):

$$d\alpha/dt = Aexp\left(-\frac{E}{RT}\right)f(\alpha) \tag{37}$$

For the function of the conversion (eq. (38)):

$$f(\alpha) = (1-\alpha)^n \tag{38}$$

Where n is the empirical order of the reaction.

Then the rate of the conversion can be written as (eq. (39)):

$$d\alpha/dt = Aexp\left(-\frac{E}{RT}\right)(1-\alpha)^n \tag{39}$$

Taking the derivative from both sides (eq. (40)):

$$\frac{d}{dt}\left(\frac{d\alpha}{dt}\right) = A(1-\alpha)^n\frac{d\left[exp\left(-\frac{E}{RT}\right)\right]}{dt} + Aexp\left(-\frac{E}{RT}\right)\frac{d[(1-\alpha)^n]}{dt} \tag{40}$$

The heating rate is assumed as $\beta = dT/dt$. Combined with eq. (28), a new equation can be obtained as follows (eqs. (41) and (42)):

$$\frac{d}{dt}\left(\frac{d\alpha}{dt}\right) = A(1-\alpha)^n exp\left(-\frac{E}{RT}\right)\frac{\beta E}{RT^2} - Aexp\left(-\frac{E}{RT}\right)n(1-\alpha)^{n-1}\frac{d\alpha}{dt} \tag{41}$$

$$\frac{d}{dt}\left(\frac{d\alpha}{dt}\right) = \left[\frac{\beta E}{RT^2} - Aexp\left(-\frac{E}{RT}\right)n(1-\alpha)^{n-1}\right]\frac{d\alpha}{dt} \tag{42}$$

The reaction rate will rise to a maximum value and then return to zero when the reactant is exhausted. The maximum rate occurs when its derivative is zero (eq. (43)):

$$\frac{\beta E}{RT_p^2} = Aexp\left(-\frac{E}{RT_p}\right)n(1-\alpha)^{n-1} \quad (43)$$

where T_p is the reaction exothermic peak temperature.

When n=1, eq. (43) becomes (eq. (44)):

$$\frac{\beta E}{RT_p^2} = Aexp\left(-\frac{E}{RT_p}\right) \quad (44)$$

In the KAS method (Kissinger, 1956), when n≠0 and n≠1, Coats-Redfern approximation is used as follows (eq. (45)):

$$n(1-\alpha)^{n-1} \approx 1 + (n-1)\left(\frac{2RT_p}{E}\right) \approx 1 \quad (45)$$

Recalling eq. (32) and rewriting it in eq. (46):

$$\frac{\beta}{T_p^2} = \frac{AR}{E}exp\left(-\frac{E}{RT_p}\right) \quad (46)$$

Taking the natural logarithm, the Kissinger method is written as (eq. (47)):

$$ln\left(\frac{\beta}{T_p^2}\right) = ln\left(\frac{AR}{E}\right) - \frac{E}{RT_p} \quad (47)$$

Therefore, $ln\ \beta/T_p^2$ must have a good linear relation with $1/T_p$ with $-(E/R)$ as the slope, from which it is possible to calculate the activation energy.

IV.2 Carrier for the structured catalyst

The Oxide Bonded Silicon Carbide (OBSiC) foams used for the structured catalyst have a diameter of 6 cm and a height of 2 cm.

The choice of using a structured catalyst is based on several key advantages. These include a high gas/solid contact surface per unit volume, which improves reaction efficiency, and low-pressure drops, even at high flow rates, which supports smoother operation. Additionally, the structured catalyst minimizes mass transfer resistance, enhancing the overall reaction process.

The material used for the carrier has excellent thermal conductivity, helping to reduce thermal gradients within the foam structure. This leads to improved thermal control, ensuring a more uniform temperature distribution during catalytic processes, which is crucial for maintaining reaction efficiency and stability.

IV.3 Preparation of the structured catalyst

The preparation procedure (Figure IV.3) for the structured catalysts involved two main phases: dip-coating (in a washcoat slurry) and wet impregnation (in a defined salt solution), to deposit the a γ-Al_2O_3 support layer and active species layer, respectively.

The washcoat slurry was made by dissolving 1 wt% of methyl cellulose in water. Then, 20 wt% of an alumina/pseudoboehmite mixture (ratio 10:3) was dispersed into this solution, with the pH adjusted to 3 using nitric acid (HNO_3) and stirred vigorously. The carriers were dipped into the slurry for 15 minutes, and the excess was removed by centrifuging at 1500 rpm for 5 minutes. Air was injected through the structure to remove any washcoat excess.

After the step of dip-coating, the coated foams were heat-treated in a muffle furnace at 120°C for 2 hours, with a temperature ramp of 10°C/min, followed by further heating at 500°C for 1 hour. This process was repeated until the desired washcoat loading (30 wt% relative to the carrier weight) was achieved.

The ceria promoter was added by multiple wet impregnation steps using an aqueous $Ce(NO_3)_3$ solution (precursor: $Ce(NO_3)_3 \cdot 6H_2O$), alternating with heat treatments at 120°C for 2 hours and at 450°C for 1 hour, until a 10-30 wt% loading (relative to the washcoat) was reached.

Finally, 20-40 wt.% of nickel and 4-8 wt.% of calcium layer (relative to the weight of the previous coatings) was deposited by similar wet impregnation steps using the co-impregnation method. The foams were dipped in a solution of $Ni(NO_3)_2 \cdot 6H_2O$ and $Ca(NO_3)_2 \cdot 4H_2O$ for 15 minutes and later heat-treated at 120°C for 2 hours and then at 600°C for 1 hour. For the catalyst without calcium promotion, the solution contained only nickel nitrate.

Before the tests, the catalyst has been activated using a stream of H_2 (15 vol%) in Ar in order to convert the nickel oxide (NiO) in metallic nickel, which is the active species for the reaction.

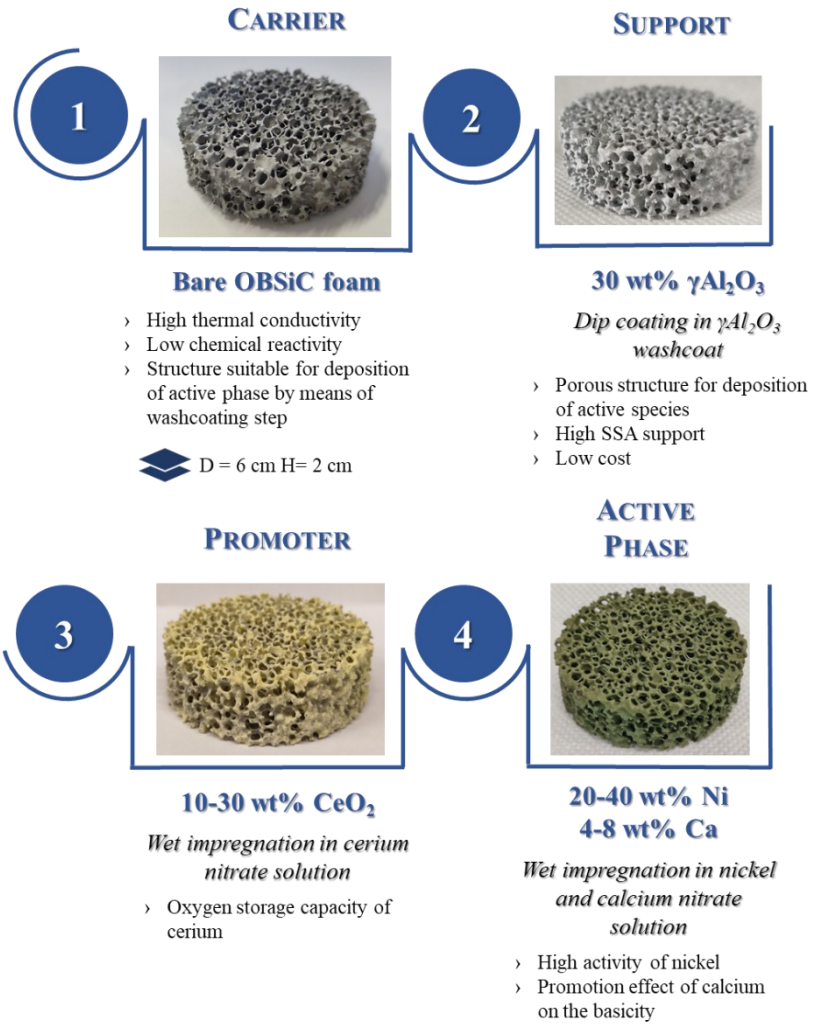


Figure IV.3 *Preparation of the catalytic foam*

IV.4 Preparation of powder catalysts

For the study of fluidization of binary systems of catalyst and plastic waste mixtures, powder catalysts were prepared.

Powder of γ-Al_2O_3 was obtained starting by treating alumina washcoat through a drying step at 120°C followed by a calcination step at 600°C. The support powders were sieved in the following granulometry: 45-90 µm, 90-180 µm, 180-250 µm, 250-355µm.

Following the drying-impregnation procedure, the calcined alumina powder was immersed in cerium nitrate solution at 150°C until dry. The solution was prepared to obtain a 30 wt.% loading of CeO_2 after calcination. The recovered catalyst was dried overnight at 120°C and calcined at 500°C. The deposition of Ni active species was achieved with a second step of drying-impregnation of the cerium-promoted catalyst in a nickel nitrate solution. The same steps of drying and calcination mentioned before were carried out before the activation with the TPR procedure (15%H_2 in Ar) up to 600°C for the conversion of NiO into Ni.

IV.5 Characterization technique

Different physical-chemical analysis techniques were used to characterize the catalysts. The adherence of the catalytic layer to the carriers was evaluated by performing an ultrasound adherence test with an ultrasonic bath CP104 (EIA S.p.A.): the samples, immersed in a beaker containing 25 mL of petroleum ether, were exposed to different cycles of 5 min, applying the 60% of rated power at 25 °C. Each ultrasonic cycle was alternated with a step of drying at 120 °C for 1 h, after which the samples were cooled, and their weight loss was evaluated as (eq. 40):

$$Weight\ loss = \frac{Final\ mass - Inizial\ mass}{Initial\ washcoat\ mass} * 100 \quad (48)$$

The porosity and pore size distribution were evaluated by Hg penetration technique, with a "PASCAL 140" and "PASCAL 240" (Thermo Finnigan Instruments). N_2 physisorption at -196 °C, performed with a Novatouch LX4 (Quantachrome instruments), was used for determining the adsorption-desorption isotherms, the specific surface areas (SSA) (applying Brunauer–Emmett–Teller (BET) method), and the mesopores characterization (with Barrett-Joyner-Halenda (BJH) method).

The morphological analysis was performed by means of a Scanning Electron Microscope (SEM) Philips Mod.XL30 (Amsterdam, the Netherlands), coupled to an Energy Dispersive X-ray Spectrometer (EDS) Oxford (Oxford Instruments, Abingdon, UK) for the elemental analysis.

Temperature Programmed Reduction (TPR) analysis was performed by feeding to the reactor a reducing stream, consisting of 15% H_2 in Ar with a total flowrate of 500-1000 NmL· min^{-1} and raising the temperature from room temperature up to 600°C with a heating rate of 10°C·min^{-1}.

The catalyst acidity and basicity were measured by CO_2 temperature programmed desorption (CO_2-TPD). After the H_2-TPR test, the samples were treated in 5 vol.% of CO_2 in Ar gas mixture at 50°C for 1 h followed by Ar purge. The TPD was performed by flowing Ar in the temperature range of 25–600°C (heating ramp of 10°C· min^{-1}).

The Raman spectra were produced in a dispersive MicroRaman in Via, Renishaw (Renishaw, Wotton-under-Edge, UK), equipped with a 514 nm Ar ion laser, in the range 200-2000 cm^{-1} Raman shift. Once selected, the optimized laser power of 25 mW was applied to all the samples.

IV.6 Experimental plant

The experimental plant used for testing the catalysts is sketched in Figure IV.4 and has three different sections.

a) Feeding section: an MFCs (mass flow controllers) battery is used for the regulation of flow rates of reactant and product gases. The gases are H_2 and He, for the reaction, and also CO, CO_2, CH_4, (and if necessary C_2H_6 and C_3H_8) for the mass spectrometer calibration; the N_2 is used for the cooling of the reactor.
b) Reaction section: first preliminary tests were performed in a reactor with a diameter of 1.5 cm and a length of 40 cm, arranged in an oven able to reach the reaction temperature. Two thermocouples, one on the plastic waste bed and one on the catalyst bed, are used to measure the temperatures; a pressure traducer measure the pressure upstream of the reactor. A detailed representation of this section is reported in Figure IV.5. The gaseous products go through a tube heated up to 200°C and then undergo a quick cooling in a flask dipped into a refrigerant liquid at 0°C. This step allows to condensate the heavier hydrocarbons produced by the reaction. A detailed representation of this section is reported in Figure IV.5.
c) Analysis section: a mass spectrometer is employed for the continuous monitoring of the product-gas composition. Before each experiment, a calibration mixture of known composition is introduced to determine the response factors; once calibration is completed, the test can be initiated.

The preliminary experimental tests performed in the plant in the configuration shown in Figure IV.5 are the following:

- Catalytic and not catalytic pyrolysis (using an inert flow)
- Catalytic and not catalytic hydrogasification (using hydrogen as reactant)

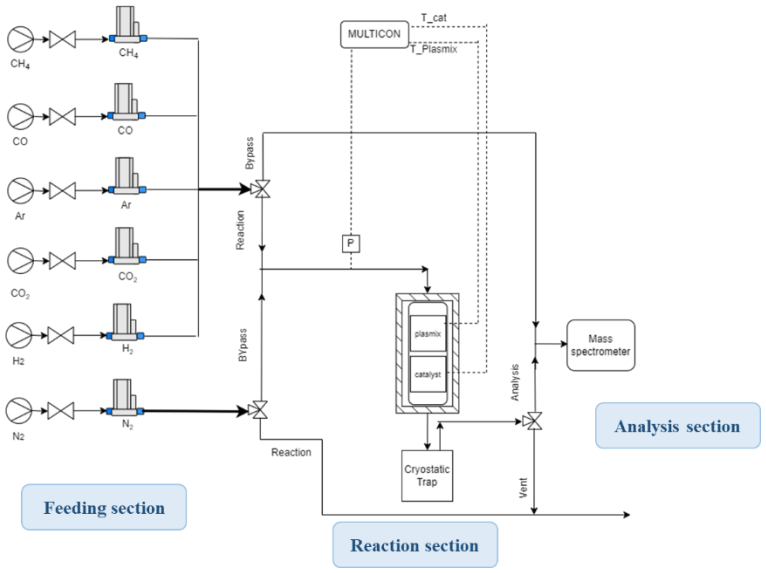


Figure IV.4 *Experimental plant set-up*

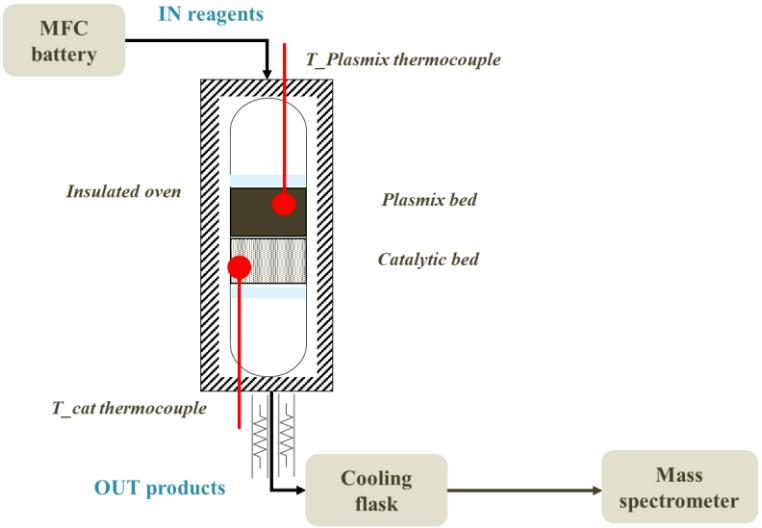


Figure IV.5 *Sketch of the experimental plant with details on the reaction section*

In order to meet methane yield and production enhancement target, a scale-up of the reactor was designed (Figure IV.6a). The scaled-up reactor has a length of 55 cm and a diameter of 7 cm, with a total volume of 2116 cm^3, enabling the conversion of plastic quantities on the order of hundreds of grams. This set-up increases the contact time of the pyrolysis gases over the catalyst, thereby enhancing the conversion to methane.

To further advance process optimization, a new reactor configuration is proposed. As shown in Figure IV.6 this design aims to overcome the limitations associated with in-situ catalytic pyrolysis.

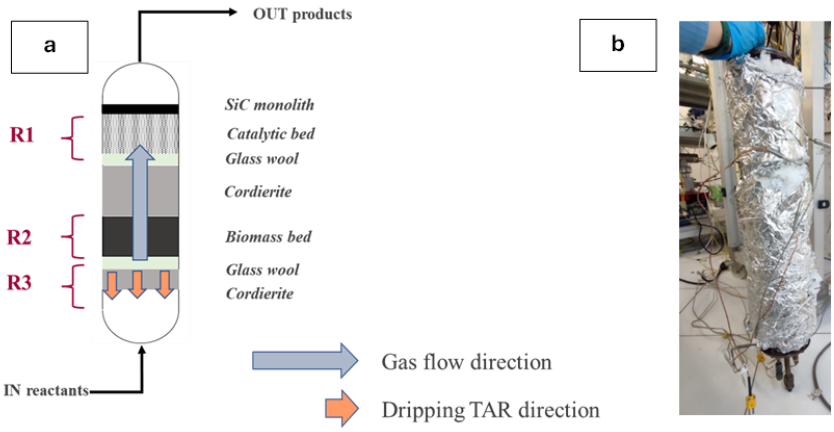


Figure IV.6 *(a) New optimized reactor configuration; (b) Photo of the reactor*

The new integrated optimized configuration proposed here combines the benefits of both stages (pyrolysis and methanation) into a single unit. A cordierite monolith (Figure IV.7) is used to thermally insulate the two zones of the reactor—one for pyrolysis of the plastic waste and the other for the methanation on the catalytic foams—with each zone heated by separate metallic resistances, R_1 and R_2, as shown in the Figure IV.6a. This arrangement allows for independent control of the pyrolysis and methanation temperatures. Moreover, the catalyst is separated from the pyrolysis zone, effectively avoiding the mass and heat transfer issues posed by high plastic viscosity and making the catalyst recovery much easier; lastly, undesirable catalyst deactivation from plastic impurities or coke deposition is limited.

During the pyrolysis of the plastic, TAR (a complex mixture of condensable hydrocarbons) can be generated and drips down to the bottom of the reactor. In this configuration, the dripping TAR flows in countercurrent mode with respect to the inflowing hydrogen, leading to an increase in the contact time with the hydrogen and then to its conversion in the bottom of the reactor. In this zone (heated-up, the temperature is set to be higher than the TAR condensation temperature (the resistance R3 allows the heating of this zone).

The reaction procedure for the test in the scaled-up reactor involves heating the plastic waste only after the catalyst has reached the operating temperature (500–600 °C). The reactant gas (H_2 with an inert) enters the reactor from the bottom and passes through the plastic waste bed which undergoes pyrolysis, once heated up to the appropriate temperatures; the volatile matter then moves

to the catalytic bed where it reacts with the hydrogen to give methane as the main product.

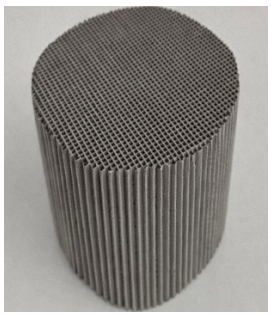


Figure IV.7 *Cordierite monolith used to thermally insulate the reactor zones*

IV.7 Experimental evaluation and prediction of the minimum fluidization velocity

The possibility of fluidizing the binary system alumina-plastic waste was studied in the experimental set-up, shown in Figure IV.8, in the laboratories of the Instituto de Investigación en ingeniería de Aragón (Spain).

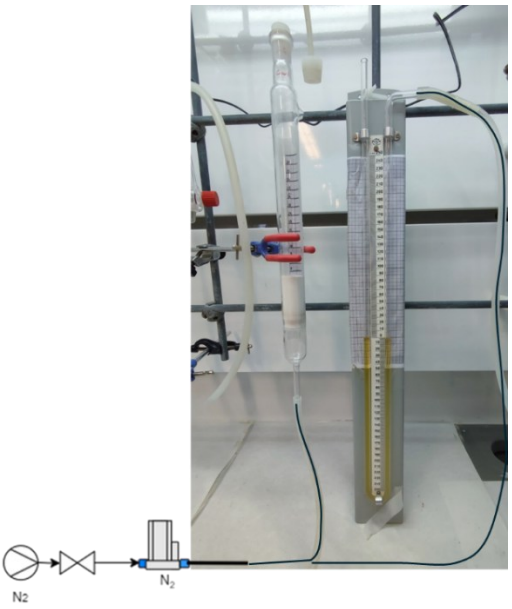


Figure IV.8 *Experimental set-up for the evaluation of the minimum fluidization velocity*

The experiments have been performed with a static bed height of 60 mm in a reactor of 2.66 cm of diameter, using nitrogen at ambient pressure and room temperature as fluidizing gas. The nitrogen injected flow was controlled by a mass flow controller by Alicat, with a full scale of 2500 $NmL \cdot min^{-1}$. Particles of plastic waste and alumina of each size, determined in the sieve analysis, have been introduced through the top of the column in order to reach the established height. The solids were subjected to strong fluidization for 5 min. Then, the flow of nitrogen was stopped, thereby obtaining a perfectly mixed solid bed. Later, the pressure drop method was used to determine the minimum fluidization velocity. In particular, the U_{mf} was determined from the intersection of the slope curve (which is the Ergun equation when inertial term is negligible – eq. 41), which corresponds to the initial velocity of the nitrogen under the fixed bed condition, with the horizontal line representing the constant pressure drop through the bed (eq. 42). For each injected flow, pressure drop was measured on the U-manometer and recorded. Three experimental runs were carried out for each particle diameter, and the average of the obtained values was taken as the final value.

$$\Delta P_l = \frac{150(1-\varepsilon)^2}{\varepsilon^3} \cdot \frac{\mu_f H}{\left(\phi d_p\right)^2} U = k(\mu_f, L, \varepsilon, d_p, \phi) * U \tag{49}$$

$$\Delta P_{max} = \frac{M_{solid} * g}{S} \tag{50}$$

The experimental results have been compared to the predictions of the correlations previously reported in the literature.

The model equation for the prediction of the minimum fluidization velocity for alumna particles is the eq. (29) reported in the previous chapter, where the values of constants K_1 and K_2 were adequately obtained with the fitting of experimental data.

The data of binary mixtures were fitted used the equation:

$$Re_{mf\,mix} = \left[K_1^2 + \left(K_2 \cdot (1 - x_p) + K_3 \cdot x_p^{\frac{1}{2}}\right) \cdot Ar_{mix}\right]^{1/2} - K_1 \tag{51}$$

Which recalls (Paudel & Feng, 2013) correlation for binary mixtures of biomass and inert particles, and where the parameters are defined as:

$$Re_{mf\,mix} = \frac{U_{mf} \cdot d_{mix} \cdot \rho_f}{\mu_f} \tag{52}$$

$$Ar = d_{mix}^3 \frac{\rho_f \cdot (\rho_{mix} - \rho_f) \cdot g}{\mu_f^2} \tag{53}$$

$$\frac{1}{\rho_{mix}} = \frac{x_p}{\rho_p} + \frac{x_s}{\rho_s} \tag{54}$$

$$d_{mix} = d_p \cdot d_s \cdot \left[\frac{x_p \cdot \rho_p + x_s \cdot \rho_s}{x_p \cdot \rho_p \cdot d_p + x_s \cdot \rho_s \cdot d_s}\right] \tag{55}$$

The subscript “s” stands of alumina, while “p” stands for plastic.

IV.8 Experimental evaluation

The operating conditions used for the tests are briefly reported in this paragraph.

IV.8.1 Preliminary tests evaluation

The operating conditions used for the tests are briefly reported in this paragraph.

The preliminary tests were conducted (in the plant sketched in Figure IV.5) according to the following logic:

- Firstly, non-catalyzed pyrolysis tests provided insight into the gas productivity and methane selectivity of the thermal decomposition of plastic waste.
- Subsequently, the structured catalyst was employed to evaluate its potential to increase methane yield without introducing additional reactants into the inert atmosphere.
- Finally, the introduction of hydrogen into the inlet stream w/o the catalyst allowed the assessment of its role in catalytic versus non-catalytic pyrolysis.

These tests were performed with a volumetric flow rate of 200 $NmL \cdot min^{-1}$ (80 vol.% of H_2 in Ar). The reactor (diameter of 1.5 cm) was fed with batches of 2 g of plastic; each test was conducted with a mass ratio catalyst/plastic of 2/3, resulting in a weight hourly space velocity of 2.56 $g_{gas} \cdot g_{cat}^{-1} \cdot h^{-1}$. The thermal decomposition was carried out at a heating rate of 40 $°C \cdot min^{-1}$ up to approximately 550 °C. The outlet tube of the reactor was maintained at 200 °C, and the stream was subsequently cooled to 0 °C in the condenser.

The results are discussed in the next section and are shown in terms of partial pressure as a function of reaction time. They have been used to elucidate the overall reaction mechanism for the degradation of mixed plastics.

Alongside the quantitative evaluation, a qualitative analysis was also conducted by calculating the gas selectivity, defined as (eq. (56)):

$$Gas\ Selectivity = \frac{m_{gas,i}}{\sum_i m_{gas,\,i}} x100 \tag{56}$$

$$m_{gas,\,i} = mass\ of\ the\ gaseous\ species\ i$$

IV.8.2 Test performed in the new reactor configuration

The new reactor configuration was tested with different amounts of plastic waste (70 and 105 g) to assess the influence on methane productivity. The

tests were performed with five catalytic foams and a total flow rate of 180 $NmL \cdot min^{-1}$, consisting of 95 vol.% H_2 in He, and the selectivity to methane, ethane, and propane was calculated.

Key Performance Indicators and Assessment Criteria

In order to quantitatively assess the effectiveness of the proposed catalytic formulations and reactor configurations, a set of key performance indicators (KPIs) was identified. These parameters provide objective criteria for evaluating catalytic performance, process efficiency, stability, and scalability of the hydrogasification process.

- **Methane-rich gas production**

Achievement of a methane-rich product stream under catalytic hydrogasification conditions, ensuring stable methane generation during time-on-stream.

$$\beta = \frac{Nm^3_{metano}}{ton_{\ bio}}$$

- **Hydrogen utilization efficiency**

Quantification of hydrogen consumption relative to the plastic feedstock, with the aim of evaluating the energetic feasibility of the process.

$$\alpha = \frac{kg_{idrogeno}}{ton_{\ bio}}$$

- **Carbon conversion and overall gas yield**

Determination of the distribution of gaseous, liquid, and solid products, verifying effective carbon valorization into methane-rich gas.

$$K = \frac{Nm^3_{gas}}{ton_{\ bio}}$$

- **Catalyst stability and regenerability**

Evaluation of catalyst performance under increased plastic load, resistance to coke formation, and recovery of activity after regeneration treatments.

The quantities appearing in the numerators were calculated by integrating the mass flow rates over time.

IV.8.3 Fluidization test performances evaluation

Evaluation of the performances of the fluidization test involved the assessment of hydrodynamic operability for future scale-up, that is the identification of operating conditions allowing stable fluidization of plastic–alumina mixtures, as a preliminary step toward potential implementation in fluidized-bed reactor configurations.

IV.9 COMSOL Multiphysics Simulations

A preliminary CFD evaluation of thermal insulation provided by the cordierite monolith within the reactor has been performed using Comsol Multiphysics ® software.

The cordierite monolith was modelled coupling the physics of *Laminar flow* and *Heat Transfer in Fluids and Solid* in the software COMSOL Multiphysics version 5.4. The first physics describes the flow both in free and porous media, while the second allows the description of solid domains too.

Fluid dynamic study

Navier-Stokes equation for the conservation of momentum (eq. (57)) is used to describe the fluid motion in free regions coupled with the continuity equation for conservation of mass (eq. (58).

$$\rho(\boldsymbol{u}\cdot\nabla)\boldsymbol{u} = \nabla\cdot[-p\boldsymbol{I}+\boldsymbol{k}]+\boldsymbol{F} \tag{57}$$

$$\nabla\cdot(\rho\boldsymbol{u}) = 0 \tag{58}$$

Boundary conditions involved the no slip conditions at the reactor wall, and the initial value of velocity of the fluid set to zero.

The heat transfer equations were applied to fluid domains (eq. (59) and eq. (60)) and solid domains (eq. (61)). For what concerns boundary conditions, the parameters were set as follows:

- The temperature in the inlet section is set to 25°C
- Thermal insulation of the reactor
- A constant temperature of 600 °C was set at the reactor wall in the zone below the cordierite monolith. This boundary condition was allowed by experimental temperature control, which was performed through three different heating zones.

$$\rho C_p\boldsymbol{u}\cdot\nabla\mathrm{T} = \nabla\cdot[k\nabla\mathrm{T}]+Q \tag{59}$$

$$q = -k\nabla\mathrm{T} \tag{60}$$

$$\nabla\cdot(k\nabla\mathrm{T})+\mathrm{Q} = 0 \tag{61}$$

Boundary conditions are necessary to solve these equations.

The COMSOL library of materials was used to associate materials to each domain; in particular, stainless steel for the reactor, cordierite for the monolith, helium for the gas, and glass wool bat for the mat used around the monolith.

Chapter IV

Chapter V.

Characterization results

Preliminary activities involved the characterization of both plastic waste feedstock and the catalysts. The catalysts were prepared in both structured and powder forms, and a catalytic formulation was developed based on insights from the literature. Characterization results are discussed in this chapter.

V.1 Plastic waste matrix characterization

The elemental analysis is reported in Table V.1. No chlorine content was detected, thereby confirming the complete absence of chlorine-containing species in the sample.

Table V.1 *Elemental Analysis of the plastic waste sample*

(C) %	(H) %	(N) %	(S) %	(O) %
77.548	10.750	0.361	0.000	11.341

The plastic sample before and after the mechanical grinding is shown in Figure V.1.

The untreated material consists of large, heterogeneous plastic fragments of various shapes and colors, whereas the ground sample shows a finer and more homogeneous particle-size distribution. Reducing the particle size improves the handling of the solid matrix, enhances heat and mass transfer during thermochemical conversion, and ensures a more uniform contact between the feedstock and the catalyst, ultimately leading to more reproducible and efficient processing.

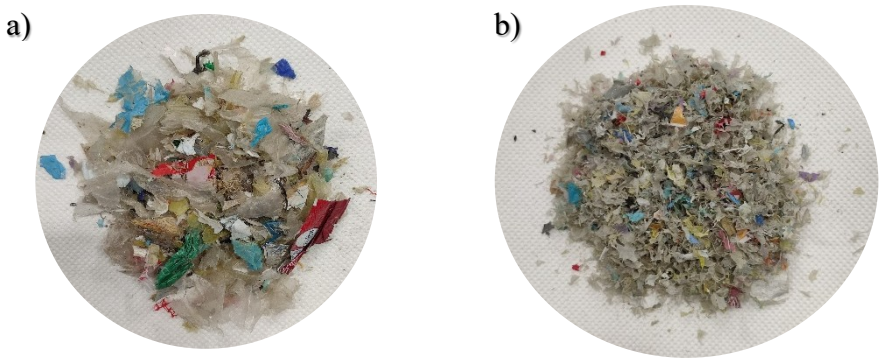
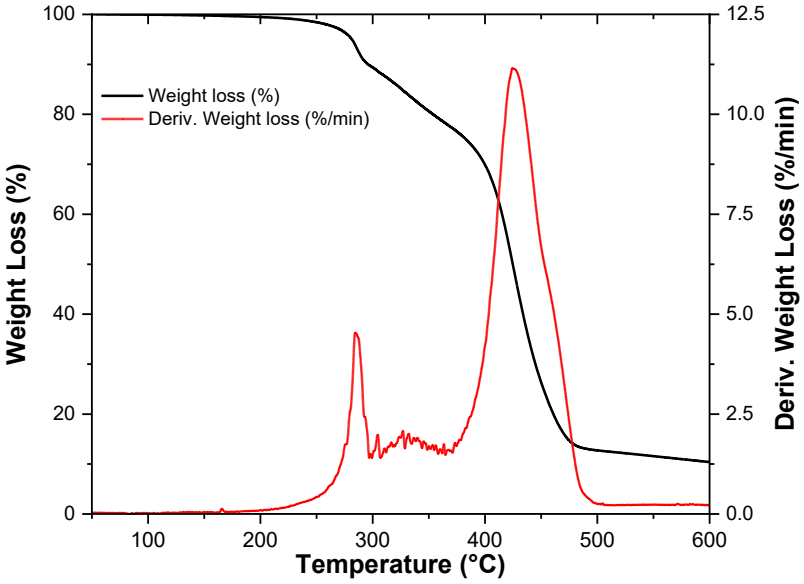


Figure V.1 *Plastic waste sample before (a) and after (b) mechanical grinding*

Initially, a Thermogravimetric Analysis (TGA) was conducted to evaluate the temperature range at which the plastics experience weight loss under pyrolysis conditions. The results of the TGA test are reported in Figure V.2.

The analysis in an inert atmosphere has shown that under N_2 pyrolysis conditions, the plastic waste degradation happens in the range 250-450°C with a maximum weight loss at 430 °C, where 90% of the sample pyrolyzes. The results are coherent with the characterization made by Xuan, et al. (Xuan et al., 2023) who reported the peak temperatures for PE and PP at 450°C and 430°C, respectively, and by Xu et. (Xu et al., 2018) who found a PP pyrolysis interval of 319-551 °C for the thermal degradation with a heating rate of 100 °C·min^{-1}. Methane, as well as hydrocarbons with 2, 3 and 4 carbon atoms (C_2-C_4) and aromatics have been detected among the gases generated from the degradation, as reported in Figure V.2b.

The curves of degradation at different heating ramps (10, 20, and 30 °C·min^{-1}) are shown in Figure V.3. The effect of the heating rate on the thermal decomposition characteristics (onset, peak, and final temperatures) are shown in Table V.2: all the temperatures are shifted to a higher value when the heating rate is increased, as also reported by different researchers (Woo Park et al., 2000; Wu et al., 1993; Yang et al., 2001). Moreover, the increase of the peak intensity is an indication of a change in the reaction mechanism depending on the temperature heating rate (Tian et al., 2016; Wu et al., 1993).



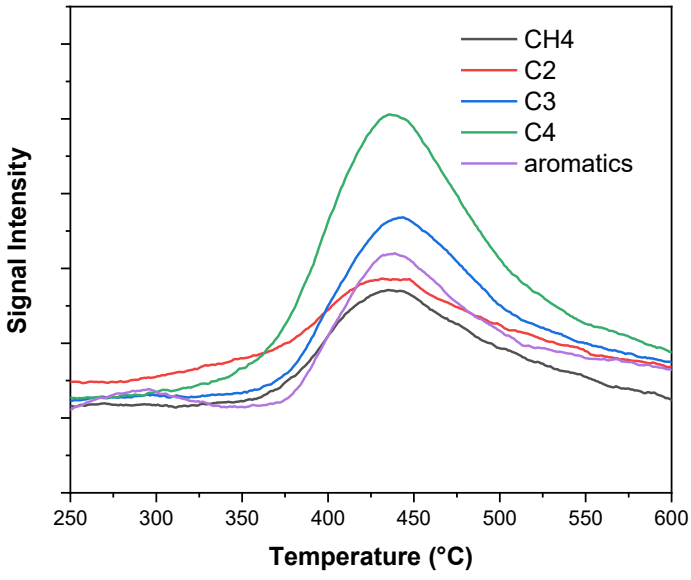


Figure V.2 *TG-MS results on the plastic waste sample: a) TG (weight loss and derivative weight loss) curves; b) MS curves from the plastic sample pyrolysis*

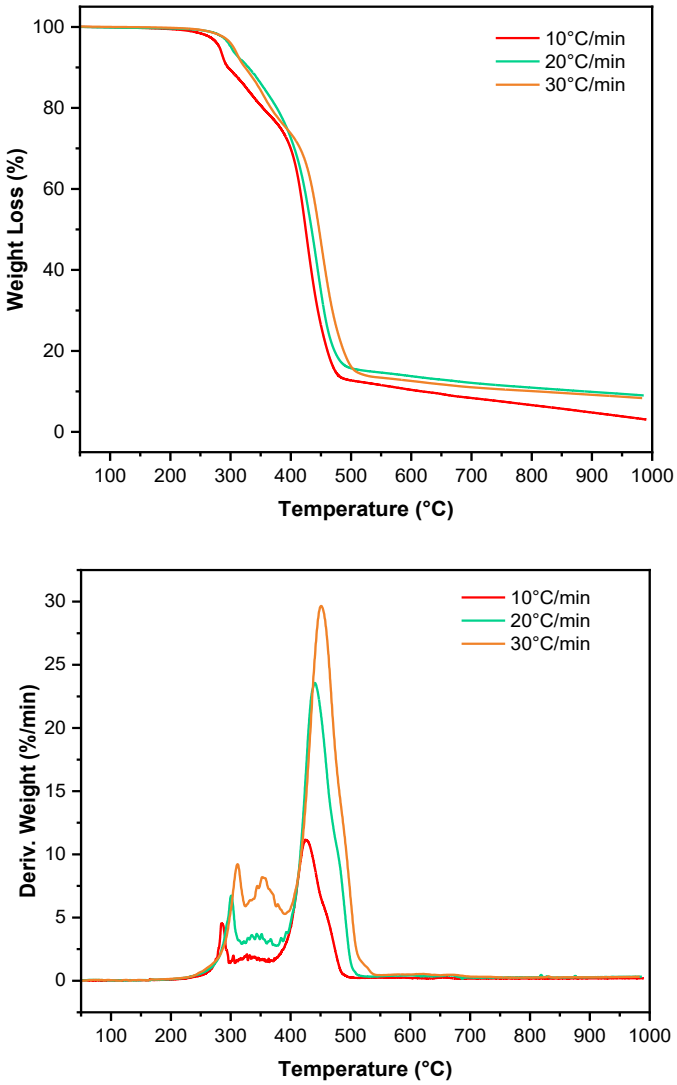


Figure V.3 *TGA and DTGA curves for plastic waste pyrolysis at different heating ramp*

Table V.2 *Onset, peak, and final temperatures for the tests on plastic waste at different heating rates*

Test	Heating rate (°C/min)	T onset (°C)	T peak (°C)	T final (°C)	Overall mass loss (%)
1	10	269	425	490	97
2	20	280	445	500	97.8
3	30	288	453	520	91.6

The experimental values of peak temperatures were employed in the Kissinger method in order to evaluate the activation energy of thermal degradation of plastic waste. Activation energy is used to define the energy barrier to be overcome in the chemical reaction, which means the minimum energy required for a chemical reaction to occur. Therefore, a reaction starts easier in the case of lower activation energy values (Xu et al., 2018). Knowing the activation energy of plastic pyrolysis is essential for understanding the thermal reactivity of the material and for defining the operating conditions required to initiate and sustain its degradation. Since the activation energy determines how strongly the reaction rate depends on temperature, it provides a quantitative indication of the temperature threshold needed to achieve significant conversion. This information is crucial for the design and optimization of the pyrolysis step, as higher activation energies require higher temperatures to reach comparable reaction rates.

The linear data fitting is shown in Figure V.4. The value of the activation energy E can be calculated from the slope (-18594) multiplied by the gas constant R, yielding 154 $kJ \cdot mol^{-1}$, with a R^2 of 0.99017. This value aligns well with literature data (Choi et al., 2024; Xu et al., 2018), especially considering that the plastic waste analyzed in this work consists of a mixture of different polymers. In particular, (Xu et al., 2018) obtained activation energy values of 180 $kJ \cdot mol^{-1}$ for LDPE, 110 $kJ \cdot mol^{-1}$ for PP and 50$\cdot mol^{-1}$ for the first stage and 113$\cdot mol^{-1}$ for the second stage for PVC, concluding that the degree of difficulty in the pyrolysis process can be ranked as PVC < PP < LDPE. The difference in activation energy is due to the difference in the number and type of bonds, such as C-C, C-H, C-C and C-Cl. The dissociation energy of C-C, C-H and C-C bonds are 347, 414 and 611 $kJ \cdot mol^{-1}$, respectively, while the energy for the breaking of C-Cl is 339 $kJ \cdot mol^{-1}$.

The activation energy values are influenced by various factors, such as heating rate, the source of materials, experimental apparatus and so on. Thus, the results of activation energy for plastic waste were only applied to the experimental condition in this study, and it also had a reference value for similar research.

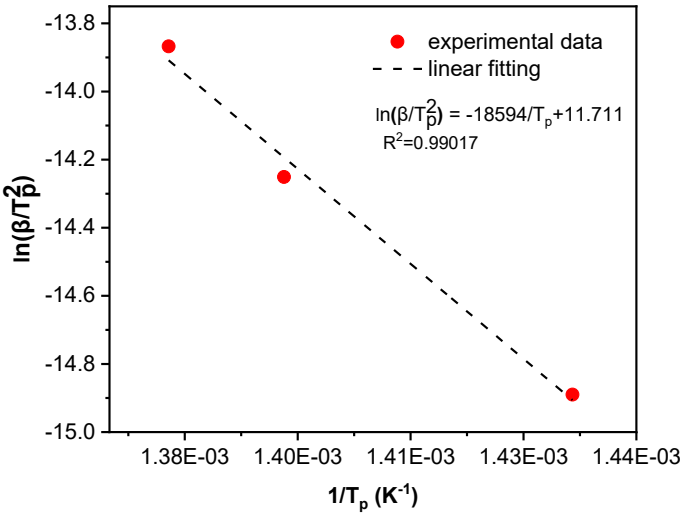


Figure V.4 *Estimation of activation energy for plastic waste thermal degradation using the Kissinger method*

V.2 Catalyst Characterization

V.2.1 Structured catalyst characterization

To evaluate the resistance of the catalytic coating on the foam, an ultrasonic adhesion test was performed. The results (Figure V.5) show that the main weight loss (about 2%) occurs after the first cycle, and that the maximum weight loss remained considerably below 10%, typical value of the structured catalysts in literature (Valentini et al., 2001) with the value for the last cycles being approximately 2.5%. These results demonstrated that the final catalyst exhibits excellent resistance to mechanical stress and strong coating adhesion.

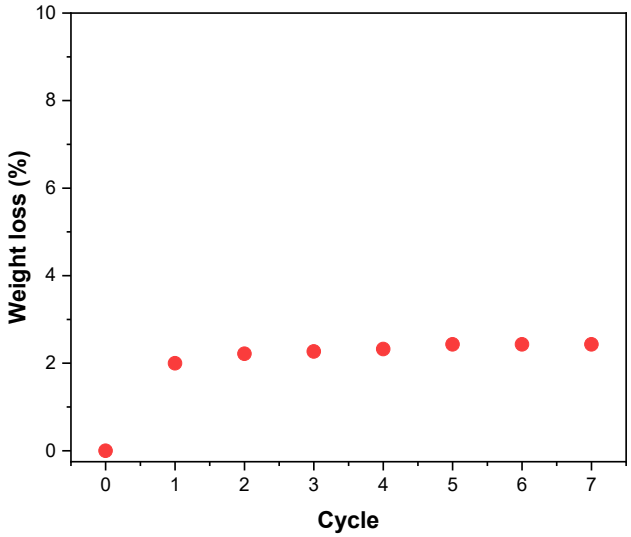


Figure V.5 *Results of the ultrasound adherence test on structured catalyst*

The mercury intrusion porosimetry was performed on samples of the structured catalysts. The results on the 20 wt% Ni/ 10 %wt. CeO_2/ 30 wt. % γ-Al_2O_3/ OBSiC are reported in Figure V.6. The curves of the porous distribution confirm the formation of pores with an average diameter of approximately 0.01 μm on the final catalysts (red curve), mainly ascribable to the presence of the γ-Al_2O_3 layer, which are not present in the bare foam (blue curve) The non-zero slope of the total volume intruded curve at small pore size for the catalytic sample indicates the presence of micropores.

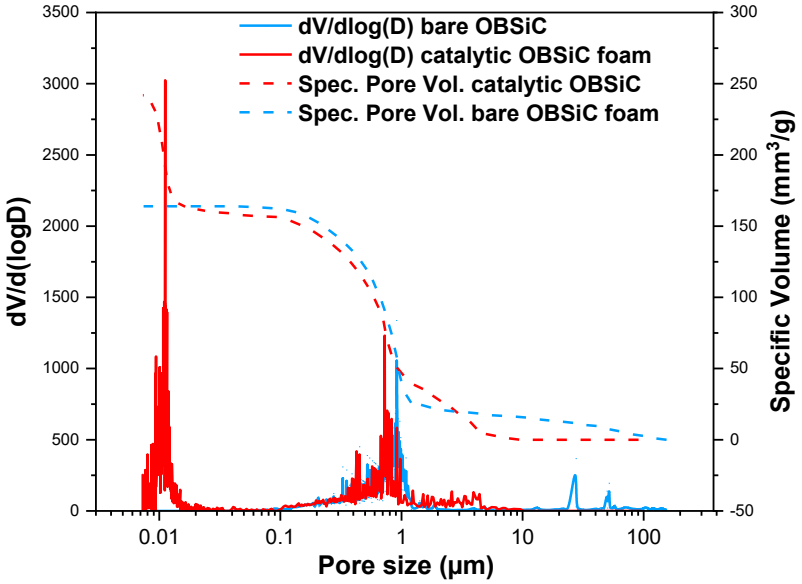


Figure V.6 *Pore distribution of the samples*

N_2 adsorption at 77 K technique has been employed to characterize the textural properties of the samples, providing quantitative information on specific surface area, pore volume, and pore-size distribution.

The Figure V.7 shows the isotherms resulting from the N_2 physisorption tests on the bare and Ni-catalyzed OBSiC foams. According to IUPAC classification, these isotherms are IV(a) type ones, which are typical of mesoporous materials, with a hysteresis of type H2b indicative of pore-blocking affected desorption (Cychosz et al., 2017; Cychosz & Thommes, 2018). Comparing the shapes and intensity of curves, it is evident that the catalyzed foams not only has an increased mesoporous structure and pore volume (which goes from 0.002 $mL \cdot g^{-1}$ for the bare foam to 0.062 $mL \cdot g^{-1}$ for the catalyzed one), but also an increased microporous fraction, as the height of the curve at lower values of relative pressure P/P_0 increases from 0.1 to 3.4 $mL \cdot g^{-1}$. Moreover, the BET method has been used to evaluate the Specific Surface Area (SSA): its value goes from 0.8 (bare foam) to 21.5 (catalytic foam) $m^2 \cdot g^{-1}$. The marked rise in SSA is mainly due to the γ-Al_2O_3 coating, which provides a highly porous and rough surface, thereby increasing the accessible area available for catalytic interactions. Notably, the deposition of the active phases does not obstruct the pores generated by the γ-Al_2O_3 coating, indicating that the catalytic formulation preserves the textural properties of the support.

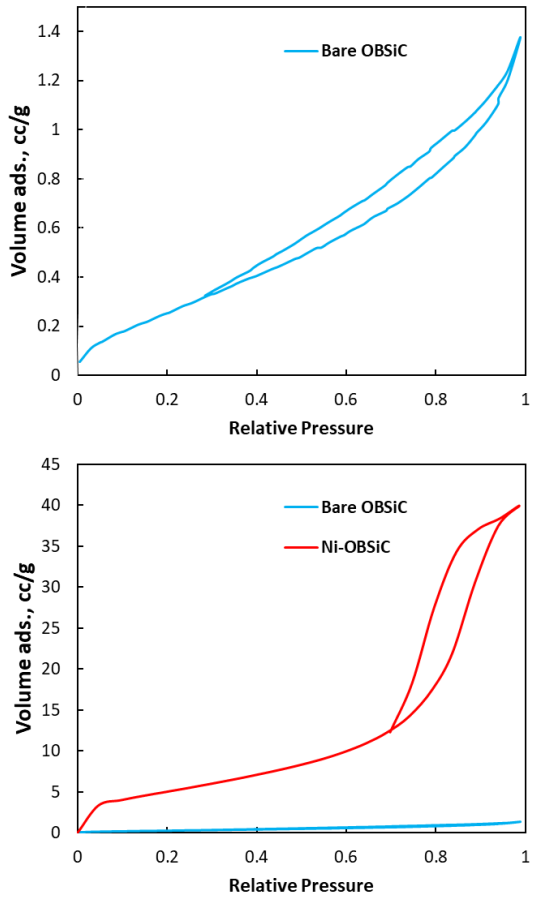


Figure V.7 *N_2 at 77K adsorption-desorption isotherms for a) the bare OBSiC foam and b) the catalytic foam*

The distribution of nickel, cerium and calcium was evaluated through SEM-EDX characterization, obtaining the elemental maps reported in Figure V.8. The analysis was performed on the catalyst with 40 wt.% Ni and 8 wt.% Ca, which is the catalyst with the highest loading of active species.

From the images, it is possible to appreciate the homogeneous distribution of the deposited Ni and Ca onto the cerium-promoted alumina-supported foam. This is particularly important for the availability of the active sites and confirms the suitability of the selected catalyst preparation method and of the nickel precursor employed.

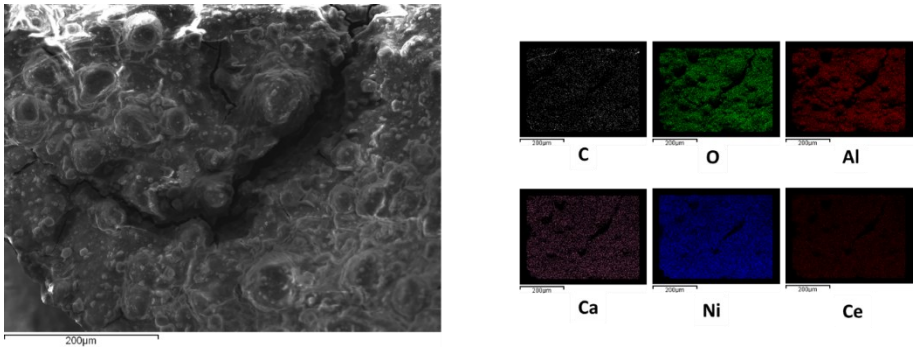


Figure V.8 *SEM-EDX images of the fresh sample 40 wt.% Ni/ 30 wt.% CeO_2/ 30 wt.% Al_2O_3/ OBSiC*

The activation of the catalysts was carried out using the Temperature Programmed Reduction (TPR) procedure, which involves exposing the catalyst to a reducing atmosphere (15 vol. % of H_2 in inert) while heating up to 600°C. The resulting reaction is the following (eq. (62)):

$$NiO + H_2 \rightleftharpoons Ni + H_2O \quad (62)$$

Namely, the nickel oxide on the catalyst is reduced to its metallic form, which is the active species for the methanation reaction. Figure V.9 shows the hydrogen consumption profile, characterized by multiple peaks, indicating the presence of reducible species with distinct reduction behaviors. The low-temperature contribution (221°C and 371°C peaks) is typically associated with the reduction of highly dispersed NiO species that weakly interact with the support. The intermediate-temperature peaks (450 °C) can be attributed to NiO species that strongly interact with the CeO_2 layer or are partially incorporated into the ceria lattice, which require higher temperatures to be reduced. The high-temperature tail (600°C) is consistent with the stepwise reduction of CeO_2 ($Ce^{4+} \rightarrow Ce^{3+}$), and its extent is influenced by the presence of Ni and Ca, which enhance oxygen mobility and modify the redox properties of ceria. The overall profile confirms the coexistence of Ni species with different degrees of interaction with the CeO_2/Al_2O_3 support and highlights the redox contribution of ceria, which plays a key role in the catalyst's oxygen-storage and hydrogen-activation capabilities.

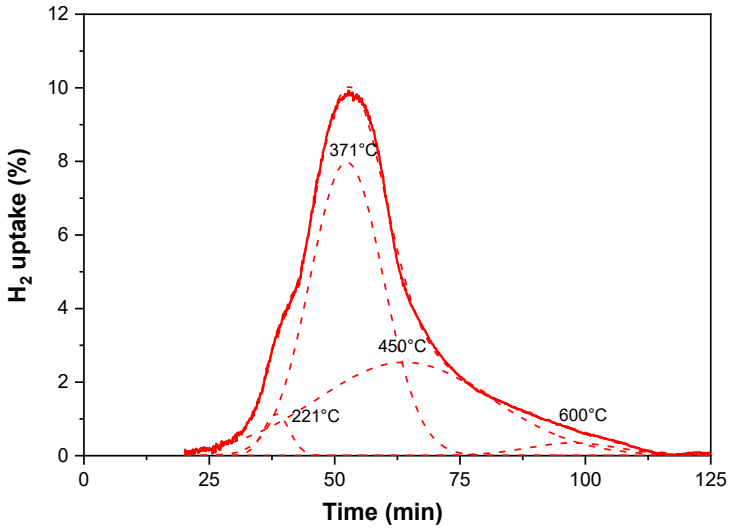


Figure V.9 *H_2 consumption from TPR analysis on 5 catalytic OBSiC foam (40 wt.% Ni/ 8 wt.% Ca/ 30 wt.% CeO_2/ 30 wt.% Al_2O_3)*

Finally, CO_2-TPD characterization was employed to evaluate the acidity and basicity of both fresh and used catalysts, with and without calcium addition. The results are reported in Figure V.10. Literature studies (Ewald & Hinrichsen, 2019; Q. Pan et al., 2014, reported that Ni/γ-Al_2O_3 catalyst can show four different peak ranges: weak adsorption peaks in the range 20-250°C, medium adsorption peaks in the range 300-650 °C and strong adsorption peaks in the range 650-950°C.

For clarity, the desorption features discussed above are interpreted qualitatively according to their temperature range, where low-temperature peaks are associated with weak basic sites, intermediate-temperature peaks with medium-strength sites, and high-temperature peaks with stronger basic sites, consistently with literature classifications for Ni-based catalysts.

The graph of the fresh catalysts reports two main CO_2 desorption peaks, whose deconvolution is shown in the graphs. The first is located around 85-90°C for both the fresh catalysts and is attributed to the weak basic sites. It is worth noting that the weakly adsorption sites in the catalyst with calcium addition are modified, since the deconvolution of the multiple peaks detected a more intense peak around 150°C. Moreover, the calcium-promoted catalyst shows a markedly reduced contribution of high-temperature desorption features (above ~400 °C), suggesting a suppression of the strongest basic sites compared with the non-promoted catalyst. (unlike the non-promoted catalyst), suggesting that calcium is able to modify the interaction between Ni active

sites and support, suppressing the formation of stronger basic sites, and potentially leading to an enhanced methanation power.

The spent catalysts show a broader and higher multipeak in the range of weak and medium basic sites, especially for the calcium-promoted catalyst. These results indicate that the NiCa catalyst can potentially be reutilized in consecutive hydrogenation steps, maintaining its medium basic sites and therefore its methanation capacity.

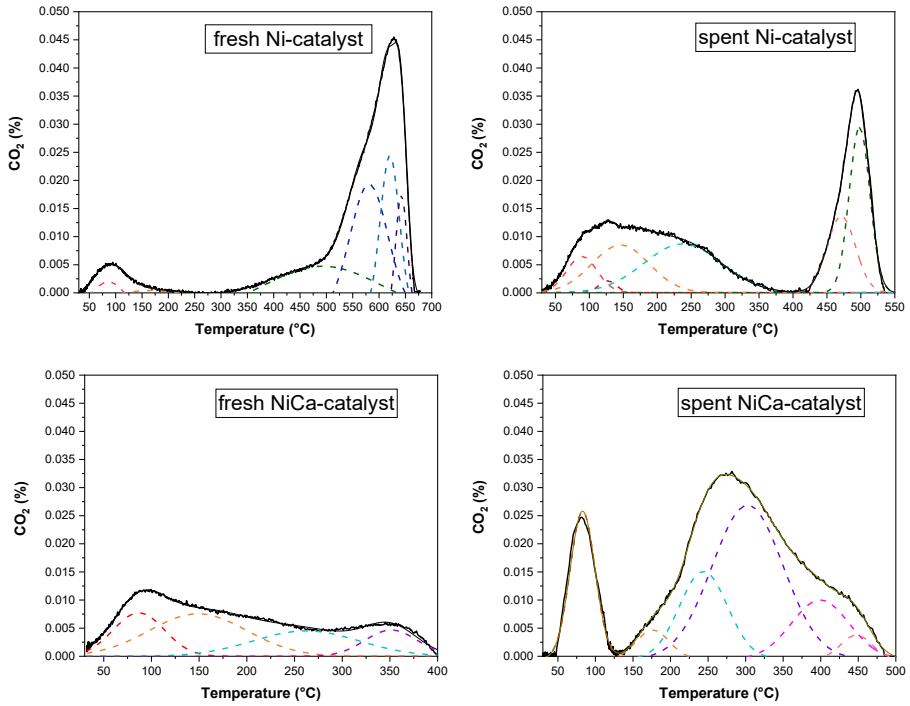


Figure V.10 *CO_2-TPD curves for the fresh and spent 20 wt.% Ni/ 10 wt.% CeO_2/ 30 wt.% Al_2O_3/ OBSiC catalysts and fresh and spent 20 wt.% Ni- 8 wt.% Ca/ 10 wt.% CeO_2/ 30 wt.% Al_2O_3/ OBSiC catalyst*

The Table V.3 reports the temperatures of deconvolution peaks for each curve and the total basicity of each catalyst, calculated by integrating the curves over time. It is worth noting that even though the total basicity of the Ni-catalyzed foam is higher (both for the fresh and spent catalysts) than that of the calcium-promoted foam, the basicity related to the medium basic sites is enhanced when the basic promoter is added to the formulation (from 84 to 68 $\mu mol \cdot g^{-1}_{cat}$ for the Ni-based, while from 38 to 50 $\mu mol \cdot g^{-1}_{cat}$ for the calcium-promoted catalyst). The most significant variation concerns the medium basic sites. Their concentration increases dramatically in the spent Ni catalyst (from 8.5 to 44.8 $\mu mol \cdot g^{-1}_{cat}$), indicating the formation of more reactive O^{2-} species

or monodentate carbonate precursors during operation. The NiCa catalyst already possesses a high density of medium basic sites in the fresh state (33 μmol·g^{-1}_{cat}), which further increases after use (48.2 μmol·g^{-1}_{cat}). This confirms that Ca strongly enhances the presence of medium basic sites, which are typically associated with the formation of monodentate carbonate and monodentate formate species—key intermediates in CO_2 activation and hydrogenation.

This result is coherent with what reported in the literature. Pan et al. (Q. Pan et al., 2014) have proposed that medium basic sites enhance CO_2 methanation activity, while strong basic sites do not participate in the reaction. It was assumed that monodentate formate species, originating from monodentate carbonate adsorbed on medium–basic sites, could be hydrogenated more rapidly than bidentate formate species, typically formed from hydrogen carbonate. Panagiotopoulou et al. (Petala & Panagiotopoulou, 2018) reported the promotion effect of alkali metals in CO_2 methanation over the 0.5%Ru/TiO_2 catalyst with a Na loading amount of <0.4 wt. %. In particular, Na promoter can enhance the adsorption and dissociation of CO on the interfacial sites of Ru/metal-oxide, promoting conversion of CO_2 to CH_4.

Table V.3 *Peaks temperatures and quantitative results in the CO_2-TPD tests*

	Fresh Ni-catalyst	Spent Ni-catalyst	Fresh NiCa-catalyst	Spent NiCa-catalyst
Peaks Temperatures (°C)	85	89	84	83
	-	126	-	-
	175	146	150	176
	-	238	265	244
	-	-	352	303
	-	471	-	400
	487	498	-	447
	582	-	-	-
	623	-	-	-
	644	-	-	-
Total basicity (μmol·g^{-1}_{cat})	84	68	38	50
Basicity of medium basic sites (μmol·g^{-1}_{cat})	8.5	44.8	33	48.2

Overall, the CO_2-TPD results demonstrate that Ca significantly modifies and stabilizes the basic properties of the catalyst, promoting a surface enriched in medium basic sites that are particularly relevant for CO_2 adsorption and conversion pathways.

V.2.2 Powder catalyst characterization

The powder catalysts were first analyzed through SSA measurements. Since the support consisted of alumina obtained from washcoat drying, a high SSA value was expected. The support sample exhibited a surface area of 203 m^2/g (

Table V.**4**) which decrease to 55 m^2/g in the final catalyst. This reduction was expected due to the deposition of relevant quantity of active species. As shown in Figure V.11, the mesoporous structure of the alumina is preserved; however, the microporosity is reduced (Table V.4) as a consequence of species deposition.

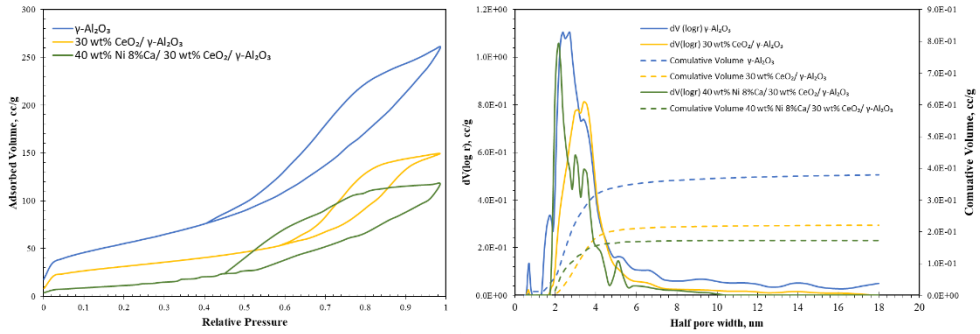


Figure V.11 *Isotherms and porous distribution of powder catalyst*

Table V.4 *SSA and porosity properties of powder catalyst*

	γ-Al_2O_3	**30%CeO_2/γ-Al_2O_3**	**40%Ni_8%Ca/30%CeO_2/γ-Al_2O_3**
SSA, m^2/g	203	108	55
Micropores diameter, nm	3.70	2.34	2.32
Micropore volume, mL/g	0.27	0.16	0.07
Mesopores diameter, nm	4.75	6.81	4.34
Mesopores volume, mL/g	0.38	0.22	0.17

Chapter VI.
Results and Discussion

VI.1 Results of the preliminary experimental tests

In the first stage of this PhD project, preliminary experiments were carried out to assess the influence of hydrogen in the reactant feed and to evaluate the effect of the catalyst on the resulting product distribution.

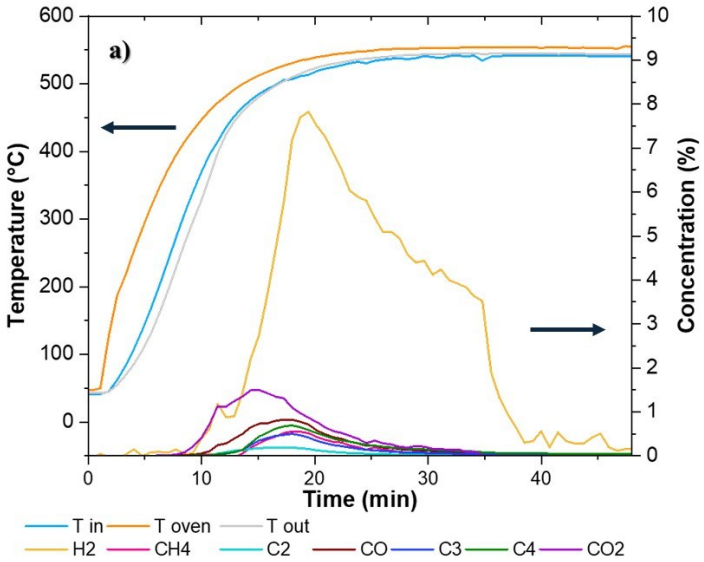
Due to the intrinsic complexity of the reaction system, a preliminary qualitative analysis was conducted as a first step toward its characterization. The results are shown in **Errore. L'origine riferimento non è stata trovata.**, for the following reaction system: pyrolysis, catalytic pyrolysis, hydrogasification and catalytic hydrogasification. The experimental tests were conducted in the configuration shown in Figure IV.5 in Chapter IV.

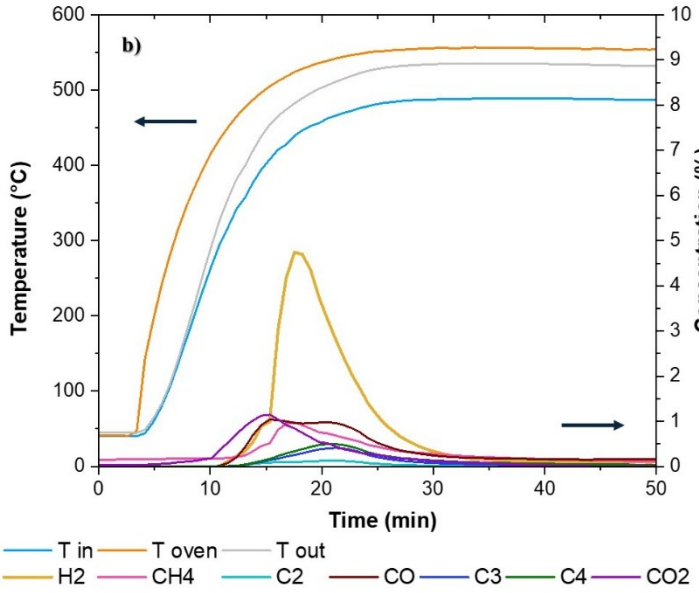
The main gaseous compounds product obtained during the heating of the plastic waste sample in an inert atmosphere are reported in Figure VI.1a. The first gases which leave the solid matrix are water and carbon dioxide starting from around 200°C, followed by carbon monoxide, methane and hydrocarbons with 2 (C2), 3 (C3) and 4 (C4) carbon atoms as the temperature increases. The decomposition of the solid mainly produces hydrogen, which can help in the hydrogenation of heavy hydrocarbons to short-chain gases (such as methane).

The addition of the catalyst (Figure VI.1b) increases the production of hydrogen and carbon monoxide; the curves of C2, C3, and C4 have the same trends of that in the pyrolysis test. No evidence on the role of the catalyst in the hydrogenation of C2, C3, and C4 into methane is given. The presence of hydrogen in the reaction stream enhances the formation of methane and carbon monoxide (Figure VI.1c).

The catalytic hydrogasification (Figure VI.1d) determines an increase in methane formation, proving the suitability of the Ni-catalyzed foam for the methanation of the pyrolysis gases. The hydrocarbons with a higher number of carbon atoms are still detected. This can be explained considering that the contact time between the gaseous volatiles and the catalyst is too low to obtain the decomposition of the hydrocarbon molecules into small ones. Indeed, the

curves reported are in accordance with the literature reaction mechanism, where the polymeric macromolecules undergo a series of dissociation steps up to methane. Furthermore, the small sample of plasmix used in these preliminary tests does not allow to report a significant production of methane, being the observed signals only a transient of a more complex process.





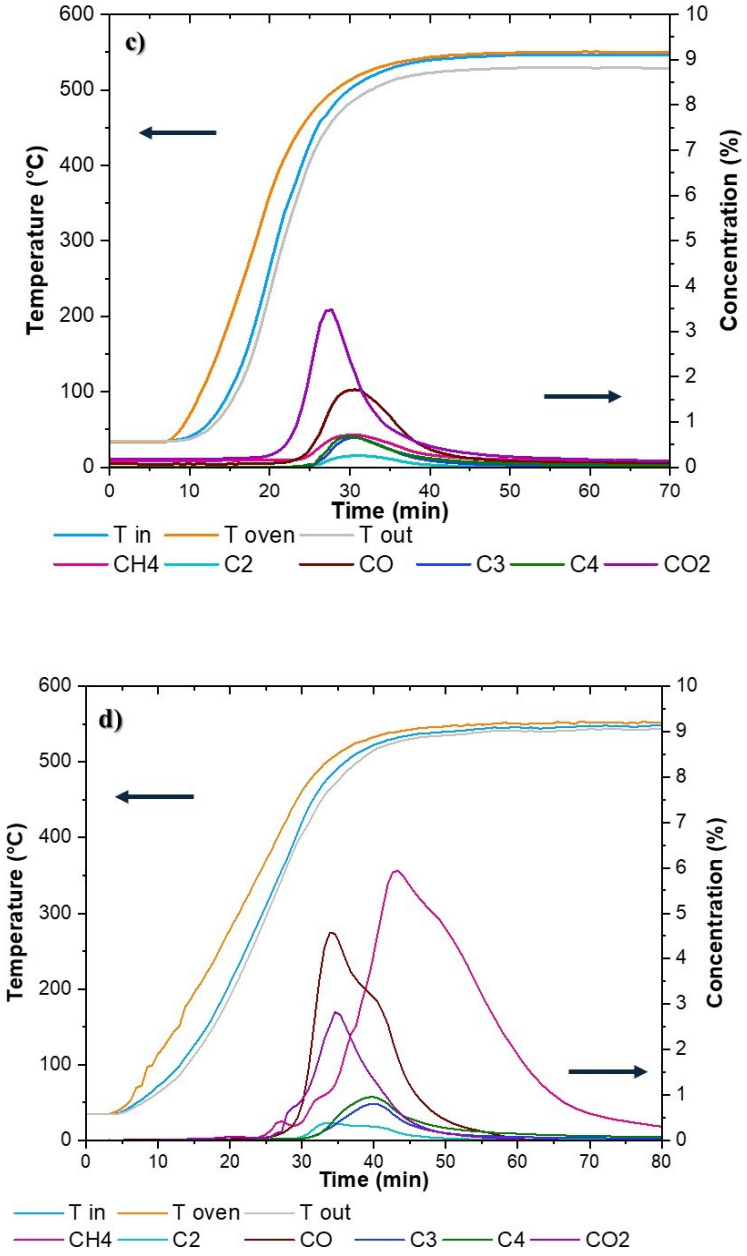


Figure VI.1 *Results of experimental test under (a) pyrolysis, (b) catalytic pyrolysis, (c) hydrogasification, and (d) catalytic hydrogasification conditions*

The evaluation of methane selectivity and other gaseous species was conducted to better assess the potential of catalyzed hydrogasification for methane production.

As shown in Figure VI.2, methane selectivity reached approximately 59% in the case of Ni-catalyzed hydrogasification, a significantly higher value compared to the other tests (6.7% for pyrolysis, 13.7% for catalyzed pyrolysis, and 7.8% for non-catalytic hydrogasification). These findings highlight the crucial role of the catalyst in steering the reaction pathway, as CO_2 remains the dominant product in both non-catalytic pyrolysis and hydrogasification.

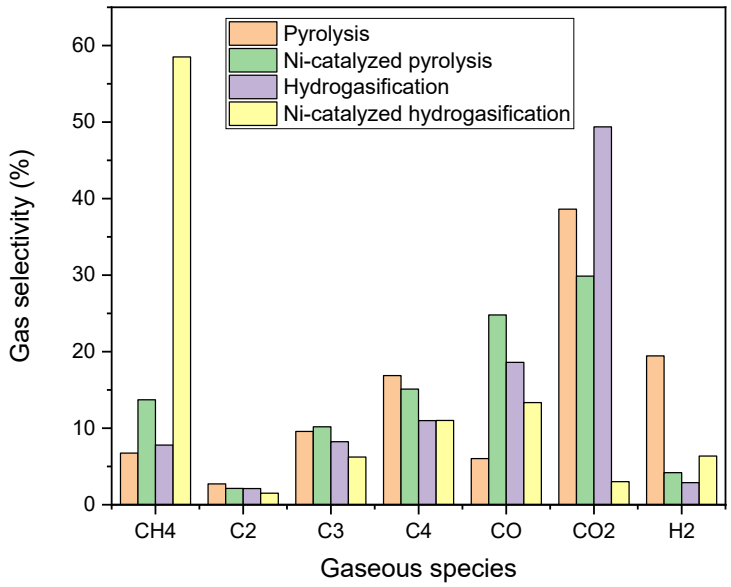


Figure VI.2 *Gas selectivity in the experimental test*

Gaseous species are not the only products of the reaction; solid and liquid residues can also be recovered from the plastic waste conversion. The liquid residue is collected in a trap located in the cooling bath after the reactor, while the solid residue, primarily ash and char, is retrieved directly from the reactor. The weights and corresponding percentages of these residues are provided in Table VI.1. The values demonstrate that the addition of the catalyst significantly improved plastic waste gasification. Furthermore, the catalyst facilitates the gasification of the liquid residue, driving the conversion of plastic waste into solid and gaseous products. Specifically, the liquid residue decreased to 5.50% in the case of Ni-catalyzed hydrogasification, while gas production rose to 76.45%.

Table VI.1 *Amount of the liquid and solid residues compared to the gaseous fraction*

Test	Solid, g	Liquid, g	Solid Yield, %	Liquid Yield, %	Gas Yield, %
Pyrolysis	0.243	0.58	11.70	36.50	51.80
Ni-catalyzed pyrolysis	0.347	0.46	17.35	23.00	59.65
Hydrogasification	0.085	0.745	4.25	37.25	58.50
Ni-catalyzed hydrogasification	0.361	0.11	18.05	5.50	76.45

VI.2 Scale-up of the reactor and optimization of the reactor configuration

Results of experimental tests performed in the reaction configuration shown in Figure IV.6 are discussed in this paragraph.

This configuration allows:

- the processing of a substantial amount of plastic-waste feed, as the reactor volume is approximately 2 L, corresponding to a scale-up factor of about 30 compared to the reactor used in the preliminary tests.
- It ensures physical and thermal separation between the plastic-waste zone and the catalytic-foam zone, thanks to the presence of the cordierite monolith.
- It provides thermally independent reaction zones, made possible by the use of separate metallic heating elements.

In such heterogeneous catalytic systems, a key challenge is that impurities present in plastic waste may deactivate the catalyst; moreover, the subsequent separation of the catalyst after reaction is considerably more demanding. Therefore, the literature indicates that the pyrolysis-catalysis system is typically divided into two stages: first, plastic is decomposed into primary volatiles at approximately 500 °C, which then pass through a catalytic reforming bed at a specified temperature. The advantages of using two independent reactors in series are clear when compared to the conventional one-step pyrolysis/gasification process.

VI.2.1 Preliminary heating test in the new reactor configuration

A preliminary heating test has been carried out by positioning the cordierite monolith within the reactor, at a middle position between the inlet and the outlet. Two thermocouples have been used to measure the temperatures in the inlet and outlet sections. The test has been performed with the following procedure: a flow of 200 NmL·min^{-1} of helium has been sent to the reactor; the upper zone of the reactor has been heated up with a ramp of 10°C·min^{-1} up to 550 °C with the metallic resistance R_1, using a PID controller; the temperatures of the two zones have been recorded with an acquisition interface developed in Labview environment. The trends of the temperatures are shown in Figure VI.3, from which it is evident that the cordierite monolith provides thermal insulation between the two zones of the reactor; indeed, the heating of the outlet section does not affect the temperature in the inlet section which remains at ambient temperature. This test proves that the cordierite monolith can thermally separate the two zones.

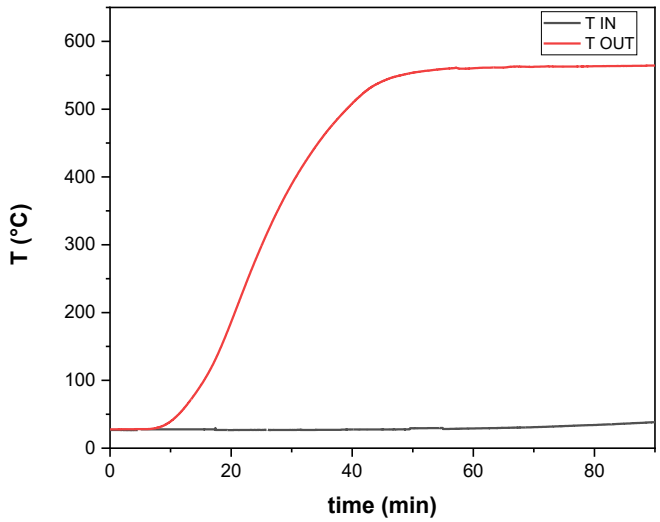


Figure VI.3 *Heating of the reactor with the cordierite monolith used for thermally insulate the two zones of the reactor*

Besides experimental assessment of thermal insulation properties of the monolith in cordierite, a simulation with COMSOL Multiphysics software was performed in order to determine the thermal gradient within the reactor and monolith.

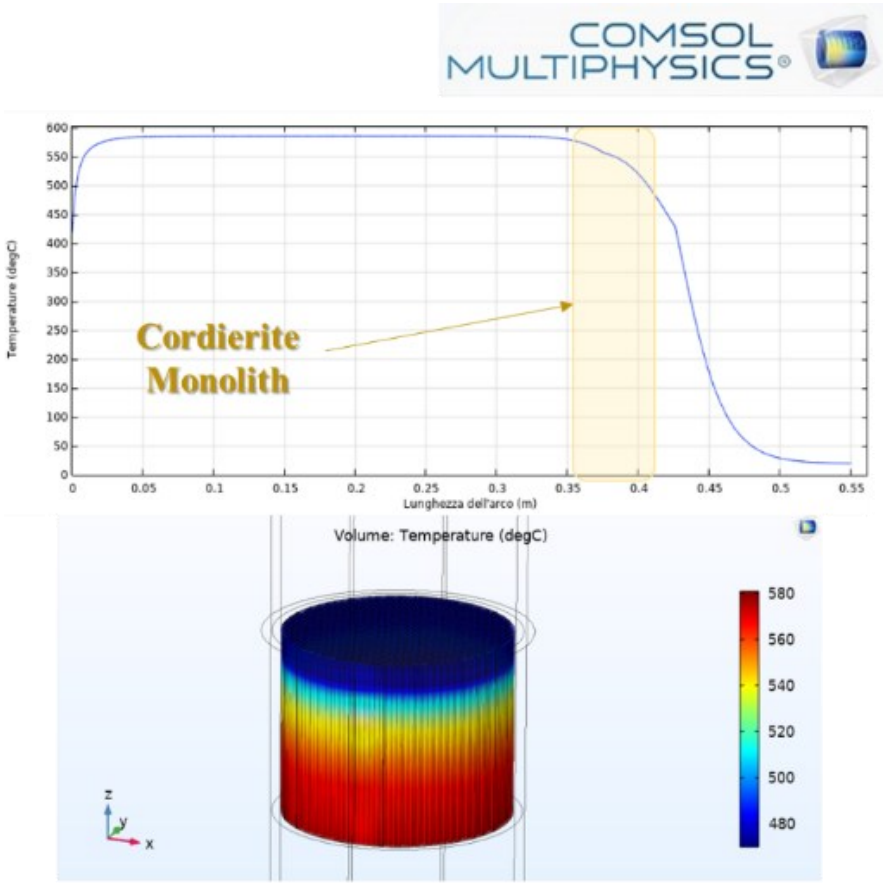


Figure VI.4 *COMSOL simulation of temperature profiles within cordierite monolith*

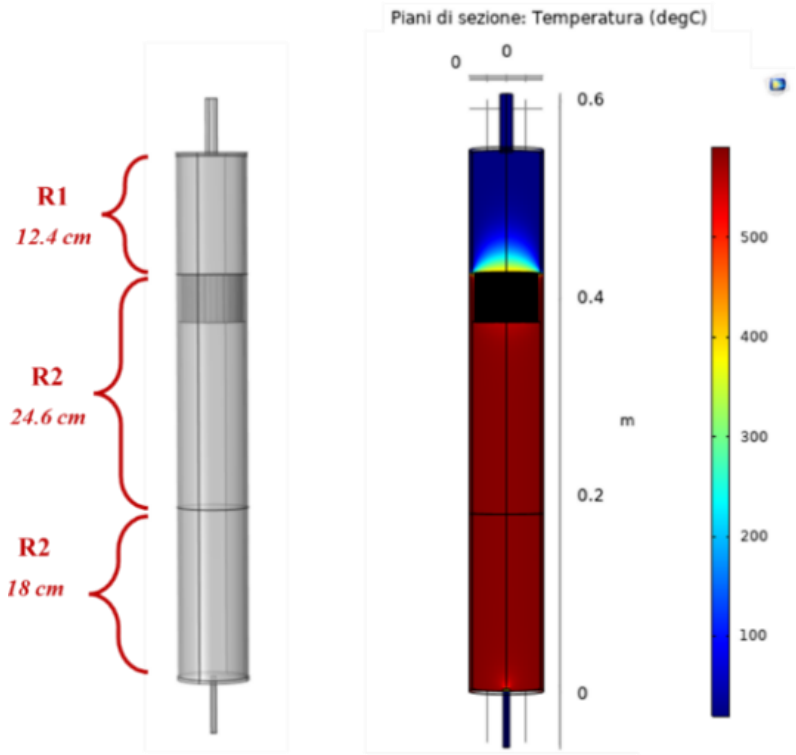


Figure VI.5 *COMSOL simulation of temperature profiles within the reactor*

Figure VI.4 and Figure VI.5 present the thermal simulation results obtained when the lower section of the reactor is heated to 600 °C. Under these conditions, the upper zone of the reactor remains largely unaffected by the heating, except for the region directly in contact with the hot monolith. The temperature distribution within the cordierite monolith reveals a gradual decrease from the heated base, reaching approximately 475 °C at the upper end. This gradient is primarily attributed to the fact that the upper zone of the reactor is initially at room temperature, which acts as a thermal sink during the transient phase. However, when the reactor operates under steady-state reaction conditions—namely, with the upper zone also maintained at 600 °C—the axial temperature gradient is expected to be significantly reduced, resulting in a more uniform thermal profile along the monolith's length. Despite this, radial gradients may still persist due to the low thermal conductivity of cordierite and the geometry of the system. These must be carefully evaluated to exclude the formation of localized hot or cold spots, which could negatively affect reaction selectivity and lead to the generation of undesired by-products.

VI.2.2 Results of structured catalyst activity test

After confirming that the reactor zones can be thermally isolated from the plastic waste bed, the catalyst was positioned inside the reactor to initiate the activation process. Specifically, five catalytic foams were employed and placed within the reactor, surrounded by a layer of glass wool to prevent reactant flow bypass and ensure uniform contact with the active surface.
The results of the tests are shown in Figure VI.6. The tests were performed using two different plastic waste weights (50 and 105 g), corresponding to two plastic waste-to-catalyst ratios. The catalyst used has the following formulation: 40 wt.% Ni/ 8 wt.% Ca/ 30 wt.% CeO_2/ 30 wt.% Al_2O_3 deposited on the OBSiC foams.

Once the catalytic foams were heated to 600 °C, the plastic feedstock was heated in the presence of a hydrogen-rich atmosphere (95% H_2 in He), triggering thermal depolymerization and the release of a gaseous mixture containing CO, CO_2, CH_4, C_2H_6 and C_3H_8. The presence of nickel-based catalysts played a crucial role in steering the reaction pathways toward hydrogenation, enhancing the conversion of unsaturated and oxygenated intermediates into saturated hydrocarbons. As the reaction progressed, a gradual shift in product distribution was observed, with methane becoming increasingly dominant. This trend reflects the progressive consumption of hydrogen, which acts both as a reactant in hydrogenation steps and as a carrier gas. The increase in CH_4 concentration is indicative of successful hydrogenation of CO and light olefins, which are typically formed in the early stages of plastic decomposition.

Comparing the two experimental runs—one with 50 g and the other with 105 g of plastic—it is evident that the amount of feedstock influences both the onset and extent of gas evolution. In the higher-load experiment, the gas composition exhibits a broader distribution of intermediates before converging toward methane-rich output (with a peak of 55 vol.% and a plateau of 47 vol.%). This suggests that the catalyst maintains activity even under increased organic load, although transient accumulation of higher carbon atoms compounds and CO may occur due to the depolymerization of plastic.

Overall, the data confirm that under hydrogen-rich conditions and with sufficient thermal input, the catalytic foams effectively promote the transformation of plastic-derived volatiles into stable, reduced products. The evolution of gas composition over time highlights the interplay between thermal cracking, catalytic hydrogenation, and feedstock availability, all of which must be considered when optimizing reactor performance and product selectivity.

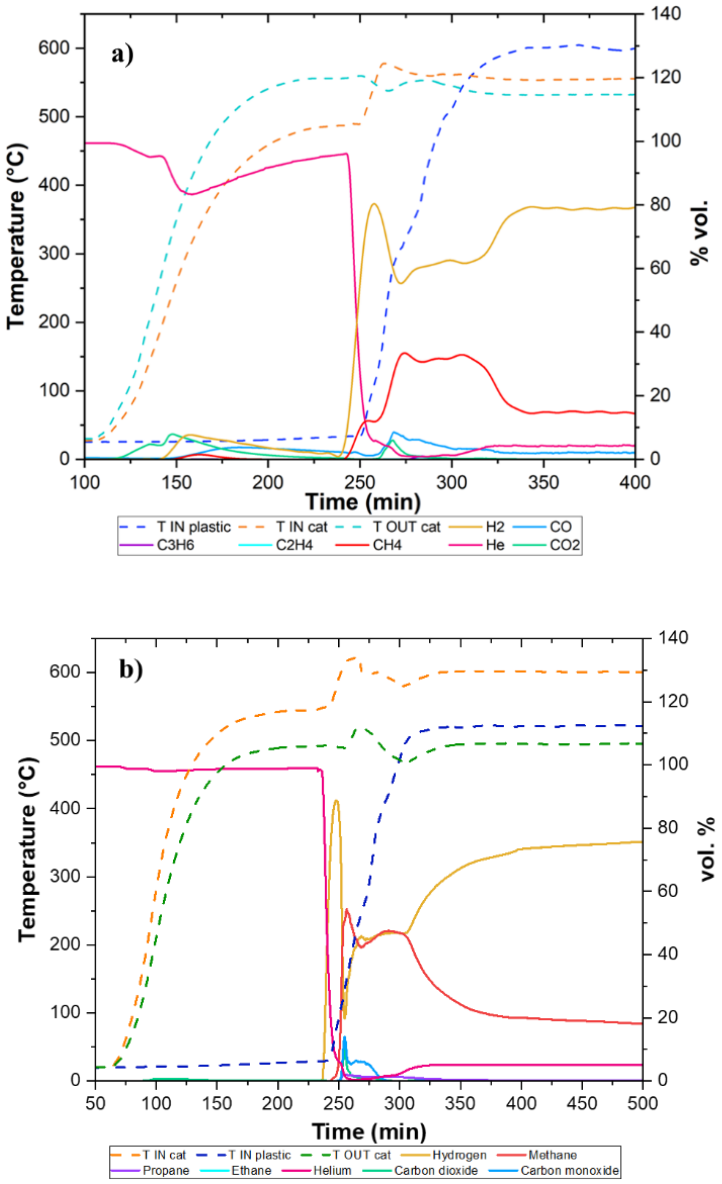


Figure VI.6 *Results of experimental test with a) 50 g and b) 105 g of plastic waste*

Figure VI.7 shows the curve of methane formation in the test where 105 g of plastic waste has been processed. Looking at the first hour of the reaction, the methane concentration sharply reaches the 55 vol.% peak within the first 10 minutes and sustains the production in the remaining 50 minutes.

This indicates that methane formation becomes dominant almost immediately after the reaction starts. Such a rapid increase suggests that the catalytic system enters a highly active regime from the outset, with fast kinetics governing the hydrogenation and cracking pathways. In this early stage, the catalyst surface is fully accessible, hydrogen is readily available, and the volatile species released from the plastic waste are quickly converted into methane. The rapid establishment of high CH_4 level highlights the strong methanation capability of the catalyst under the operating conditions employed.

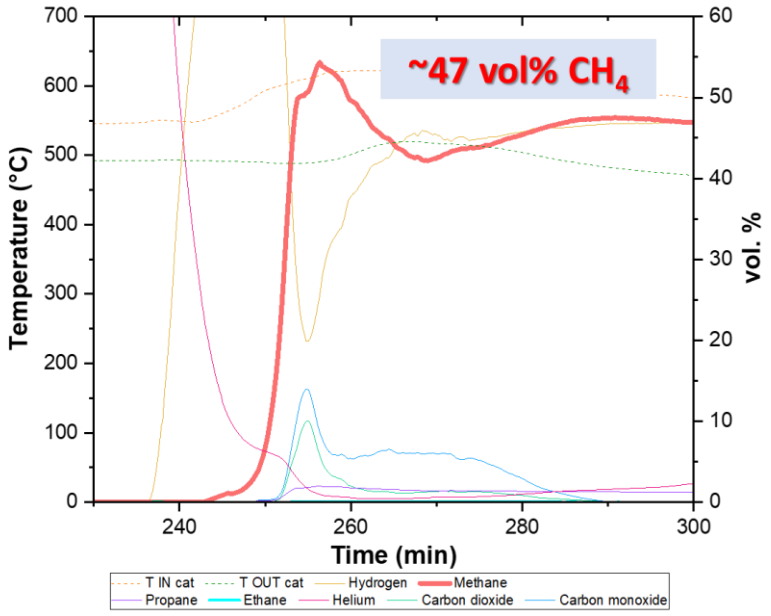


Figure VI.7 *Details of the results of the test with 105 g of plastic waste*

The parameters calculated for the efficiency assessment of the process are reported in Table VI.2.

Table VI.2 *Parameters for the assessment of process efficiency*

Plastic/catalyst ratio	α, kgH_2/ton plastic waste	κ, Nm^3gas/ton plastic waste	β, Nm^3 CH_4/ton plastic waste
1.5	16	454	405
0.7	22	490	411

The results indicate that the total gas production reaches about 500 $Nm^3_{gas}\cdot ton^{-1}_{\ plastic\ waste}$, and methane is the main product, accounting for approximately 84-89% of the total gas, which is much higher with respect to the methane yield in conventional plastic gasification/pyrolysis systems currently employed. The results reported in the table demonstrate that the two tests exhibit a high degree of reproducibility. When the gas production is normalized per ton of processed plastic waste, the values of κ and β remain remarkably similar across the two plastic-to-catalyst ratios. This consistency is particularly significant considering the strong heterogeneity of the plastic feedstock, which would normally be expected to introduce substantial variability in the process performance. The comparable gas and methane yields therefore indicate that the system operates in a robust and reproducible manner, despite fluctuations in feed composition.

The quantified gas yield and product distribution confirm effective carbon valorization, in agreement with the carbon conversion and gas yield KPI defined in Chapter IV.

Notably, the hydrogen consumption per ton of plastic is higher at the lower plastic-to-catalyst ratio (22 vs 16 $kg_{H2}\cdot ton^{-1}$), suggesting more intensive hydrogenation per unit feed despite the lower overall gas yield.

The higher plastic/catalyst ratio likely favours rapid thermal cracking and devolatilization, generating a larger quantity of reactive intermediates that are efficiently converted to methane via surface hydrogenation on Ni active sites (Figure VI.6). In contrast, at lower plastic loadings, the catalyst is less saturated and more available for deeper hydrogenation, leading to higher H_2 consumption per unit of plastic but a lower overall gas volume. This behavior reflects a shift from a cracking-dominated regime to a hydrogenation-limited regime, where the extent of conversion is governed by the balance between feedstock availability, active site coverage, and hydrogen partial pressure.

VI.2.3 Solid products characterization and catalyst regeneration

At the end of the experimental run, the catalytic foams were extracted from the reactor and visually inspected. A distinct layer of carbonaceous deposits was observed on the surface of the foams (Figure VI.8), indicating the formation of coke during the process. This suggests that, despite the hydrogen-rich atmosphere and the presence of active nickel sites, certain intermediates—likely unsaturated hydrocarbons or aromatics—underwent polymerization or condensation reactions leading to coke accumulation, (Khabib et al., 2014; Ochoa et al., 2020). On the contrary, hydrogen enriched atmosphere avoids the gasification of the deposited coke.



Figure VI.8 *Coke layer deposited over the catalytic foams*

Even though the presence of calcium improves the basicity of the catalyst and theoretically reduces the coke formation, coke deposition is inevitable in this kind of process. In the reaction conditions, this coke could react with the hydrogen and produce methane. This could explain the extended plateau in both the test reported in Figure VI.6 (at 15 vol.% and 20 vol.% for the test with 50 g and 105 g of plastic waste, respectively).

Raman analysis on coke sample is shown in Figure VI.9. The band at 1390 and 1605 cm^{-1} are assigned to so-called G and D peaks, which are due to sp^2 carbon species. The G peak is due to the bond stretching of all pairs of sp^2 atoms in both rings and chains, and the D peak is due to the breathing modes of sp^2 atoms in rings. These two peaks are common for various forms of disordered, non-crystalline, and amorphous carbons in the Raman spectra. The I(D)/I(G) ratio is 1.87 and indicates that the coke deposited on the catalyst exhibits a high degree of structural disorder, characteristic of amorphous or highly fragmented carbon. This suggests that coke formation is primarily driven by polymerization and condensation reactions rather than the deposition of well-organized graphitic structures (He et al., 2010).

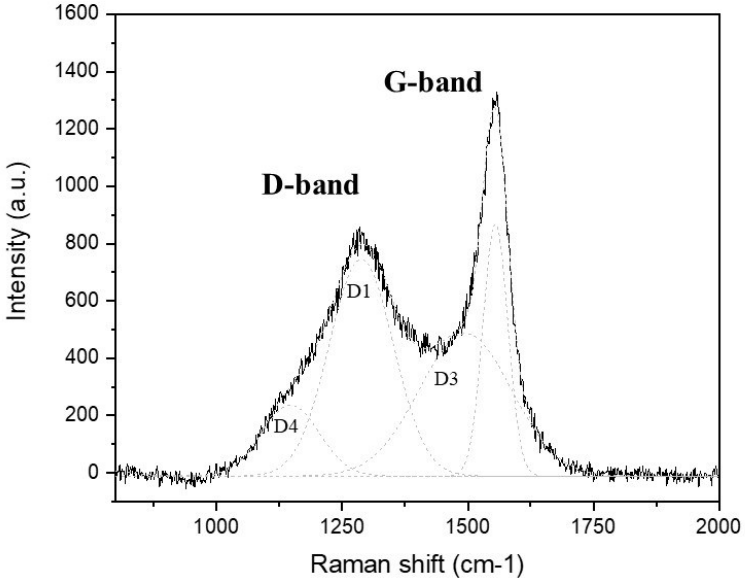


Figure VI.9 *Raman analysis results on coke deposited on the catalytic foams*

The foams were regenerated by means of oxidation in air of the coke deposited, and characterization of the regenerated catalyst was carried out.

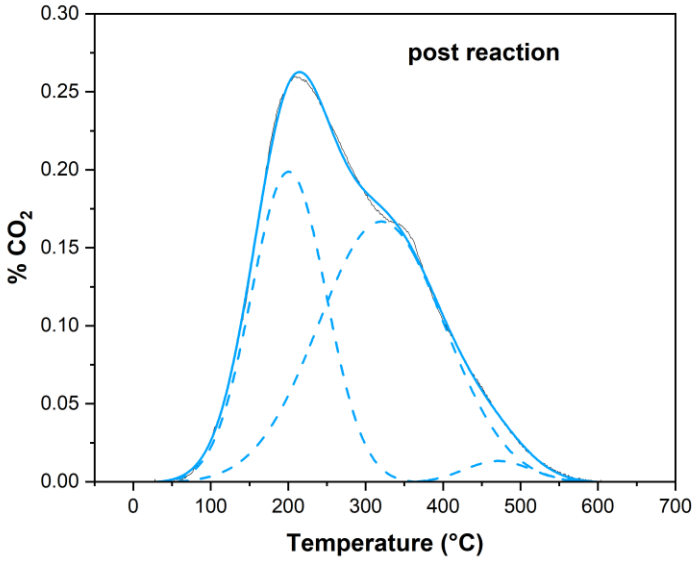


Figure VI.**10** compares the temperature-programmed reduction (TPR) profiles of the catalyst on the fresh catalyst (red curve) and after reaction on the regenerated catalyst (blue curve). The regenerated catalyst shows a clear shift of the reduction peaks toward higher temperatures, suggesting a decrease in overall reducibility. This behavior is likely due to structural changes induced during the reaction and subsequent oxidation treatment, such as stronger metal–support interactions, partial sintering of Ni particles, or formation of more stable Ni–O–Ce or Ni–O–Ca phases. These modifications can hinder hydrogen uptake and delay the reduction of NiO, reflecting a more robust but less reactive surface environment.

The values of H_2 uptake have shown that about 26% of the NiO was lost after the disruption of some of the foam due to the coke formation.

The CO_2-TPD curve does not disclose a significant modification in the basicity properties of the regenerated catalyst, since the medium sites are still predominant compared to the others.

The preserved activity of the regenerated catalytic foams suggests that they are suitable for repeated use under the same reaction conditions, provided that intermediate regeneration steps are applied to mitigate coke accumulation and extend operational lifetime.

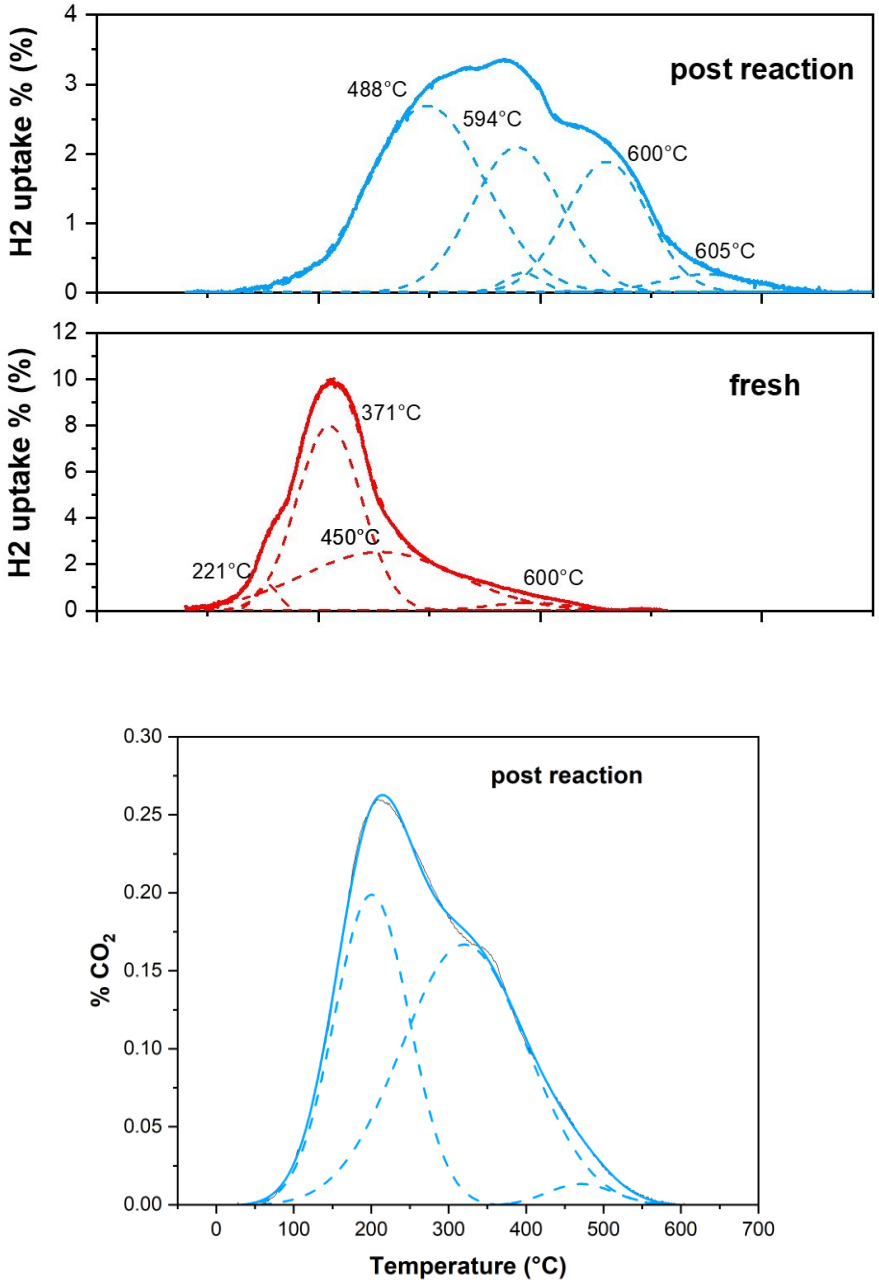


Figure VI.10 *TPR and CO_2-TPD on regenerated catalyst*

VI.2.4 Results on the regenerated catalyst

The regenerated catalytic foams were used in an additional test to process a new batch of 30 g of plastic waste feed, to evaluate the activity of the regenerated catalyst. Assessing its performance after regeneration is essential to determine whether the catalyst undergoes deactivation during the hydrogasification process. The results are reported in Figure VI.11.

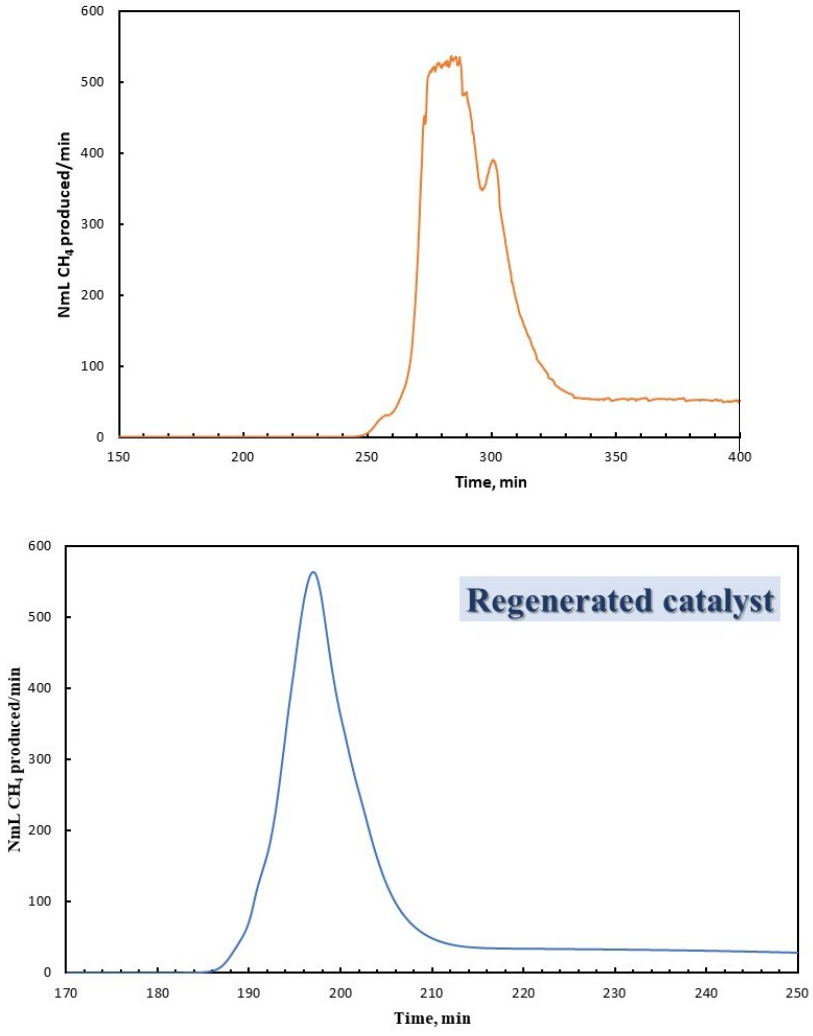


Figure VI.11 *Methane production in NmL·min^{-1} for the fresh and spent catalyst*

The methane production profiles obtained with the fresh and regenerated catalysts show a remarkably similar kinetic behaviour, indicating that the catalyst retains a high level of activity after regeneration. In both cases, the CH_4 formation rate exhibits a sharp increase shortly after the onset of the reaction, reaching peak values in the range of 500–570 $NmL \cdot min^{-1}$. Moreover, the values of methane production normalized per ton of plastics and grams of active phase are relatively close (55 for the fresh catalyst and 51 $Nm^3_{CH4} \cdot ton_{plastic}^{-1} \cdot g_{cat}^{-1}$ for the regenerated), which reinforces the conclusion that the catalyst preserves its functional performance after regeneration.

This rapid rise reflects the strong intrinsic activity of the catalytic foam toward methanation, as well as the efficient conversion of the volatile species released from the plastic waste.

The regenerated catalyst displays a peak that is comparable in magnitude to that of the fresh material, confirming that the regeneration procedure effectively restores the active surface. This suggests that no significant deactivation occurred during the previous hydrogasification test, and that the catalyst maintains its functional integrity and reactivity after regeneration.

This behaviour is fully consistent with the TPR analysis. The regenerated catalyst exhibits a reduction profile that closely resembles that of the fresh material, with only minor shifts in peak position and intensity. Such similarity confirms that the regeneration procedure effectively restores the reducible Ni species and re-establishes the active metallic phase responsible for methanation. The absence of significant changes in the TPR features suggests that no substantial sintering or irreversible structural modification occurred during the previous reaction cycle.

Overall, the close similarity between the two methane production profiles demonstrates both the robustness of the catalytic system and the effectiveness of the regeneration step, supporting the suitability of the catalyst for repeated hydrogasification cycles.

The recovery of methane production after regeneration, together with the preserved reducibility profile, demonstrates compliance with the catalyst stability and regenerability KPI defined in Chapter IV.

VI.3 Mechanistic interpretation of the Ni–Ca/CeO_2/γ-Al_2O_3/OBSiC structured catalyst in Hydrogasification of plastic waste

The catalytic behaviour observed in the discussed results can be rationalized by considering the hierarchical architecture of the structured catalyst and the synergistic interactions among its individual components. The OBSiC foam, the γ-Al_2O_3 and CeO_2 interlayers, and the Ni–Ca active phase each contribute distinct physicochemical functions that collectively determine the activity, selectivity, and stability of the system during hydrogasification.

The OBSiC support provides the mechanical robustness and thermal conductivity required for moderate-temperature hydrogasification. Its open-cell structure ensures efficient heat transfer and minimizes temperature gradients within the reactor, thereby preventing local hot spots that could promote Ni sintering or uncontrolled carbon deposition as reported for SiC-based structured supports in high-temperature catalytic processes (Balzarotti et al., 2022). Moreover, the chemical inertness of OBSiC avoids parasitic reactions and provides a stable macroscopic scaffold for the subsequent functional layers.

The γ-Al_2O_3 layer deposited on the foam plays a crucial role in increasing the accessible surface area and providing anchoring sites for the CeO_2 and Ni–Ca phases. Its moderate acidity facilitates the adsorption and activation of oxygenated functionalities released from the carbonaceous feedstock, promoting their subsequent hydrogenation. At the same time, γ-Al_2O_3 contributes to the dispersion of the active phase by preventing the migration and coalescence of Ni nanoparticles (Bartholomew, 2001).

The CeO_2 interlayer introduces an additional level of functionality through its well-known redox behaviour. The Ce^{4+}/Ce^{3+} couple provides mobile oxygen species capable of participating in the activation of carbonaceous intermediates, particularly at the metal–support interface. This redox flexibility enhances the removal of surface carbon species that would otherwise accumulate on Ni, thereby maintaining the availability of active sites. Furthermore, CeO_2 establishes strong metal–support interactions that stabilize Ni nanoparticles against sintering, especially under the reducing and high-temperature conditions typical of hydrogasification. The presence of CeO_2 therefore contributes both to the intrinsic activity of the catalyst and to its long-term durability (X. Yan et al., 2019) .

The Ni phase remains the primary site for H_2 dissociation and hydrogen spillover, which are essential steps in the hydrogasification mechanism. Ni facilitates the formation of reactive hydrogen species that migrate to the carbon surface, enabling the hydrogenation of carbonaceous fragments and the formation of methane. The cyclic carburization–decarburization behaviour of Ni, often observed in carbon–hydrogen systems, plays a central role in sustaining the reaction. The formation of transient Ni–C and Ni–(O)–C species is consistent with the enhanced reactivity observed experimentally and aligns with mechanistic models reported in the literature (Haga et al., 1992) (Jiang et al., 2017).

Calcium acts as a powerful promoter, influencing both the structure and the reactivity of the Ni phase. During heating under H_2, calcium nitrates or acetates form CaO(COO) intermediates that decompose above 550 °C into CaO and CO_2 as originally reported by (Haga & Nishiyama, 1987). The CO_2 released in situ can be captured by Ni–C structures, forming Ni–(O)–C species that enhance Ni dispersion and facilitate the activation of carbon. This mechanism, previously proposed by Haga, Jiang, and others, is consistent with

the improved methane yields and higher carbon conversion observed in this work. In addition, CaO migrates toward the char surface during reaction, where it suppresses Ni sintering, mitigates catalyst poisoning, and promotes the activation of low-reactivity carbon domains such as graphite and amorphous carbon. These effects are particularly relevant for the structured catalyst investigated here, where the hierarchical arrangement of layers allows CaO to interact efficiently with both the Ni phase and the carbonaceous substrate.

The experimental results presented in Chapter VI reflect the combined action of these mechanisms. The enhanced methane production, the higher conversion of carbon, and the improved stability of the catalyst can be attributed to the cooperative behaviour of the OBSiC support, the γ-Al_2O_3 and CeO_2 interlayers, and the Ni–Ca active phase. The structured architecture ensures optimal heat and mass transfer, while the chemical functionalities of the individual layers contribute to the activation of hydrogen, the stabilization of Ni, the activation of carbon, and the mitigation of deactivation pathways.

Overall, the catalytic performance of the Ni–Ca system supported on OBSiC arises from a complex but coherent interplay of structural and chemical factors. The mechanistic interpretation provided here strengthens the discussion of the experimental results and highlights the importance of the hierarchical catalyst design in enabling efficient hydrogasification of carbonaceous materials.

VI.4 Results of fluidization experiments

This paragraph presents the experimental activities related to the fluidization tests conducted during the period abroad at the University of Zaragoza.

Alumina powder was sieved into distinct granulometric fractions (45-90 μm, 90-180 μm, 180-250 μm, 250-355 μm) and subjected to multiple fluidization cycles, each lasting several hours. After each cycle, the amount of solid retained within the target size range was measured to assess potential particle fragmentation. This procedure aimed to evaluate the mechanical stability of the powder under fluidization conditions and determine its suitability for use in fluidized bed reactors.

Figure VI.12a shows the weight loss of 90-180 μm alumina particle sample after prolonged fluidization. The majority of the material consistently remains within the selected size range even after repeated fluidization steps. This indicates that the alumina powder exhibits good mechanical resistance to attrition and fragmentation under dynamic gas–solid contact, making it a suitable candidate for long-term operation in fluidized systems without significant loss of granulometric integrity.

Minimum fluidization velocities were measured for the distinct alumina sieve fractions to quantify the impact of granulometry on fluidization behavior (Figure VI.12b). As expected for fluidized systems, the pressure drop increase with gas velocity in the fixed-bed regime and reaches a plateau once the minimum fluidization velocity is attained. Clear differences emerge among the various granulometries: finer particles (45–90 μm) exhibit higher pressure drops and achieve fluidization at lower gas velocities, reflecting their lower terminal velocity and better fluid dynamic responsiveness. Conversely, coarser particles (250–355 μm) show lower pressure drops and require significantly higher gas velocities to reach the fluidization plateau, consistent with their higher density–diameter product and reduced mobility within the bed.

Overall, the pressure-drops curves confirm the strong influence of particle size on the hydrodynamic behaviour of the alumina powders. Smaller particles fluidize more easily and display more pronounced pressure-drop transitions, whereas larger particles behave more like a packed bed over a wider velocity range.

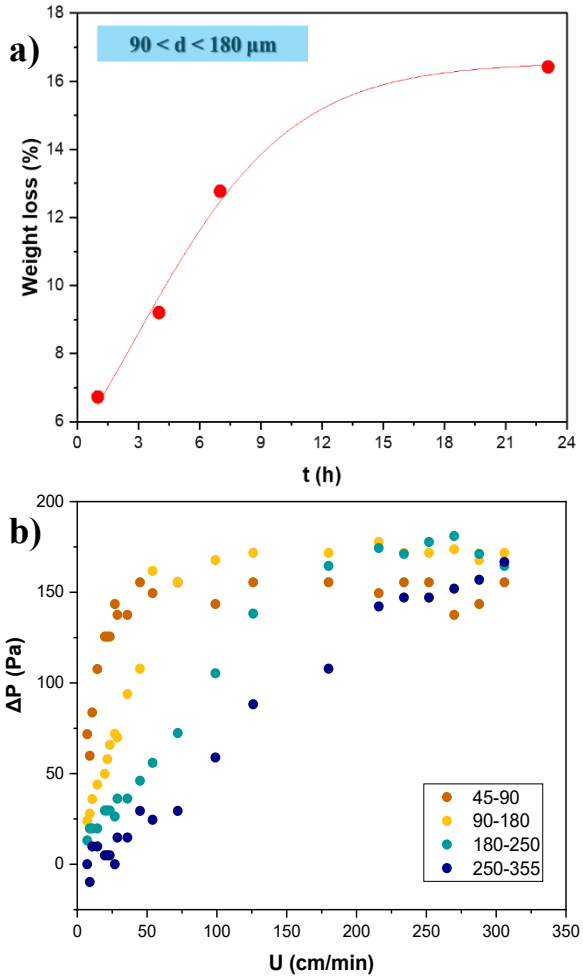


Figure VI.12 *a) Weight loss of 90-180 µm alumina particle sample after prolonged fluidization; b) Pressure drops curves for different granulometries of alumina powder*

Figure VI.13 compares the experimental data for minimum fluidization velocity with several literature models and the correlation developed in this work.

The proposed model (eq. (63)) shows excellent agreement with the experimental points across the tested Archimedes range, outperforming classical correlations such as those by Geldart & Abrahamsen, Chitester et al., and Barbosa. This suggests that the derived correlation better captures the

fluidization behavior of alumina powders under the specific operating conditions and particle characteristics of this study.

$$Re_{mf} = [2.6337^2 + 0.0076 \cdot Ar]^{1/2} + 2.6337 \quad (63)$$

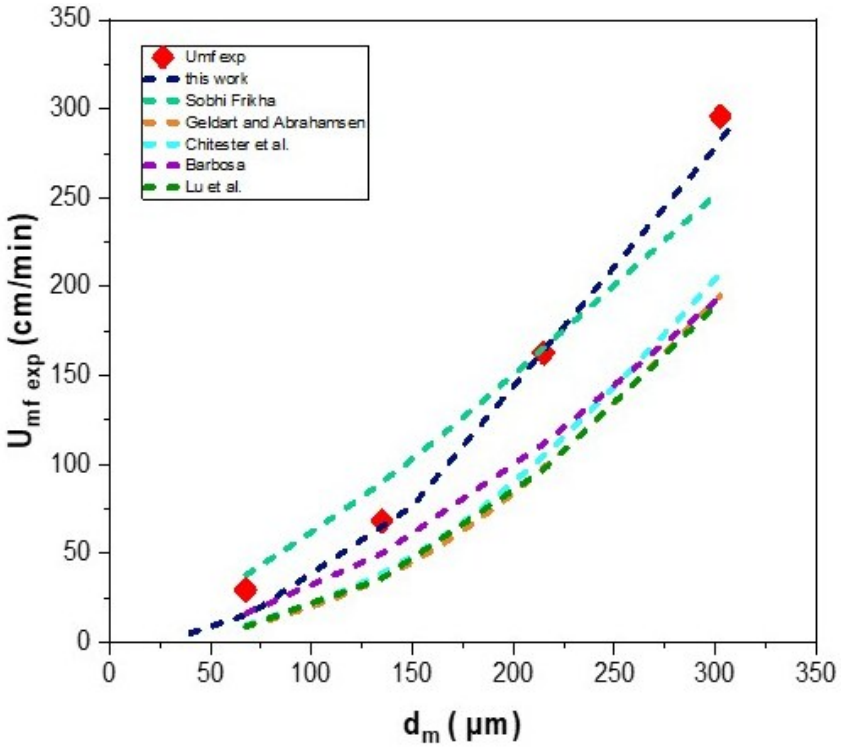


Figure VI.13 *Model for the prediction of minimum fluidization velocity of alumina powder and fitting of experimental data with literature models*

Deviation in the values of constants C_1 and C_2 from those reported in literature correlations highlights the need for a tailored equation that reflects the specific conditions of this study. The model proposed herein shows superior agreement with the experimental U_{mf} values and more accurately captures the influence of particle morphology.

Once the characterization of the alumina solid of different granulometry was finalized, experiments on the plastic waste were carried out. The peculiar size and shape of these particles, along with the low apparent density, have determined deficiencies in fluidization. This behavior is primarily attributed to the particles' tendency to form bridges and interlock, which—combined with strong interparticle forces such as adhesion and cohesion—prevents the bed from expanding and keeps it in a compacted state (Pérez et al., 2018). This phenomenon led to the formation of cohesive particle networks that ascended in plug flow as the superficial air velocity increased up to a threshold value.

Despite the application of higher gas velocities and external energy inputs intended to overcome interparticle cohesion, these networks remained intact, preventing the onset of fluidization. The entire bed behaved as a single, rigid entity. Eventually, the particles began to reorganize, reconnect, and interlace once more, further inhibiting any possibility of achieving fluidization. The main causes of fluidization difficulties can be attributed to the generation of electrostatic charges and particle interlacing induced by the fluidizing gas, which promote the formation of preferential flow channels and enhance interparticle forces. Additionally, the complex geometric morphology of the particles, their high aspect ratio (length-to-diameter), and low apparent density contribute to gas leakage through void regions, resulting in elevated bed porosity. As the air flow increases, these conditions favour the onset of plug flow (slugging), whereby particles move in cohesive blocks rather than fluidizing individually. This behavior closely resembles that reported by Reina et al. (Reina et al., 2000), who investigated low-density wood particles, by Zhong et al. (Zhong et al., 2008), who studied the fluidization of corn and cotton stalk particles, and by (Pérez et al., 2018), who studied the fluidization of sugarcane bagasse. Moreover, Pérez et al. (Pérez et al., 2018) demonstrated that even though bagasse "*in nature*" is not able to be fluidized itself, diminishing its size or granulometry to an adequate range, the biomass can be fluidized without adding inert material.

Assessed that the plastic waste cannot be fluidized, experiments of mixtures of alumina and plastic waste have been carried out.

The fluid-dynamic behavior of these mixtures is different from that of the single plastic waste particles. When gas was flowed through the tube, a significant expansion of the bed was observed, firstly, and then the increase in the superficial velocity of nitrogen induced the formation of the first bubbles and a small quantity of fluidized particles near the surface of the bed, while the remaining part of the bed was inactive. When velocity increases, pressure drops increase and bubbles rise in number and frequency. The plastic waste tends to detach itself from the wake created by the upward movement, entering a regime of fluidization when the pressure drop remains almost constant, defining the state where the whole bed is fluidized.

The first fluidization tests of a plastic–alumina mixture were carried out using alumina particles in the 90–180 μm size range and plastic waste in the 180–355 μm range. Experiments were performed at various alumina-to-plastic volume ratios, specifically 1.00, 1.25, 1.50, 1.75, 2.00, and 2.25, to evaluate the fluidization behavior and identify the optimal mixing conditions. Figure VI.14 shows that the minimum fluidization velocity decreases with the volume ratio, as expected. Only a slight variation can be observed when the ratio is varied from 2 to 2.25 Table VI.3.

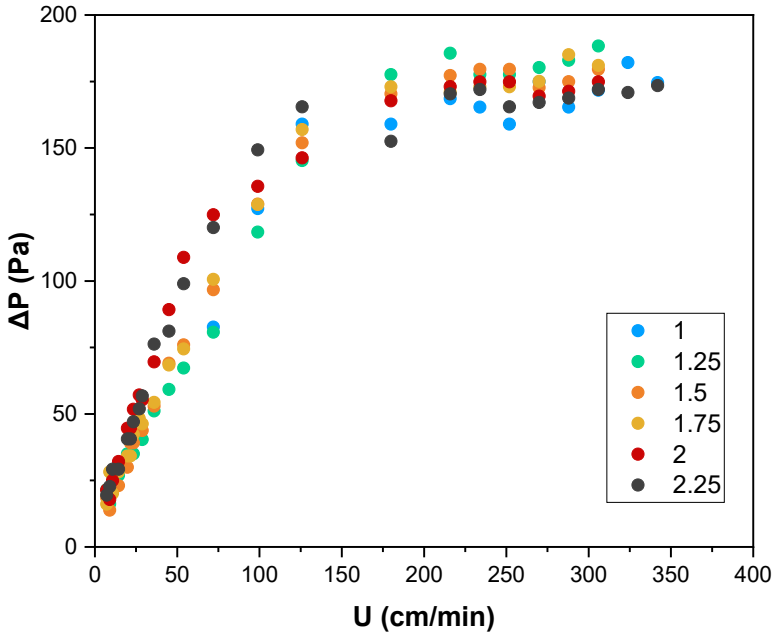


Figure VI.14 *Pressure drops curves of mixtures of alumina (90-180 µm) and plastic waste (180-355 µm)*

Table VI.3 *Experimental minimum fluidization velocity and dimensionless parameters for different volume ratios of alumina (90-180 µm) and plastic waste (180-355 µm)*

volume ratio alumina/ plastic waste	Umf, cm/min	Remf	Ar
0	66	0.101	67.01
2.25	91	0.159	85.31
2	116	0.205	88.57
1.75	124	0.222	89.71
1.5	126	0.231	92.18
1.25	144	0.272	95.26
1	141	0.273	99.71

The results of the prediction of the minimum fluidization velocity using different existing correlations in literature are shown in Figure VI.15.

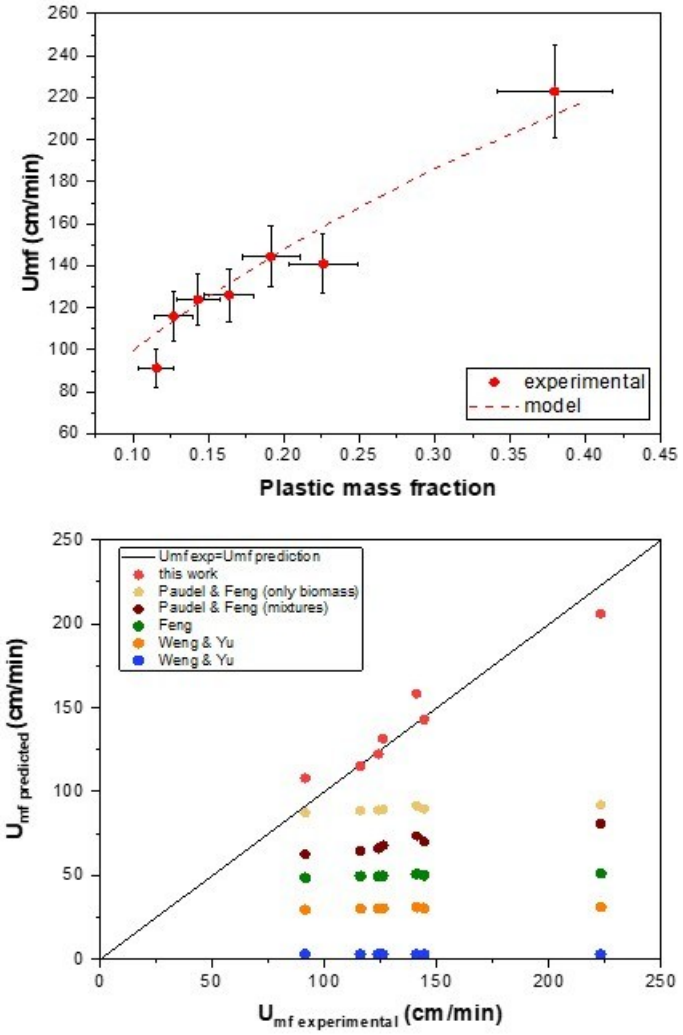


Figure VI.15 *Prediction of minimum fluidization velocity of mixtures for different volume ratios of alumina (90-180 µm) and plastic waste (180-355) µm*

The fitting of experimental data has been obtained with the following equation (eq. (64)):

$$Re_{mf} = \left[2160^2 + \left(2 \cdot (1 - x_p) + 24 \cdot x_p^{\frac{1}{2}}\right) \cdot Ar\right]^{1/2} - 24 \qquad (64)$$

Where the constants were optimized to the value C_1=2160, C_2=2 and C_3=24.

The discrepancies observed between the values predicted by literature-based correlations and those obtained experimentally can be attributed to the origin and characteristics of the particles used in developing such models. Most existing correlations were derived from mineral particles exhibiting well-defined geometries and operating conditions—namely, narrow size distributions, high sphericity, and predictable bed porosity—under which the influence of interparticle forces, crucial to fluidization behavior, was largely neglected. Consequently, when these correlations are applied to particles with irregular shapes, broad size distributions, high fines content, and low bulk densities—features that favour bridging and entanglement—the simulated outcomes deviate significantly from experimental reality, as exemplified by plastic waste.

Even for correlations specifically developed for biomass particles, discrepancies may arise due to the limited applicability of these models. They were typically formulated using particles within a narrow diameter range and possessing physical properties—such as density, sphericity, and aspect ratio—that differ significantly from those of plastic waste. These parameters strongly affect bed porosity and, in turn, influence the determination of the minimum fluidization velocity (U_{mf}), thereby limiting the predictive accuracy of such correlations when applied to heterogeneous biomass systems.

The effect of the dimension of plastic waste particles on the minimum fluidization velocity of the mixtures is shown in Figure VI.16.

The mean particle size of the plastic waste significantly influences the minimum fluidization velocity as it increases with the average diameter of the particles. This is ascribed to the low density of plastic waste, composed of particles with a high tendency to bond due to electrostatic forces. When the diameter increases, the aspect ratio rises, having an unfavourable effect on fluidization quality, requiring a higher superficial nitrogen velocity to fluidize particles with a larger diameter. This agrees with the findings in Zhong et al. (Zhong et al., 2008) investigation on cotton stalk and corn stalk and in Pérez et al. (Pérez et al., 2018) investigation with sugarcane bagasse.

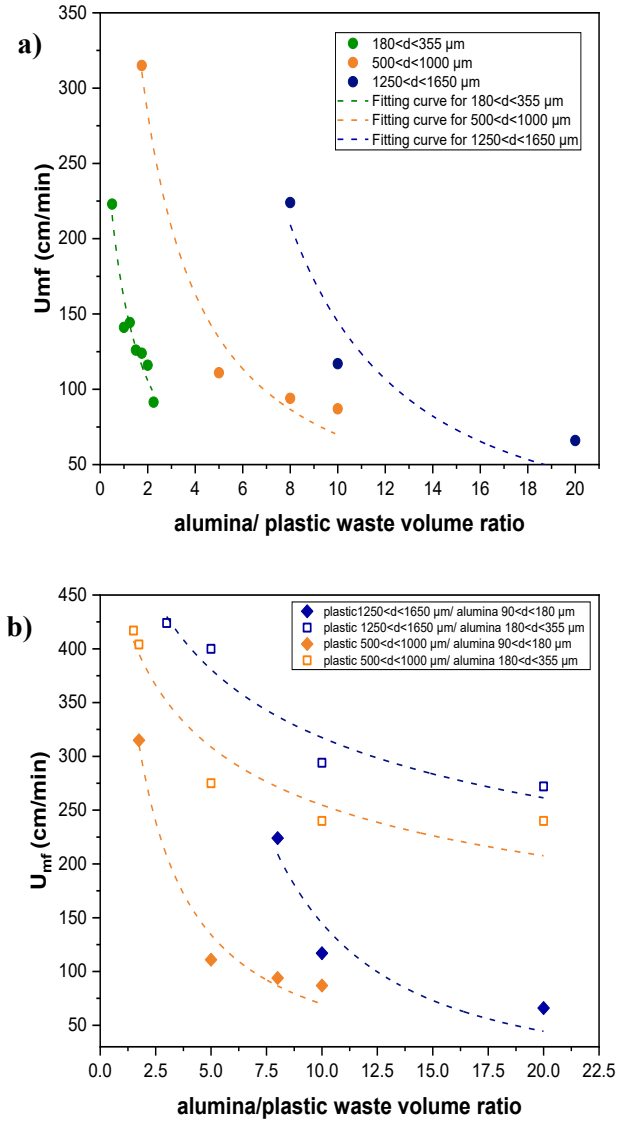


Figure VI.16 *Effect of the dimension of plastic waste particles on minimum fluidization velocity in mixtures of a) 90-180 µm alumina and b) 180-355 µm and at different ratio*

At a fixed alumina particle size, U_{mf} decreases as the alumina-to-plastic volume ratio increases, regardless of the plastic granulometry. Moreover, for finer plastic fractions, the target U_{mf} is reached at lower alumina/plastic ratios,

indicating that smaller plastic particles facilitate fluidization. Notably, fluidization occurs more readily when the particle size distributions of the two solids are more similar, suggesting that size compatibility enhances bed homogeneity and reduces segregation effects.

Finally, the fluidization behavior of a ternary mixture consisting of alumina, plastic waste, and coke was investigated to simulate reaction conditions (

Figure VI.**17**). The experiments were conducted by maintaining a constant weight of alumina while varying the amounts of plastic waste and coke, in order to emulate progressive plastic degradation and coke formation.

A coke yield of 50% per conversion step was assumed, based on results obtained from fixed-bed reactor experiments. Under this assumption, the coke-to-plastic ratio remains constant regardless of the alumina-to-plastic ratio, allowing to conclude that the decreasing amount of plastic in the reactor—associated with increasing conversion—does not affect the relative proportion of coke to plastic. An increase in coke content within the reactor leads to a reduction in the minimum fluidization velocity, suggesting that coke formation does not negatively affect the fluidization behavior of the system.

This implies that the evolving composition during reaction, including coke accumulation, remains compatible with stable fluidization. These results therefore confirm the hydrodynamic operability KPI defined in Chapter IV and represent a necessary step toward future implementation of plastic hydrogasification in fluidized-bed reactor configurations.

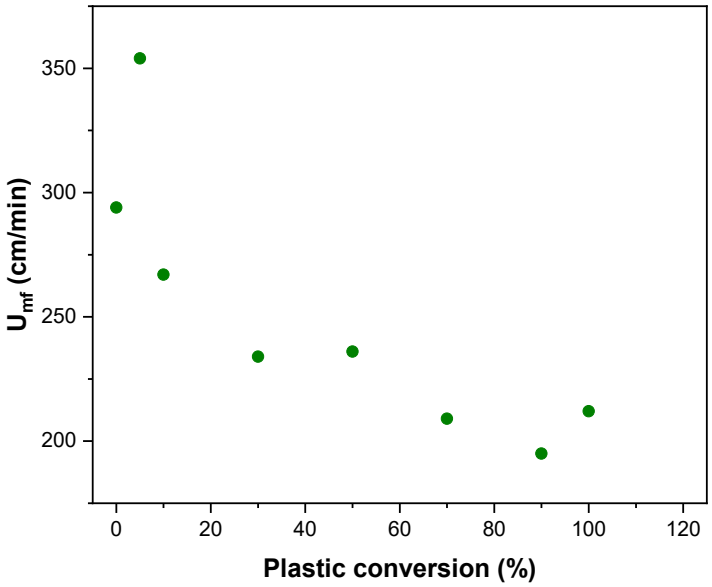


Figure VI.17 *Experimental minimum fluidization velocity of mixtures of alumina, plastic waste and coke*

The fluidization results presented in this study represent a preliminary investigation into the behavior of binary and ternary mixtures of plastic waste and alumina under ambient conditions. While these findings provide valuable insights into the influence of particle size, composition, and mixing ratios on fluidization quality, they do not account for the complex phenomena that may arise under actual reaction conditions.

Further research is needed to assess the fluidization dynamics at elevated temperatures, where thermal softening of plastic, gas-phase reactions, and coke formation may significantly alter bed stability, particle interactions, and minimum fluidization velocity. Understanding these effects is essential for the design and optimization of fluidized-bed reactors intended for plastic waste valorization.

VI.5 Implications of catalytic performance and fluidization behavior for hydrogasification scale-up

The catalytic results obtained at laboratory scale provide essential indications for the design and operation of a hydrogasification reactor at larger scale. The high methane selectivity observed under mild conditions demonstrates that the Ni–Ca/CeO_2/γ-Al_2O_3/OBSiC structured catalyst is

capable of promoting rapid hydrogenolysis and methanation even in the presence of complex polymeric matrices. The onset of methane formation occurs immediately after the plastic reaches its volatilization temperature and volatile intermediates migrate from the pyrolysis zone through the cordierite monolith and reach the catalytic bed. The sharp peak observed in the methane production rate, followed by a rapid decay, mirrors the transient release of volatiles rather than any intrinsic kinetic limitation of the catalyst. The gas-phase composition further supports this interpretation: the concentrations of C_2H_4, C_3H_6, CO and CO_2 remain very low throughout the experiment, indicating that the catalyst converts the intermediates efficiently and without accumulation of partially reformed species. The high methane fraction (up to ~47 vol%) and the reproducible peak shape observed also with the regenerated catalyst confirm that the catalytic bed operates in a regime where intrinsic kinetics are sufficiently fast to process all intermediates delivered from the pyrolysis zone.

These observations imply that, in a scaled-up reactor, the dominant design constraints would be hydrogen distribution, thermal management across the two zones, and the efficiency of volatile transport through the monolith, rather than the intrinsic catalytic activity. Ensuring uniform heating of the pyrolysis region, minimizing temperature gradients at the monolith interface, and maximizing gas–solid contact in the catalytic zone would therefore be essential to preserve the high methane selectivity and the rapid conversion dynamics demonstrated at laboratory scale.

The maximization of heat and mass transport coefficients can be optimized in a fluidized-bed reactor. The fluidization studies carried out in the laboratory provide essential insights into the challenges associated with scaling up a fluidized-bed reactor for catalytic hydrogasification. The pressure-drop measurements show that, for all tested compositions, the system remains far from the minimum fluidization velocity, with ΔP values significantly lower than those expected for a fully expanded bed. This behavior is consistent with the heterogeneous nature of the mixtures: the plastic particles, characterized by low density and irregular shape, exhibit poor fluidization quality, while the alumina particles, although more suitable for fluidization, tend to segregate and settle due to their higher density. These observations imply that, in a scaled-up reactor, achieving homogeneous fluidization of plastic–alumina mixtures would require careful engineering of particle size distribution, density matching, and gas-velocity control. The tendency of the finest alumina fractions to be entrained at relatively low velocities highlights the need for an efficient solids-retention system and for a distributor capable of generating uniform gas flow to minimize channeling and segregation. At the same time, the poor fluidization behavior of the plastic fraction suggests that pelletization, controlled agglomeration, or blending with a larger proportion of inert material may be necessary to stabilize the bed and avoid defluidization events. The ΔP–velocity trends measured at laboratory scale also indicate that

significantly higher superficial gas velocities would be required to reach the minimum fluidization condition in a pilot-scale unit, with the associated risk of excessive entrainment of fines. Overall, the fluidization results delineate the key hydrodynamic constraints for scaling up a fluidized-bed reactor for plastic hydrogasification, namely: the need for optimized particle engineering, mitigation of segregation between plastic and alumina, control of entrainment through appropriate freeboard and cyclone design, and careful selection of the operating gas velocity. These considerations highlight that the transition from a fixed-bed or two-zone reactor to a fluidized-bed configuration is non-trivial when processing heterogeneous plastic waste streams, and that hydrodynamic stability must be addressed as a primary design criterion in future scale-up efforts.

Chapter VII.
Conclusions and future perspectives

This Ph.D. project has been devoted to advancing the understanding of plastic waste decomposition under hydrogasification conditions. The motivation behind this work stems from the need to valorize a material that is currently landfilled, representing both a loss of valuable resources and a significant environmental burden.

The primary objective was the identification of an effective catalyst for the conversion of plastic into methane-enriched gas. Experimental results demonstrated that Ni-catalyzed OBSiC foams are suitable for this purpose, achieving a methane selectivity of approximately 59% and promoting the gasification of the liquid residue formed during pyrolysis. Nevertheless, the product gas stream also contained heavier hydrocarbons (including ethane, ethylene, propane, propylene, and butane), which could be further converted into methane through optimization of reactor design and operating conditions.

Starting from these results, a lab-scale set-up was developed, capable of processing up to 100 g of feed. An integrated reactor configuration was designed to separate the pyrolysis and hydrogenation steps, with a cordierite monolith employed to thermally the zones of reaction. Experimental tests confirmed the feasibility of this approach, with methane production increasing with the amount of plastic waste fed to the reactor and reaching a plateau of around 50 vol.%. Quantitative analysis of the gas stream showed that, at a plastic-to-catalyst ratio of 1.5, the process yielded approximately 450 Nm^3 of gas per ton of plastic waste, with 405 Nm^3 of methane and 16 kg of hydrogen consumed. The methane is the main product, accounting for approximately 84-89% of the total gas, which is much higher with respect to the methane yield in conventional plastic gasification/pyrolysis systems currently

employed. These results confirm the catalytic effectiveness of Ni-based OBSiC foams.

As expected from the nature of the feedstock and despite the promotional effect of calcium on nickel, coke formation was observed, underscoring the need for effective regeneration strategies. The regenerated catalysts exhibited well-preserved activity, as the methane production recorded in the subsequent test showed only a slight decrease compared to the fresh catalyst.

Towards the final stage of the project, attention was directed to the fluidization of mixtures of plastic waste and alumina-based catalysts, as a preliminary step toward testing a fluidized-bed reactor configuration. These studies confirmed that plastic waste can be successfully fluidized when an appropriate ratio of alumina is introduced, acting as the fluidization medium. This represents an important foundation for future investigations, which should focus on fluidization behavior under reaction conditions, including elevated temperatures, coke accumulation, and the evolving morphology of plastic-derived particles. Such studies will be essential to validate the scalability of the process and to optimize reactor design for the valorization of plastic waste in fluidized systems.

Future investigations should focus on the fluidization dynamics at elevated temperatures, where thermal softening of plastic particles, onset of pyrolysis reactions, and progressive coke formation may significantly alter the hydrodynamic regime. In particular, the interplay between heat transfer, gas–solid reactivity and evolving particle morphology must be characterized to assess the stability and scalability of fluidized-bed reactors for plastic waste valorization.

Moreover, the impact of reaction atmosphere (e.g., inert vs. oxidative), gas composition, and superficial velocity on bed expansion, bubbling regime, and segregation phenomena should be systematically studied. The role of coke accumulation on long-term fluidization quality and the effectiveness of regeneration strategies also warrant dedicated analysis.

The results achieved in this project represent a significant contribution to the emerging field of plastic waste valorization via hydrogasification, an area still scarcely explored in the literature. The development of a catalytic system based on Ni-supported OBSiC foams, combined with an integrated reactor configuration capable of separating pyrolysis and hydrogenation steps, demonstrates both technical feasibility and promising conversion performance. The observed methane selectivity and gas yields confirm the potential of this approach for producing energy-rich gas streams from heterogeneous plastic feedstocks. Moreover, the fluidization studies conducted on binary and ternary mixtures of plastic, alumina, and coke provide a valuable foundation for future reactor design, particularly in fluidized-bed configurations. Given the limited number of experimental investigations addressing the coupling of fluidization behavior with reactive

plastic conversion, this work fills a critical gap and opens new perspectives for scalable, thermochemically-driven recycling technologies.

References

Abbasi, T., & Abbasi, S. A. (2010). Biomass energy and the environmental impacts associated with its production and utilization. In *Renewable and Sustainable Energy Reviews* (Vol. 14, Number 3, pp. 919–937). https://doi.org/10.1016/j.rser.2009.11.006

Abdullah, M. Z., Husain, Z., & Yin Pong, S. L. (2003). Analysis of cold flow fluidization test results for various biomass fuels. *Biomass and Bioenergy*, *24*(6), 487–494. https://doi.org/10.1016/S0961-9534(02)00150-2

Al-Maari, M. A., Ahmad, M. A., Din, A. T. M., Hassan, H., & Alsobaai, A. M. (2021). Co-pyrolysis of oil palm empty fruit bunch and oil palm frond with low-density polyethylene and polypropylene for bio-oil production. *Arabian Journal of Chemistry*, *14*(8), 103282. https://doi.org/10.1016/J.ARABJC.2021.103282

Arena, U., & Mastellone, M. L. (2000). Defluidization phenomena during the pyrolysis of two plastic wastes. *Chemical Engineering Science*, *55*(15), 2849–2860. https://doi.org/10.1016/S0009-2509(99)00533-3

Asif, M. (2011). Effect of volume-contraction on incipient fluidization of binary-solid mixtures. *Particuology*, *9*(2), 101–106. https://doi.org/10.1016/J.PARTIC.2010.11.001

Balestieri, F. M. P., Luna, C. M. R., & Ávila, I. (2023). Investigating the Influence of Distributor Type, Particle Size and Rice Husk Percentage on Fluidized Beds through Cold Fluidization Experiments. *Energies*, *16*(22). https://doi.org/10.3390/en16227574

Balzarotti, R., Ambrosetti, M., Beretta, A., Groppi, G., & Tronconi, E. (2022). Recent Advances in the Development of Highly Conductive Structured Supports for the Intensification of Non-adiabatic Gas-Solid Catalytic Processes: The Methane Steam Reforming Case Study. *Frontiers in Chemical Engineering*, *3*. https://doi.org/10.3389/fceng.2021.811439

Barbuzza, E., Buceti, G., Pozio, A., Santarelli, M., & Tosti, S. (2019). Gasification of wood biomass with renewable hydrogen for the production of synthetic natural gas. *Fuel*, *242*, 520–531. https://doi.org/10.1016/j.fuel.2019.01.079

Bartholomew, C. H. (2001). Mechanisms of catalyst deactivation. *Applied Catalysis A: General*, *212*(1–2), 17–60. https://doi.org/10.1016/S0926-860X(00)00843-7

Basu Prabir. (2013). *Biomass Gasification, Pyrolysis, abd Torrefaction. Practical Design and Theory (second edition)*.

Bhandari, R., Trudewind, C. A., & Zapp, P. (2014). Life cycle assessment of hydrogen production via electrolysis – a review. *Journal of Cleaner*

Production, *85*, 151–163. https://doi.org/10.1016/J.JCLEPRO.2013.07.048

Bridier, B., & Pérez-Ramírez, J. (2010). Cooperative effects in ternary Cu-Ni-Fe catalysts lead to enhanced alkene selectivity in alkyne hydrogenation. *Journal of the American Chemical Society*, *132*(12), 4321–4327. https://doi.org/10.1021/ja9101997

Celik, G., Kennedy, R. M., Hackler, R. A., Ferrandon, M., Tennakoon, A., Patnaik, S., Lapointe, A. M., Ammal, S. C., Heyden, A., Perras, F. A., Pruski, M., Scott, S. L., Poeppelmeier, K. R., Sadow, A. D., & Delferro, M. (2019). Upcycling Single-Use Polyethylene into High-Quality Liquid Products. *ACS Central Science*, *5*(11), 1795–1803. https://doi.org/10.1021/acscentsci.9b00722

Chen, R., Zhang, S., Cong, K., Li, Q., & Zhang, Y. (2020). Insight into synergistic effects of biomass-polypropylene co-pyrolysis using representative biomass constituents. *Bioresource Technology*, *307*, 123243. https://doi.org/10.1016/J.BIORTECH.2020.123243

Chen, Z., Dun, Q., Shi, Y., Lai, D., Zhou, Y., Gao, S., & Xu, G. (2017). High quality syngas production from catalytic coal gasification using disposable Ca(OH)2 catalyst. *Chemical Engineering Journal*, *316*, 842–849. https://doi.org/10.1016/J.CEJ.2017.02.025

Cheung L. ; Nienow A.W. ; Rowe P.N. (1973). *minimum-fluidisation-velocity-of-a-binary-mixture-of-different-s-1974*.

Chiba, S., Chiba, T., Nienow, A. W., & Kobayashi, H. (1979). FIuidisation Velocity_ Bed Expansion and Pressure-Drop Profile of Binary Particle Mixtures. In *Powder Technology* (Vol. 22).

Chitester, D. C., Kornosky, R. M., Fan, L. S., & Danko, J. P. (1984). Characteristics of fluidization at high pressure. *Chemical Engineering Science*, *39*(2), 253–261. https://doi.org/10.1016/0009-2509(84)80025-1

Choi, Y., Wang, S., Yoon, Y. M., Jang, J. J., Kim, D., Ryu, H. J., Lee, D., Won, Y., Nam, H., & Hwang, B. (2024). Sustainable strategy for converting plastic waste into energy over pyrolysis: A comparative study of fluidized-bed and fixed-bed reactors. *Energy*, *286*, 129564. https://doi.org/10.1016/J.ENERGY.2023.129564

Conner, W. C., & Falconer, J. L. (1995). Spillover in Heterogeneous Catalysis. In *Chem. Rev* (Vol. 95). https://pubs.acs.org/sharingguidelines

Cronshaw, I. (2015). World Energy Outlook 2014 projections to 2040: Natural gas and coal trade, and the role of China. *Australian Journal of Agricultural and Resource Economics*, *59*(4), 571–585. https://doi.org/10.1111/1467-8489.12120

Cychosz, K. A., Guillet-Nicolas, R., García-Martínez, J., & Thommes, M. (2017). Recent advances in the textural characterization of hierarchically

structured nanoporous materials. In *Chemical Society Reviews* (Vol. 46, Number 2, pp. 389–414). Royal Society of Chemistry. https://doi.org/10.1039/c6cs00391e

Cychosz, K. A., & Thommes, M. (2018). Progress in the Physisorption Characterization of Nanoporous Gas Storage Materials. In *Engineering* (Vol. 4, Number 4, pp. 559–566). Elsevier Ltd. https://doi.org/10.1016/j.eng.2018.06.001

EIJI OBATA, HARU OWATANABE AND NAOTO SHIENDO. (1982). *MEASUREMENT OF SIZE AND SIZE DISTRIBUT10N OF PARTICLES BY FLUIDIZATION*. *15*(1).

Energy Agency, I. (2021). *Net Zero by 2050 - A Roadmap for the Global Energy Sector*. www.iea.org/t&c/

Ewald, S., & Hinrichsen, O. (2019). On the interaction of CO2 with Ni-Al catalysts. *Applied Catalysis A: General*, *580*, 71–80. https://doi.org/10.1016/J.APCATA.2019.04.005

Feng, J., Yan, S., Zhang, R., Gu, S., Qu, X., & Bi, J. (2022). Characteristics of Co–Ca catalyzed coal hydrogasification in a mixture of H2 and CO2 atmosphere. *Fuel*, *324*. https://doi.org/10.1016/j.fuel.2022.124486

Feng, J., Yan, S., Zhang, R., Gu, S., Qu, X., & Bi, J. (2023). Recycling and reuse performance of cobalt catalyst for coal hydrogasification. *Fuel*, *335*. https://doi.org/10.1016/j.fuel.2022.126939

Feng, R., Li, J., Cheng, Z., Yang, X., & Fang, Y. (2017). Influence of particle size distribution on minimum fluidization velocity and bed expansion at elevated pressure. *Powder Technology*, *320*, 27–36. https://doi.org/10.1016/J.POWTEC.2017.07.024

Formisani, B. (1991). Packing and fluidization properties of binary mixtures of spherical particles. *Powder Technology*, *66*(3), 259–264. https://doi.org/10.1016/0032-5910(91)80039-L

Formisani, B., Girimonte, R., & Longo, T. (2008). The fluidization process of binary mixtures of solids: Development of the approach based on the fluidization velocity interval. *Powder Technology*, *185*(2), 97–108. https://doi.org/10.1016/J.POWTEC.2007.10.003

Formisani, B., Girimonte, R., & Vivacqua, V. (2011). Fluidization of mixtures of two solids differing in density or size. *AIChE Journal*, *57*(9), 2325–2333. https://doi.org/10.1002/aic.12450

Formisani, B., Girimonte, R., & Vivacqua, V. (2013). Fluidization of mixtures of two solids: A unified model of the transition to the fluidized state. *AIChE Journal*, *59*(3), 729–735. https://doi.org/10.1002/aic.13876

Freitas, I. C., Manfro, R. L., & Souza, M. M. V. M. (2018). Hydrogenolysis of glycerol to propylene glycol in continuous system without hydrogen addition over Cu-Ni catalysts. *Applied Catalysis B: Environmental*, *220*, 31–41. https://doi.org/10.1016/j.apcatb.2017.08.030

Fu, Z., Zhu, J., Barghi, S., Zhao, Y., Luo, Z., & Duan, C. (2019). Minimum fluidization velocity of binary mixtures of medium particles in the Air Dense medium fluidized bed. *Chemical Engineering Science*, *207*, 194–201. https://doi.org/10.1016/J.CES.2019.06.005

Gandarias, I., Requies, J., Arias, P. L., Armbruster, U., & Martin, A. (2012). Liquid-phase glycerol hydrogenolysis by formic acid over Ni-Cu/Al 2O 3 catalysts. *Journal of Catalysis*, *290*, 79–89. https://doi.org/10.1016/j.jcat.2012.03.004

Gauthier, D., Zerguerras, S., & Flamant, G. (1999). Influence of the particle size distribution of powders on the velocities of minimum and complete fluidization. *Chemical Engineering Journal*, *74*(3), 181–196. https://doi.org/10.1016/S1385-8947(99)00075-3

Geldart, D. (1973). Types of gas fluidization. *Powder Technology*, *7*(5), 285–292. https://doi.org/10.1016/0032-5910(73)80037-3

Geyer, R., Jambeck, J. R., & Law, K. L. (2017). *Production, use, and fate of all plastics ever made*. https://www.science.org

Guo, S., Wang, Z., Chen, G., Zhang, M., Sun, T., Wang, Q., Du, Z., Chen, Y., Wu, M., Li, Z., Lei, T., Burra, K. R. G., & Gupta, A. K. (2023). Co-pyrolysis characteristics of forestry and agricultural residues and waste plastics: Thermal decomposition and products distribution. *Process Safety and Environmental Protection*, *177*, 380–390. https://doi.org/10.1016/j.psep.2023.06.084

Haga' And, T., & Nishiyama, Y. (1983). *Promotion of Nickel-Catalyzed Hydrogasification of Carbon by Alkaline Earth Compounds*.

Haga, T., & Nishiyama, Y. (1987). Promotion of iron-group catalyst by calcium salts in hydrogasification of carbons at elevated pressures. *Ind. Eng. Chem. Res*, *26*(6), 1202–1206.

Haga, T., Ozaki, J.-I., Suzuki, K., & Nishiyama, Y. (1992). Role of MgO and CaO Promoters in Ni-Catalyzed Hydrogenation Reactions of CO and Carbon. In *JOURNAL OF CATALYSIS* (Vol. 134).

Han, Q., Rehman, M. U., Wang, J., Rykov, A., Gutiérrez, O. Y., Zhao, Y., Wang, S., Ma, X., & Lercher, J. A. (2019). The synergistic effect between Ni sites and Ni-Fe alloy sites on hydrodeoxygenation of lignin-derived phenols. *Applied Catalysis B: Environmental*, *253*, 348–358. https://doi.org/10.1016/j.apcatb.2019.04.065

He, S., Sun, C., Yang, X., Wang, B., Dai, X., & Bai, Z. (2010). Characterization of coke deposited on spent catalysts for long-chain-paraffin dehydrogenation. *Chemical Engineering Journal*, *163*(3), 389–394. https://doi.org/10.1016/J.CEJ.2010.07.024

Hong, B., Wang, X., Zhou, Z., & Yu, G. (2013). A Comparison of the Gas-Product-Release Characteristics from Coal Pyrolysis and

Hydrogasification. *Energy Technology*, *1*(8), 449–456. https://doi.org/10.1002/ente.201300052

Hong, D., Li, P., Si, T., & Guo, X. (2021). ReaxFF simulations of the synergistic effect mechanisms during co-pyrolysis of coal and polyethylene/polystyrene. *Energy*, *218*, 119553. https://doi.org/10.1016/j.energy.2020.119553

Hu, B., Yin, Y., Liu, G., Chen, S., Hong, X., & Tsang, S. C. E. (2018). Hydrogen spillover enabled active Cu sites for methanol synthesis from CO2 hydrogenation over Pd doped CuZn catalysts. *Journal of Catalysis*, *359*, 17–26. https://doi.org/10.1016/j.jcat.2017.12.029

Jiang, J., Liu, Q., & Liu, Z. (2016). Superior catalytic effect of calcium oxide on the hydrogasification of char for CH4. *Fuel*, *180*, 737–742. https://doi.org/10.1016/j.fuel.2016.04.093

Jiang, J., Liu, Z., & Liu, Q. (2017). Synergetic catalysis of calcium oxide and iron in hydrogasification of char. *Energy and Fuels*, *31*(1), 198–204. https://doi.org/10.1021/acs.energyfuels.6b02026

Karcz, A., & Porada, S. (1996). The influence of coal rank on formation of gaseous hydrocarbons in hydrogasif ication of coal. *Fuel*, *75*(5). https://doi.org/10.1016/0016-2361(95)00298-7

Khabib, I., Kadarwati, S., & Wahyuni, S. (2014). 92 DEACTIVATION AND REGENERATION OF Ni/ZA CATALYST IN HYDROCRACKING OF POLYPROPYLENE. In *Indo. J. Chem* (Vol. 14, Number 2).

Kissinger, H. E. (1956). Reaction Kinetics in Differential Thermal Analysis. In *Helv. Chim. Acta* (Vol. 28, Number 5). https://pubs.acs.org/sharingguidelines

Kokorotsikos, P. S., Stavropoulos, G. G., & Sakellaropoulos, G. P. (n.d.). *Effect of catalyst impregnation conditions on Greek lignite hydrogasification"*.

Kozanoglu, B. U., Welti Chanes, J., García Cuautle, D., & Santos Jean, J. P. (2002). Hydrodynamics of large particle fluidization in reduced pressure operations: an experimental study. *Powder Technology*, *125*(1), 55–60. https://doi.org/10.1016/S0032-5910(01)00524-1

Lee, K., Jing, Y., Wang, Y., & Yan, N. (2022). A unified view on catalytic conversion of biomass and waste plastics. In *Nature Reviews Chemistry* (Vol. 6, Number 9, pp. 635–652). Nature Research. https://doi.org/10.1038/s41570-022-00411-8

Lee, W. T., Bobbink, F. D., van Muyden, A. P., Lin, K. H., Corminboeuf, C., Zamani, R. R., & Dyson, P. J. (2021). Catalytic hydrocracking of synthetic polymers into grid-compatible gas streams. *Cell Reports Physical Science*, *2*(2), 100332. https://doi.org/10.1016/J.XCRP.2021.100332

Li, C., Xu, G., Zhai, Y., Liu, X., Ma, Y., & Zhang, Y. (2017). Hydrogenation of biomass-derived ethyl levulinate into Γ-valerolactone by activated

carbon supported bimetallic Ni and Fe catalysts. *Fuel*, *203*, 23–31. https://doi.org/10.1016/j.fuel.2017.04.082

Lin, C. L., Wey, M. Y., & You, S. Da. (2002). The effect of particle size distribution on minimum fluidization velocity at high temperature. *Powder Technology*, *126*(3), 297–301. https://doi.org/10.1016/S0032-5910(02)00074-8

Liu, H., Huang, Z., Kang, H., Li, X., Xia, C., Chen, J., & Liu, H. (2018). Efficient bimetallic NiCu-SiO2 catalysts for selective hydrogenolysis of xylitol to ethylene glycol and propylene glycol. *Applied Catalysis B: Environmental*, *220*, 251–263. https://doi.org/10.1016/j.apcatb.2017.08.022

Liu, S., Cheng, X., Zhang, J., Guo, R., & Sun, H. (2024). Further research of the mechanism of char catalytic hydrogasification: Effect of spillover hydrogen on Fe-group catalysts. *Journal of Analytical and Applied Pyrolysis*, *182*, 106718. https://doi.org/10.1016/J.JAAP.2024.106718

Liu, S., Kots, P. A., Vance, B. C., Danielson, A., & Vlachos, D. G. (2021). Plastic waste to fuels by hydrocracking at mild conditions. In *Sci. Adv* (Vol. 7). https://www.science.org

Liu, X., Xiong, B., Huang, X., Ding, H., Zheng, Y., Liu, Z., & Zheng, C. (2017). Effect of catalysts on char structural evolution during hydrogasification under high pressure. *Fuel*, *188*, 474–482. https://doi.org/10.1016/j.fuel.2016.10.053

Lockett, M. J., & Gunnarsson, G. (1973). The delayed bubbling of gas fluidised beds. *Chemical Engineering Science*, *28*(2), 666–668. https://doi.org/10.1016/0009-2509(73)80072-7

Mastellone, M. L., & Arena, U. (2004). Bed defluidisation during the fluidised bed pyrolysis of plastic waste mixtures. *Polymer Degradation and Stability*, *85*(3), 1051–1058. https://doi.org/10.1016/J.POLYMDEGRADSTAB.2003.04.002

Matsumoto, S. (1991). Catalyzed Hydrogasification of Yallourn Char in the Presence of Supported Hydrogenation Nickel Catalyst. *Energy and Fuels*, *5*(1), 60–63. https://doi.org/10.1021/ef00025a009

Melaina, M. W., Antonia, O., & Penev, M. (2013). *Blending Hydrogen into Natural Gas Pipeline Networks: A Review of Key Issues*. http://www.osti.gov/bridge

Miandad, R., Barakat, M. A., Aburiazaiza, A. S., Rehan, M., Ismail, I. M. I., & Nizami, A. S. (2017). Effect of plastic waste types on pyrolysis liquid oil. *International Biodeterioration & Biodegradation*, *119*, 239–252. https://doi.org/10.1016/J.IBIOD.2016.09.017

Mo, F., Ullah, H., Zada, N., & Shahab, A. (2023). A Review on Catalytic Co-Pyrolysis of Biomass and Plastics Waste as a Thermochemical Conversion to Produce Valuable Products. In *Energies* (Vol. 16, Number

14). Multidisciplinary Digital Publishing Institute (MDPI). https://doi.org/10.3390/en16145403

Morales, S., Miranda, R., Bustos, D., Cazares, T., & Tran, H. (2014). Solar biomass pyrolysis for the production of bio-fuels and chemical commodities. *Journal of Analytical and Applied Pyrolysis*, *109*, 65–78. https://doi.org/10.1016/j.jaap.2014.07.012

Murakami, K., Arai, M., & Shirai, M. (2000). Hydrogasification of Loy Yang Brown Coal by Ion-Exchanged Nickel Species. *Energy and Fuels*, *14*(6), 1240–1244. https://doi.org/10.1021/ef000099v

Nam, H., & Capareda, S. (2015). Experimental investigation of torrefaction of two agricultural wastes of different composition using RSM (response surface methodology). *Energy*, *91*, 507–516. https://doi.org/10.1016/J.ENERGY.2015.08.064

Nam, H., Capareda, S. C., Ashwath, N., & Kongkasawan, J. (2015). Experimental investigation of pyrolysis of rice straw using bench-scale auger, batch and fluidized bed reactors. *Energy*, *93*, 2384–2394. https://doi.org/10.1016/J.ENERGY.2015.10.028

Ochoa, A., Bilbao, J., Gayubo, A. G., & Castaño, P. (2020). Coke formation and deactivation during catalytic reforming of biomass and waste pyrolysis products: A review. *Renewable and Sustainable Energy Reviews*, *119*, 109600. https://doi.org/10.1016/J.RSER.2019.109600

Ohgoshi, S., Nakamura, I., & wakushima, Y. (1993). Hydrogenation of isobutylene by spiltover hydrogen from Pt/KA-zeolite to NaY-zeolite. *Studies in Surface Science and Catalysis*, *77*(C), 289–292. https://doi.org/10.1016/S0167-2991(08)63193-6

Olivieri, G., Marzocchella, A., & Salatino, P. (2004). Segregation of fluidized binary mixtures of granular solids. *AIChE Journal*, *50*(12), 3095–3106. https://doi.org/10.1002/aic.10340

Pan, Q., Peng, J., Sun, T., Wang, S., & Wang, S. (2014). Insight into the reaction route of CO2 methanation: Promotion effect of medium basic sites. *Catalysis Communications*, *45*, 74–78. https://doi.org/10.1016/J.CATCOM.2013.10.034

Pan, Z., Wang, R., & Chen, J. (2018). Deoxygenation of methyl laurate as a model compound on Ni-Zn alloy and intermetallic compound catalysts: Geometric and electronic effects of oxophilic Zn. *Applied Catalysis B: Environmental*, *224*, 88–100. https://doi.org/10.1016/j.apcatb.2017.10.040

Paudel, B., & Feng, Z. G. (2013). Prediction of minimum fluidization velocity for binary mixtures of biomass and inert particles. *Powder Technology*, *237*, 134–140. https://doi.org/10.1016/J.POWTEC.2013.01.031

Pérez, N. P., Pedroso, D. T., Machin, E. B., Antunes, J. S., Verdú Ramos, R. A., & Silveira, J. L. (2018). Prediction of the minimum fluidization velocity

of particles of sugarcane bagasse. *Biomass and Bioenergy*, *109*, 249–256. https://doi.org/10.1016/J.BIOMBIOE.2017.12.004

Petala, A., & Panagiotopoulou, P. (2018). Methanation of CO2 over alkali-promoted Ru/TiO2 catalysts: I. Effect of alkali additives on catalytic activity and selectivity. *Applied Catalysis B: Environmental*, *224*, 919–927. https://doi.org/10.1016/J.APCATB.2017.11.048

Plastics-the Facts 2019 An analysis of European plastics production, demand and waste data. (n.d.).

Qu, X., Wang, Q. F., Yan, S., Feng, J., Zhang, J. S., Zhang, R., & Bi, J. C. (2022). The behavior of the different catalysts for model carbon hydrogasification. *Ranliao Huaxue Xuebao/Journal of Fuel Chemistry and Technology*, *50*(1), 1–10. https://doi.org/10.1016/S1872-5813(21)60136-6

Qu, X., Yan, S., Yan, X., Zhang, J., Zheng, Q., & An, Y. (2019). Role of cobalt and calcium on coal catalytic hydrogasification in a pressurized fluidized bed. *Fuel*, *239*, 347–356. https://doi.org/10.1016/j.fuel.2018.11.031

Qureshi, M. S., Oasmaa, A., Pihkola, H., Deviatkin, I., Tenhunen, A., Mannila, J., Minkkinen, H., Pohjakallio, M., & Laine-Ylijoki, J. (2020a). Pyrolysis of plastic waste: Opportunities and challenges. *Journal of Analytical and Applied Pyrolysis*, *152*, 104804. https://doi.org/10.1016/J.JAAP.2020.104804

Qureshi, M. S., Oasmaa, A., Pihkola, H., Deviatkin, I., Tenhunen, A., Mannila, J., Minkkinen, H., Pohjakallio, M., & Laine-Ylijoki, J. (2020b). Pyrolysis of plastic waste: Opportunities and challenges. *Journal of Analytical and Applied Pyrolysis*, *152*, 104804. https://doi.org/10.1016/J.JAAP.2020.104804

R. Rao, T., & Ram. Bheemarasetti, J. V. (2001). Minimum fluidization velocities of mixtures of biomass and sands. *Energy*, *26*(6), 633–644. https://doi.org/10.1016/S0360-5442(01)00014-7

Reina, J., Velo, E., & Puigjaner, L. (2000). Predicting the minimum fluidization velocity of polydisperse mixtures of scrap-wood particles. *Powder Technology*, *111*(3), 245–251. https://doi.org/10.1016/S0032-5910(00)00226-6

Renda, S., Soler, J., Herguido, J., & Menéndez, M. (2025). Effect of particles size and density on the segregation of catalyst-sorbent mixtures for direct sorption-enhanced DME synthesis: Experimental and mathematical study. *Biomass and Bioenergy*, *197*, 107764. https://doi.org/10.1016/J.BIOMBIOE.2025.107764

Rincon, J., Guardioòa, J., Romero, A., & Ramos, G. (1994). Predicting the minimum fluidization velocity of multicomponent systems. *Journal of Chemical Engineering of Japan*, *27*(2).

Rorrer, J. E., Beckham, G. T., & Román-Leshkov, Y. (2021). Conversion of Polyolefin Waste to Liquid Alkanes with Ru-Based Catalysts under Mild Conditions. *JACS Au*, *1*(1), 8–12. https://doi.org/10.1021/jacsau.0c00041

Rowe, P. N., Partridge, B. A., & Lyall, E. (1964). Cloud formation around bubbles in gas fluidized beds. *Chemical Engineering Science*, *19*(12), 973–985. https://doi.org/10.1016/0009-2509(64)85104-6

Sancier, K. M. (1971). Hydrogen migration on Alumina/Palladium catalysts for benzene hydrogenation. *Journal of Catalysis*, *20*(1), 106–109. https://doi.org/10.1016/0021-9517(71)90011-X

Scheirs, John., & Kaminsky, W. . (2006). *Feedstock recycling and pyrolysis of waste plastics : converting waste plastics into diesel and other fuels*. J. Wiley & Sons.

Shah, H. H., Amin, M., Iqbal, A., Nadeem, I., Kalin, M., Soomar, A. M., & Galal, A. M. (2023). A review on gasification and pyrolysis of waste plastics. In *Frontiers in Chemistry* (Vol. 10). Frontiers Media S.A. https://doi.org/10.3389/fchem.2022.960894

Sheth, A. C., Sastry, C., Yeboah, Y. D., Xu, Y., & Agarwal, P. (2004). Catalytic gasification of coal using eutectic salts: Reaction kinetics for hydrogasification using binary and ternary eutectic catalysts. *Fuel*, *83*(4–5). https://doi.org/10.1016/j.fuel.2003.08.016

Si, C., & Guo, Q. (2008). Fluidization characteristics of binary mixtures of biomass and quartz sand in an acoustic fluidized bed. *Industrial and Engineering Chemistry Research*, *47*(23), 9773–9782. https://doi.org/10.1021/ie801070z

Skodras, G., Panagiotidou, S., Kokorotsikos, P., & Serafidou, M. (2016). Potassium catalyzed hydrogasification of low-rank coal for synthetic natural gas production. *Open Chemistry*, *14*(1), 92–102. https://doi.org/10.1515/chem-2016-0009

Sun, H., Wang, J., Bi, J., Zhang, R., Qu, X., Zhang, J., & Zhang, J. (2021). Investigating the Cu-based catalysts for char catalytic hydrogasification and its recovery. *Fuel*, *294*. https://doi.org/10.1016/j.fuel.2021.120567

Sun, H., Zhang, F., Bi, J., Qu, X., Yan, S., Zhang, J., & Zhang, J. (2019). Study of Cu-Ni-Ca Composite Catalysts in Catalytic Hydrogasification of Char. *Energy and Fuels*, *33*(10), 9661–9670. https://doi.org/10.1021/acs.energyfuels.9b02279

Terry, L. M., Wee, M. X. J., Chew, J. J., Khaerudini, D. S., Timuda, G. E., Aqsha, A., Saptoro, A., & Sunarso, J. (2023). Co-pyrolysis of oil palm trunk and polypropylene: Pyrolysis oil composition and formation mechanism. *South African Journal of Chemical Engineering*, *43*, 348–358. https://doi.org/10.1016/J.SAJCE.2022.12.001

Tezer, Ö., Karabağ, N., Öngen, A., Çolpan, C. Ö., & Ayol, A. (2022). Biomass gasification for sustainable energy production: A review. *International Journal of Hydrogen Energy*, *47*(34), 15419–15433. https://doi.org/10.1016/J.IJHYDENE.2022.02.158

Tian, L., Shen, B., Xu, H., Li, F., Wang, Y., & Singh, S. (2016). Thermal behavior of waste tea pyrolysis by TG-FTIR analysis. *Energy*, *103*, 533–542. https://doi.org/10.1016/J.ENERGY.2016.03.022

Tosti, S., Spazzafumo, G., Capobianco, D., Buceti, G., Pozio, A., & Bartucca, S. (2016). EU scenarios of renewable coal hydro-gasification for SNG production. *Sustainable Energy Technologies and Assessments*, *16*, 43–52. https://doi.org/10.1016/j.seta.2016.04.003

Tukker, A., & Picard, L. (1999). *STB-99-55 Final*.

Valentini, M., Groppi, G., Cristiani, C., Levi, M., Tronconi, E., & Forzatti, P. (2001). The deposition of-Al 2 O 3 layers on ceramic and metallic supports for the preparation of structured catalysts. In *Catalysis Today* (Vol. 69).

Wang, S., Kim, H., Lee, D., Lee, Y. R., Won, Y., Hwang, B. W., Nam, H., Ryu, H. J., & Lee, K. H. (2021). Drop-in fuel production with plastic waste pyrolysis oil over catalytic separation. *Fuel*, *305*, 121440. https://doi.org/10.1016/J.FUEL.2021.121440

Wang, Y., Li, Y., Zhang, C., Yang, L., Fan, X., & Chu, L. (2021). A study on co-pyrolysis mechanisms of biomass and polyethylene via ReaxFF molecular dynamic simulation and density functional theory. *Process Safety and Environmental Protection*, *150*, 22–35. https://doi.org/10.1016/j.psep.2021.04.002

Weldekidan, H., Strezov, V., & Town, G. (2018). Review of solar energy for biofuel extraction. In *Renewable and Sustainable Energy Reviews* (Vol. 88, pp. 184–192). Elsevier Ltd. https://doi.org/10.1016/j.rser.2018.02.027

Wen, C. Y., & Yu, Y. H. (1953). A Generalized Method for Predicting the Minimum Fluidization Velocity. In *Wohl, K., Trans. Am. Inst. Chem. Eng* (Vol. 47).

Woo Park, J., Cheon Oh, S., Pyeong Lee, H., Taik Kim, H., & Ok Yoo, K. (2000). A kinetic analysis of thermal degradation of polymers using a dynamic method. *Polymer Degradation and Stability*, *67*(3), 535–540. https://doi.org/10.1016/S0141-3910(99)00155-X

Wu, C.-H., Chang, C.-Y., Hor, J.-L., Shih, S.-M., & Chen, L.-W. (1993). ON THE THERMAL TREATMENT OF PLASTIC MIXTURES OF MSW: PYROLYSIS KINETICS. In *WASTE MANAGEMENT* (Vol. 13).

Xiong, M., Gao, Z., & Qin, Y. (2021). Spillover in Heterogeneous Catalysis: New Insights and Opportunities. In *ACS Catalysis* (Vol. 11, Number 5, pp.

3159–3172). American Chemical Society. https://doi.org/10.1021/acscatal.0c05567

Xu, F., Wang, B., Yang, D., Hao, J., Qiao, Y., & Tian, Y. (2018). Thermal degradation of typical plastics under high heating rate conditions by TG-FTIR: Pyrolysis behaviors and kinetic analysis. *Energy Conversion and Management*, *171*, 1106–1115. https://doi.org/10.1016/J.ENCONMAN.2018.06.047

Xuan, W., Yan, S., & Dong, Y. (2023). Exploration of Pyrolysis Behaviors of Waste Plastics (Polypropylene Plastic/Polyethylene Plastic/Polystyrene Plastic): Macro-Thermal Kinetics and Micro-Pyrolysis Mechanism. *Processes*, *11*(9), 2764. https://doi.org/10.3390/pr11092764

Yan, L., He, B., Ma, L., Pei, X., & Wang, C. (2014). Chemical equilibrium model and prediction for coal hydrogasification. *International Journal of Chemical Reactor Engineering*, *12*(1). https://doi.org/10.1515/ijcre-2012-0031

Yan, S., Bi, J., & Qu, X. (2017). The behavior of catalysts in hydrogasification of sub-bituminous coal in pressured fluidized bed. *Applied Energy*, *206*, 401–412. https://doi.org/10.1016/j.apenergy.2017.08.189

Yan, S., Feng, J., Yuan, S., Xia, Z., Han, F., Qu, X., & Bi, J. (2024). A critical review on direct catalytic hydrogasification of coal into CH4: catalysis process configurations, evaluations, and prospects. *International Journal of Coal Science and Technology*, *11*(1). https://doi.org/10.1007/s40789-024-00677-x

Yan, S., Qu, X., Xia, Z., Chen, C., & Bi, J. (2021). Catalytic hydrogasification characteristic of coal with diverse properties in a pressurized fluidized bed. *Fuel*, *296*. https://doi.org/10.1016/j.fuel.2021.120652

Yan, S., Qu, X., Xia, Z., Chen, C., & Bi, J. (2022). Effect of experimental variables on coal catalytic hydrogasification in a pressurized fluidized bed. *Fuel*, *307*. https://doi.org/10.1016/j.fuel.2021.121761

Yan, S., Zhang, J., Yan, X., Pan, D., Ren, H., & Qu, X. (2018). Catalytic coal hydrogasification by cobalt-calcium catalyst in a pressurized fluidized bed: Role of hydropyrolysis and catalysis process. *Journal of Analytical and Applied Pyrolysis*, *135*, 251–259. https://doi.org/10.1016/j.jaap.2018.08.028

Yang, J., Miranda, R., & Roy, C. (2001). Using the DTG curve fitting method to determine the apparent kinetic parameters of thermal decomposition of polymers. *Polymer Degradation and Stability*, *73*(3), 455–461. https://doi.org/10.1016/S0141-3910(01)00129-X

Yek, P. N. Y., Chan, Y. H., Foong, S. Y., Mahari, W. A. W., Chen, X., Liew, R. K., Ma, N. L., Tsang, Y. F., Sonne, C., Cheng, Y. W., Tan, Y. H., & Lam, S. S. (2024). Co-processing plastics waste and biomass by pyrolysis–gasification: a review. In *Environmental Chemistry Letters* (Vol. 22,

Number 1, pp. 171–188). Springer Science and Business Media Deutschland GmbH. https://doi.org/10.1007/s10311-023-01654-7

Yongbin, J., Jiejie, H., & Yang, W. (2004). Effects of calcium oxide on the cracking of coal tar in the freeboard of a fluidized bed. *Energy and Fuels*, *18*(6), 1625–1632. https://doi.org/10.1021/ef034077v

Yuan, S., Qu, X., Zhang, R., & Bi, J. (2015). Effect of calcium additive on product yields in hydrogasification of nickel-loaded Chinese sub-bituminous coal. *Fuel*, *147*. https://doi.org/10.1016/j.fuel.2015.01.004

Yuan, S., Zhang, N., Qu, X., Bi, J., Cao, Q., & Wang, J. (2017). Promoted catalysis of calcium on the hydrogasification reactivity of iron-loaded subbituminous coal. *Fuel*, *200*, 153–161. https://doi.org/10.1016/j.fuel.2017.03.066

Zhang, F., Sun, H., Bi, J., Qu, X., Yan, S., Zhang, J., & Zhang, J. (2019). The evolution of Fe and Fe-Ca catalysts during char catalytic hydrogasification. *Fuel*, *257*. https://doi.org/10.1016/j.fuel.2019.116040

Zhang, F., Zeng, M., Yappert, R. D., Sun, J., Lee, Y.-H., Lapointe, A. M., Peters, B., Abu-Omar, M. M., & Scott, S. L. (n.d.). *POLYMER CHEMISTRY Polyethylene upcycling to long-chain alkylaromatics by tandem hydrogenolysis/aromatization*. Retrieved https://www.science.org

Zhang, J., Zhang, L., Yang, Z., Yan, Y., Mao, Y., & Bi, J. (2015). Effect of bauxite additives on ash sintering characteristics during the K2CO3-catalyzed steam gasification of lignite. *RSC Advances*, *5*(9), 6720–6727. https://doi.org/10.1039/c4ra14060e

Zhang, Y., Ji, G., Chen, C., Wang, Y., Wang, W., & Li, A. (2020). Liquid oils produced from pyrolysis of plastic wastes with heat carrier in rotary kiln. *Fuel Processing Technology*, *206*, 106455. https://doi.org/10.1016/J.FUPROC.2020.106455

Zhang, Z., Wang, J., Ge, X., Wang, S., Li, A., Li, R., Shen, J., Liang, X., Gan, T., Han, X., Zheng, X., Duan, X., Wang, D., Jiang, J., & Li, Y. (2023). Mixed Plastics Wastes Upcycling with High-Stability Single-Atom Ru Catalyst. *Journal of the American Chemical Society*, *145*(41), 22836–22844. https://doi.org/10.1021/jacs.3c09338

Zhao, M., Chu, X., Wang, F., Fang, Y., Sun, L., Xie, Q., Zhang, L. L., Song, S., Zhang, H., & Wang, X. (2024). Enhancing the Conversion Efficiency of Polyethylene to Methane through Codoping of Mn Atoms into Ru Centers and CeO2 Supports. *Journal of the American Chemical Society*, *146*(48), 33104–33111. https://doi.org/10.1021/jacs.4c10793

Zhong, W., Jin, B., Zhang, Y., Wang, X., & Xiao, R. (2008). Fluidization of biomass particles in a gas-solid fluidized bed. *Energy and Fuels*, *22*(6), 4170–4176. https://doi.org/10.1021/ef800495u

Zoheidi, H., & Miller, D. J. (n.d.). *ROLE OF OXYGEN SURFACE GROUPS IN CATALYSIS OF HYDROGASIFICATION OF CARBON BLACK BY POTASSIUM CARBONATE* (Vol. 2, Number 6).